UNIVERSITY OF OKLAHOMA

GRADUATE COLLEGE

# INTERACTION EFFECTS IN GENERALIZED DIRAC SYSTEMS

A DISSERTATION

SUBMITTED TO THE GRADUATE FACULTY

in partial fulfillment of the requirements for the

Degree of

DOCTOR OF PHILOSOPHY

By

XU DOU
Norman, Oklahoma
2018

INTERACTION EFFECTS IN
GENERALIZED DIRAC SYSTEMS

A DISSERTATION APPROVED FOR THE
HOMER L. DODGE DEPARTMENT OF PHYSICS AND ASTRONOMY

BY

Dr. Bruno Barboza, Chair

Dr. Bin Wang

Dr. Kieran Mullen

Dr. Michael Santos

Dr. Arne Schwettmann

To

my family

# Acknowledgements

I would like to first thank my advisor Bruno Uchoa for his guidance and help.

I want to thank postdocs in the group: Akbar Jaefari and Kangjun Seo. They are also mentors in different aspects of my research projects. I want to thank them for teaching me and answering my questions.

Thank you to my committee members and former committee members of this thesis: Bin Wang, Kieran Mullen, Michael Santos, Arne Schwettmann, Barbara Capogrosso-Sansone, Nikola Petrov. I benefit from their instructions.

I would like to thank many people who taught me physics during my graduate school years. Among them, I want to especially thank Ron Kantowski and Kim Milton.

I would like to thank my peer graduate students and other Nielsen Hall dwellers for many interesting conversations and sharing our time here.

My life became easier with the help of our departmental staff. Thank you!

Finally, I would like to thank my mother Ying and my father Guangzhi for their constant support and encouragement.

# Table of Contents

# List of Figures

# List of Tables

# Abstract

Interaction effects in condensed matter systems with chiral quasiparticles at low energy are studied. A prominent example in the category of such systems is monolayer graphene, which has low energy massless Dirac excitations near some special points in the momentum space. We consider three generalized Dirac systems, which include ABC-stacked trilayer graphene, a superlattice of a gapped Dirac system decorated with charged impurities, and chromium dioxide (CrO2) bilayers. Interaction effects and interaction-induced phases are examined in these systems. For the ABC-stacked trilayer graphene, we calculate the renormalization properties of the chiral massless quasiparticles due to electron-electron interactions. Renormalization features of several physical observables are also studied, which may be measured in experiments. For the superlattice system of a two-dimensional gapped Dirac system with charged impurities, we show that this superlattice system can simulate SU(4) symmetric spin-orbital lattice models. We study the correlations of mid-gap bound states formed around the Coulomb impurities and propose the emergence of quantum spin-orbital liquids in this setup. In the third part, the focus is on the system of chromium dioxide bilayers, which also host Dirac quasiparticles at low energy. We investigate the possibility of forming chiral p+ip superconductivity in chromium dioxide bilayers.

# Chapter 1

# Introduction

## 1.1 Overview

One important research topic in condensed matter physics is the study of systems in which exotic quasiparticle excitations appear. A particular class of materials, the theme of this thesis, named nodal materials, is of recent research interest. In these systems, the conduction and the top of the valence energy bands cross at isolated points, which are called nodal points or band touching points (Fig. 1.1). These crossing points are rare. In general, when energy bands cross they hybridize and a gap opens in the energy spectrum. If the Fermi level is tuned to cross these points, then the low energy excitations of the system would appear just around these points. In the definitions of electronic band theory, a material with a very small overlap between the conduction band and the valence band is defined as a semimetal. Nodal materials belong to semimetals.

Many examples of these systems have emerged in different spatial dimensions. Single layer graphene, a single atom thick film consists of carbon atoms formed in a honeycomb lattice, is a prominent example in two dimensions. At low energy,

the dispersion relation of graphene has a relativistic form and the low energy degrees of freedom can be described by the two dimensional Dirac equation. Few layer graphene [1] systems and graphene-based systems (for example) are also typical representatives of 2D nodal materials. In few layer graphene systems, the energy spectrum depends on how graphene layers are stacked. Besides the isolated touching points property, these materials show chiral quasiparticles with non-trivial Berry phase [2], after moving around the touching point the wavefunction acquires a phase factor. Very recently, semi-Dirac metals have been proposed, where the quasiparticles have a vanishing density of states at the nodal point, with linear dispersion in one direction and quadratic in the other [3].

The focus of this thesis is on two dimensional systems. In three dimensional systems, the conditions for the appearance of nodal points are different. Subjected to some global constraints, these touching points are stable. Three dimensional topological semimetals including Weyl and Dirac semimetals have attracted much attention; for a convenient review see [4]. Two dimensional materials like graphene have special lattice symmetries which ensure the appearance of the nodal points. In three dimensional Weyl semimetals, isolated band touching points have a topological origin. These materials are characterized by exotic surface Fermi-arc states, which are zero energy localized states forming an arc on the surface of the mateirals. These surface states emerge as a result of the topological properties of the bulk. As in the quantum Hall effect, those surface states are robust and are predicted to have unusual transport phenomena. Other interesting systems are Dirac loop semi-metals which include both topological and non-topological types, where the overlap between the conduction band and the top of the valence band is a loop and Dirac-like quasiparticles form along this loop rather than at isolated points [5] in the momentum space.

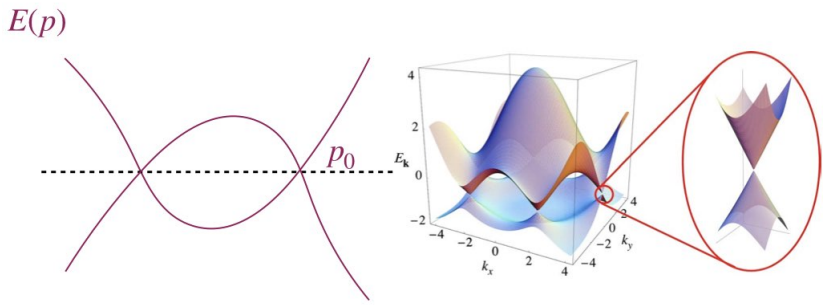


Figure 1.1: Left: Nodal points in one dimension; $E(p)$ is the energy. Two bands cross at two points, and the right one is $p_0$. The dashed line represents the Fermi level. Right: The energy bands of graphene shows a set of band touching points.

In this thesis we study some generalizations of two dimensional Dirac materials. Combined with atoms added to the materials and substrates, two dimensional materials can be a platform for new exotic physics. For example, coupling a graphene film to a substrate can break the original lattice symmetry of graphene. Therefore, combinations of those systems with specially designed substrates allow a vast number of possibilities for novel quantum phenomena. Few layer graphene systems have larger densities of states in the low energy end of the spectrum, and the stacking-dependent dispersion relation can provide more opportunities for many-body effects [6].

## 1.2 Motivations and works

In the works presented in this thesis, we are mainly concerned with the interaction effects in two dimensional Dirac systems. Particularly, we examine three systems where interactions interplay with nodal quasiparticle excitations and we concentrate on finding effects detectable in experiments. These include:

- *ABC-stacked trilayer graphene system*: This system has the cubic dispersion, therefore the density of states are larger compared to the single layer

graphene systems, which may provide a good platform for many-body instabilities. Electron-electron interactions are important from the points of view of the renormalization flow. In experiments, an energy gap has been observed, and this gap is believed to be induced by interactions. Partially motivated by this observation, we investigate many body effects due to the long range electron-electron interactions among charged quasiparticles in this work. Particularly, we try to find measurable effects and focus on the renormalization of quasiparticle properties which we may be observed in experiments.

- *Hetereostructure of single layer graphene decorated with Coulomb impurity lattice*: Quantum spin liquids are elusive states in real materials. Will they be realized in more controllable experimental setups, for example, in artificial superlattices? Most of the proposals in controllable systems are based on cold atom experiments. In this part, the aim is to simulate Mott physics in a solid state system. Bound states around charged impurities can be used to simulate a correlated superlattice, where the states carrying spin and valley quantum numbers interact with each other. We calculate several parameters characterizing the superlattice system, and propose the superlattice to be a solid-state platform for realizing spin-orbital liquids.

- *Chiral topological superconductivity in chromium dioxide*: Chromium dioxide bilayers are predicted to have four Dirac nodes in the Brillouin zone [156]. Chromium dioxide is a well-known half-metal, which is spin-polarized near the Fermi energy. Therefore, the superconductivity can only happen in the spin triplet channel. Motivated by the unsual spin polarization property, we study the possibility of a spin triplet superconductivity instability.

The chiral topological superconductivity property of this system is studied.

This thesis is based on the publications of [7], [8], and [9].

# Chapter 2

# Dirac systems in condensed matter physics

In this chapter, we provide some general introductions to some concepts important to the thesis. For a better understanding and providing useful preparations for further generalizations, we also review some concepts which can be compared to the systems with which we are concerned here.

## 2.1 Single-layer graphene

We briefly review the low energy properties of single layer graphene. Graphene is a 2D carbon material with two atoms per unit cell. A note on units: in this chapter we set $\hbar = 1$. In this section, we follow the notation and coordinate choice used in the review paper [1]. The lattice vectors are (see Fig. 2.1)

$$\vec{a}_1 = \frac{a}{2}(3, \sqrt{3}),\ \vec{a}_2 = \frac{a}{2}(3, -\sqrt{3}), \tag{2.1}$$

in which $a$ is the lattice constant. The reciprocal lattice vectors are obtained

$$\vec{b}_1 = \frac{2\pi}{3a}(1, \sqrt{3}),\ \vec{b}_2 = \frac{2\pi}{3a}(1, -\sqrt{3}). \tag{2.2}$$

The tight-binding Hamiltonian model for graphene can be written as

$$\begin{aligned} H = & -t \sum_{<i,j>} (a^{\dagger}_{\sigma,i} b_{\sigma,j} + h.c.) \\ & - t' \sum_{\ll i,j \gg} (a^{\dagger}_{\sigma,j} a_{\sigma,j} + b^{\dagger}_{\sigma,i} b_{\sigma,i} + h.c.), \end{aligned} \tag{2.3}$$

where spin summation is assumed, $t$ and $t'$ are hopping parameters for the nearest neighbor and the next nearest neighbor sites. In this model, electrons can hop (annihilation and creation operators) between nearest-neighbor and next-nearest-neighbor. Diagonalizing the Hamiltonian, we obtain the energy spectrum

$$E_{\pm} = \pm\sqrt{3 + f(\vec{k})} - t' f(\vec{k}), \tag{2.4}$$

where $f(\vec{k}) = 2\cos(\sqrt{3}k_y a) + 4\cos(\frac{\sqrt{3}}{2}k_y a)\cos(\frac{3}{2}k_x a)$. In this two-band case, the conduction band and the valence band touch at discrete points in the Brillouin zone. By tuning the Fermi energy properly, we could get a point-like Fermi "surface". There are some special points in the Brillouin zone, where the low energy excitation behaves as a massless Dirac fermion. These points are called $K$ points,

$$\vec{K} = (\frac{2\pi}{3a}, \frac{2\pi}{3\sqrt{3}a}),\ \vec{K}' = (\frac{2\pi}{3a}, -\frac{2\pi}{3\sqrt{3}a}).$$

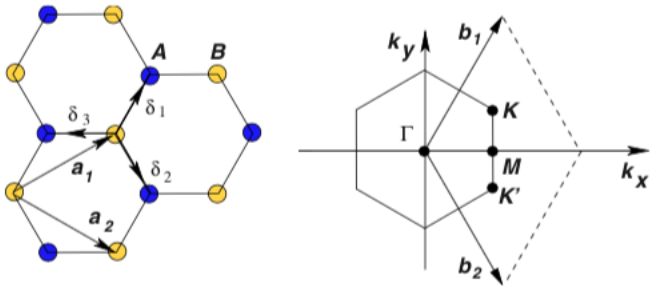


Figure 2.1: The honeycomb lattice and the Brillouin one. The figure is from [1].

If the system is tuned slightly away from the zero energy point, and in the low momentum limit $|\vec{k}| = \vec{K} + \vec{q}$ with $\vec{q} \approx 0$,

$$E_{\pm}(\vec{q}) \approx \pm v_F |\vec{q}| + \mathcal{O}((q/K)^2), \tag{2.5}$$

where $v_F$ is the Fermi velocity defined as $v_F = 3ta/2$, its magnitude is $v_F \approx 1 \times 10^6 \mathrm{m/s}$.

We have seen the linear spectrum at low energy, and it can be shown that the low energy Hamiltonians which describe the physics near nodal points are Dirac Hamiltonians [1]. In this effective formalism, only low energy degrees of freedom $\psi$ near nodal points are kept. The expansion of the original mode defined in the lattice in terms of the effective modes are

$$a(\vec{r}) \sim \mathrm{e}^{ik_F \cdot \vec{r}} \psi_A^K(\vec{r}) + \mathrm{e}^{-ik_F \cdot \vec{r}} \psi_A^{K'}(\vec{r}), \tag{2.6}$$

and $b$ operator has a similar expansion. We define the new operator which combines operators from two valleys

$$\psi = (\psi_A^K(\vec{k}), \psi_B^K(\vec{k}), \psi_B^{K'}(\vec{k}), -\psi_A^{K'}(\vec{k}))^T. \tag{2.7}$$

In terms of these operators $\psi_\sigma$

$$H = \int \mathrm{d}^2 r \psi^\dagger(\vec{r})[-iv_F \vec{\sigma} \cdot \vec{\nabla}]\psi(\vec{r}). \tag{2.8}$$

We can also obtain the equations of motion in each valley. Consider a two component wave function at the $K$(or $K'$) point,

$$-iv_F \vec{\sigma} \cdot \vec{\nabla}\phi(\vec{r}) = E\phi(\vec{r}). \tag{2.9}$$

The solutions corresponding to the two eigenvalues are

$$\phi_{\pm,K}(\vec{k}) = \frac{1}{\sqrt{2}} \begin{pmatrix} \mathrm{e}^{-i\theta_k/2} \\ \pm \mathrm{e}^{i\theta_k/2} \end{pmatrix} \tag{2.10}$$

where $\theta_k$ is the angle of $\vec{k}$ with respect to the point $K$, and $\theta_k \equiv \arctan\frac{k_y - K_y}{k_x - K_x}$. Due to the phase factor, we can see that a $2\pi$ change makes the wave function change sign. And this wave function is also the eigenvector of the helicity operator

$$h = \frac{1}{2}\vec{\sigma} \cdot \frac{\vec{p}}{|\vec{p}|}, \tag{2.11}$$

and $h\phi_K = \pm\phi_K$. The eigenvalues characterize the helicity of these low energy modes.

## 2.2 Berry phase and Chern number

The $\pi$ change in the phase factor of the wave function when a $2\pi$ change is made to $\theta_k$ is called the Berry phase. When discussing topological properties of Dirac and Weyl systems, the concept of Berry phase is crucial. So in this subsection we

give a brief review of several facts about the Berry phase. For a thorough review on this topic, please read [11].

We start with a process that changes a quantum system adiabatically in the parameter space. The quantum adiabatic theorem states that an initial eigenstate of the system will evolve into the eigenstate of the time-dependent Hamiltonian with the same corresponding quantum number. However, the new state would acquire two extra phase factors. One factor is the dynamical phase factor $\exp(-i\int dt' E(R(t')))$, where $E(R(t))$ is the energy, and $R(t)$ is a time ($t$) dependent parameter. This is the generalization of the evolution factor in quantum mechanics. The other factor is defined as $\gamma_n = \int_c d\mathbf{R}\cdot i\langle n(R)|\frac{\partial}{\partial \mathbf{R}}|n(R)\rangle$. If the contour $C$ is a closed loop, we obtain the Berry phase,

$$\gamma_n = \oint d\mathbf{R}\cdot i\langle n(R)|\frac{\partial}{\partial \mathbf{R}}|n(\mathbf{R})\rangle. \tag{2.12}$$

In condensed matter physics, we are mainly concerned with the Berry phase defined in a lattice system, where a non-interacting electron is described by Bloch wave functions $\psi_n(\mathbf{r}) = \mathrm{e}^{i\mathbf{kr}}u_n(\mathbf{r})$, where $n$ is the band index and $u_n(\mathbf{r})$ is periodic in space. The Berry curvature is a similar concept as the fields in electrodynamics, which is gauge invariant. The Berry curvature is defined as

$$\Omega_n(\vec{q}) = \nabla_q \times \langle\psi_n(\vec{q})|i\nabla_q|\psi_n(\vec{q})\rangle, \tag{2.13}$$

or to cast it in another way

$$\Omega^n_{\mu\nu} = i[\langle\frac{\partial\psi_n(\vec{q})}{\partial q^\mu}|\frac{\partial\psi_n(\vec{q})}{\partial q^\nu}\rangle - (\nu\leftrightarrow\mu)] \tag{2.14}$$

$$= \frac{\partial}{\partial q^\mu}A^n_\nu(\vec{q}) - \frac{\partial}{\partial q^\nu}A^n_\mu(\vec{q}). \tag{2.15}$$

This quantity is non-trivial in many materials. The quantity $\vec{A_n}(\vec{q}) = \langle\psi_n(\vec{q})|i\nabla_q|\psi_n(\vec{q})\rangle$ is called the Berry connection. The Berry phase in the Brillouin zone (Zak's phase) is defined as

$$\gamma_n = \int_{BZ} \mathrm{d}q \ \langle\psi_n(\vec{q})|i\nabla_q|\psi_n(\vec{q})\rangle. \tag{2.16}$$

The first Chern number is defined as the integral of the Berry curvature over the Brillouin zone. This quantity plays an important role in the understanding of the quantized conductivity of the integer quantum Hall effect. The Thouless-Kohmoto-Nightingale-den Nijs paper (TKNN)[12] calculated the Hall conductivity by explicitly using Kubo formula, which is the standard way to get the conductivity (see an explanation below).

Here we use a two band example to illustrate how to compute the Berry curvature, then the first Chern number (the Hall conductivity). We follow the method in [13]. We can begin with a generic two band Hamiltonian

$$h(k) = d_i(k)\sigma^i, \tag{2.17}$$

where we use Einstein's summation convention. The $\sigma^i$ $(i = 1, 2, 3)$ are three gamma matrices. The basis of this model can be spin or other two-component degree of freedom. $d_i(k)$ are three functions that explicitly depend on the momentum $k_x$, $k_y$, and $k_z$. For example, intrinsic graphene ($\mu = 0$) has $d_1 = k_x$ and $d_2 = k_y$. We write Eq.(2.17) in a matrix form

$$h(k) = \begin{pmatrix} d_3 & d_1 - id_2 \\ d_1 + d_2 & -d_3 \end{pmatrix}. \tag{2.18}$$

We can diagonalize the Hamiltonian and obtain the energy spectrum, which has

two branches (we indicate them by + and −)

$$\lambda_{\pm} = \pm\sqrt{d_1^2 + d_2^2 + d_3^2},\ \lambda = \sqrt{d_1^2 + d_2^2 + d_3^2} \tag{2.19}$$

and corresponding eigenvectors

$$\phi_+ = \frac{1}{\sqrt{2\lambda_+(\lambda_+ - d_3)}} \begin{pmatrix} d_1 - id_2 \\ \lambda_+ - d_3 \end{pmatrix}, \tag{2.20}$$

$$\phi_- = \frac{1}{\sqrt{2\lambda_-(\lambda_- - d_3)}} \begin{pmatrix} d_1 - id_2 \\ \lambda_- - d_3 \end{pmatrix}. \tag{2.21}$$

The Berry connection and the Berry curvature can be seen as analogous concepts of gauge potential and field in electromagnetism. The definition of the Berry connection gives

$$A_i = -\frac{1}{2\lambda(\lambda + d_3)}(d_2\partial_i d_1 - d_1\partial_i d_2), \tag{2.22}$$

and the Berry curvature reads

$$\Omega = \frac{1}{2\lambda^3}\epsilon_{abc} d_a \partial_i d_b \partial_j d_c \tag{2.23}$$

$$= \frac{1}{2}\hat{\mathbf{d}} \cdot \partial_i \hat{\mathbf{d}} \times \partial_j \hat{\mathbf{d}}. \tag{2.24}$$

where $\hat{\mathbf{d}} = (d_1, d_2, d_3)/\lambda$ and $\epsilon_{abc}$ is the antisymmetric Levi-Civita symbol. Inte-

grating it over the Brillouin zone, we can get

$$\sigma_{ij} = -\frac{1}{8\pi^2}\int_{BZ} \mathrm{d}^2k\ \hat{\mathbf{d}}\cdot\partial_i\hat{\mathbf{d}}\times\partial_j\hat{\mathbf{d}}, \tag{2.25}$$

which can be shown to be the Chern number of this system [10]. The integrand counts how many times the function $\hat{\mathbf{d}}$ rotates around the origin, so it is a winding number, which is an integer. This quantity also appears in other branches of physics, like Skyrmions and the analysis of the nonlinear sigma model [14].

For a generic linear 2D Hamiltonian (massive)

$$H(\vec{k}) = v_{ij}k_i\sigma_j + m\sigma_3, \tag{2.26}$$

in which $v_{ij}$ is a coefficient matrix with $i, j = 1, 2$, and $m$ stands for a mass term. Following the calculation procedure of the Berry phase, the Chern number can be shown to be

$$\sigma_{xy} = \frac{1}{2}\mathrm{sign}(m)\mathrm{sign}(\det[v]). \tag{2.27}$$

The TKNN paper [12] provides a direct link between the Kubo formula calculation of the conductivity and the Berry phase. This result can also be obtained by considering electron dynamics under the influence of EM fields [11]. For the $n$-th band, the energy eigenstate is $|u_n(q,t)\rangle$. Treating the electric field as an perturbation, the first order wave function in the perturbative expansion is

$$|u_n'\rangle = |u_n\rangle - i\hbar\sum_{n'\neq n}\frac{|u_{n'}\rangle\langle u_{n'}|\partial u_n/\partial t\rangle}{E_n - E_{n'}}. \tag{2.28}$$

The velocity operator of the electron is $v = \partial H/\partial k$. After some algebra, the first

order value of the velocity is

$$v_n(q) = \langle u_n'|\frac{\partial H}{\partial k}|u_n'\rangle = \frac{\partial E_n(q)}{\hbar\partial q} - i[\langle\frac{\partial u_n}{\partial q}|\frac{\partial u_n}{\partial t}\rangle - \langle\frac{\partial u_n}{\partial t}|\frac{\partial u_n}{\partial q}\rangle]$$
$$= \frac{\partial E_n(q)}{\hbar\partial q} - \Omega^n(q,t). \tag{2.29}$$

The second term on the right is just the Berry curvature. Then we would see the connection between the current and the Berry phase.

## 2.3 Dirac and Weyl semimetal

In the context of four dimensional relativistic quantum mechanics, a Dirac fermion can be seen as a combination of one left-handed Weyl fermion and one right-handed Weyl fermion. In the massless case, the Dirac equation becomes [44]

$$\begin{pmatrix} 0 & i\sigma\cdot\partial \\ i\bar{\sigma}\cdot\partial & 0 \end{pmatrix}\begin{pmatrix} \psi_L \\ \psi_R \end{pmatrix} = 0, \tag{2.30}$$

where $\bar{\sigma} \equiv (1, \sigma)$.

In the condensed matter community, the solid state realizations of Dirac and Weyl fermions in 3D attract much attention [45][47], and these materials are called Dirac semimetals and Weyl semimetals.

In Weyl semimetals, the low energy excitations are Weyl-fermion-like quasi-particles around several nodal Fermi points. The low energy Hamiltonian has the form:

$$H_W = \sum_\alpha a_1(\mathbf{k}_\alpha)\sigma^1 + a_2(\mathbf{k}_\alpha)\sigma^2 + a_3(\mathbf{k}_\alpha)\sigma^3, \tag{2.31}$$

where $\sigma^i$ are Pauli matrices. This Hamiltonian describes two non-degenerate

bands touching at nodal points $k_0$'s in the Brillouin zone such that $a_\alpha = 0$. The generally non-degenerate bands rely on the symmetries of the system. In Weyl semimetals, either inversion or time-reversal symmetry is broken.

In Dirac semimetals, the system is both inversion and time-reversal symmetric. The bands are generally degenerate. The low-energy Hamiltonian is Dirac-like as Eq.(2.30).

## 2.4 Topological properties of Weyl materials

As an illustration of the role of topology in nodal materials, we analyze some of topological properties of a Weyl semimetal. One can compute the Berry flux going through a closed sphere enclosing a Weyl point. The result turns out to be 1 or $-1$. The common explanation is that Weyl points can be treated as monopoles ("Berry monopole") in the Brillouin zone. To see this, a widely used two-band model can be a good starting point. The Hamiltonian is

$$\begin{aligned} H = &-\sum_{\vec{k}}[2t_x(\mathrm{cos}k_x - \mathrm{cos}k_0) + m(2 - \mathrm{cos}k_x - \mathrm{cos}k_y)]\sigma_x \\ &+ 2t_y \mathrm{sin}k_y \sigma_y + 2t_z \mathrm{sin}k_z \sigma_z. \end{aligned}$$

$m$, $t_i$ are model parameters. To calculate the spectrum of the model, on would see two zeros located at $\pm k_0$, and there are the Weyl points of the model. The "Berry monopole" described above can be revealed by calculating the flux of the

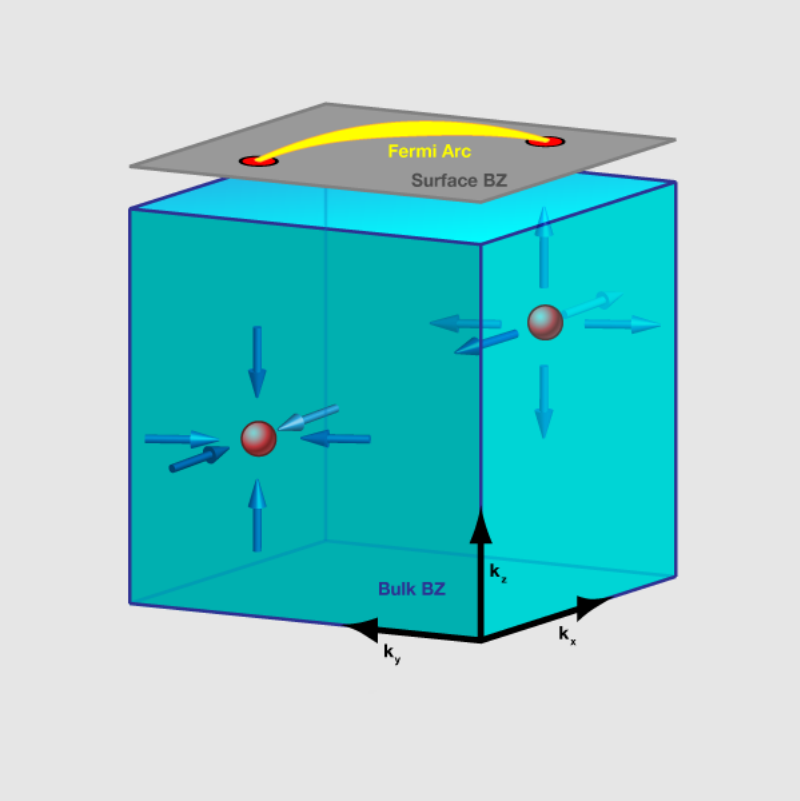


Figure 2.2: Two Weyl points are shown as small red balls, and the arrows indicate the flux of the Berry curvature. The Fermi arc is shown in the grey plane, which is the surface Brillouin zone. The figure is from [46].

gauge field $\vec{A}$ and its "magnetic field" is defined as $\vec{B}$

$$\vec{A}(\vec{k}) = -i \sum_{n,\text{filled}} \langle \psi_{n,k} | \nabla_k | \psi_{n,k} \rangle \tag{2.32}$$

$$\vec{B}(\vec{k}) = \vec{\nabla}_k \times \vec{A}(\vec{k}). \tag{2.33}$$

The flux around the two Weyl point are $\pm 2\pi$. Consider a 2D slice of the system at a given $k_z$, the two dimensional Hamiltonian $H_r(k_x, k_y)$ is gapped if $k_z$ is away from the Weyl points (the system is everywhere gapped except at Weyl points). In a time-reversal broken gapped 2D system, one can calculate the Chern number which characterized the Hall conductivity, which means we

can treat this fixed $k_z$ slice as a two dimensional integer quantum Hall system. This observation can be used as an argument to see the existence of the exotic surface states of Weyl semimetal. An integer quantum Hall system hosts chiral edge states moving along the edge. If the Weyl semimetals are seen as a stack of integer quantum Hall systems, then the Weyl semimetal hosts surface states due to the chiral modes in 2D. These 2D surface states of the Weyl semimetal are named "Fermi arc".

Weyl semimetals have special transport properties due to Weyl points and the chiral anomaly. A very nice thing about Weyl semimetals is that they provide a condensed matter demonstration of a chiral anomaly. The Jacobian introduced by the chiral transformation adds a new term into the Lagrangian [50]

$$S_\theta = -\frac{e^2}{8\pi^2}\int \mathrm{d}t\ \mathrm{d}^3x\ \partial_\mu\theta\ \epsilon^{\mu\nu\rho\sigma}A_\nu\partial_\rho A_\sigma \tag{2.34}$$

where $\theta = 2b_{mu}x_\mu$, $b_\mu$ characterizes the distance between $k_{R/L}$ in the Brillouin zone. This term introduces current which has the following effects, for more details see [50][51]:

- the anomalous Hall effect: $j_\nu = \frac{e^2}{2\pi^2}b_\mu\epsilon^{\mu\nu\rho\sigma}\partial_\rho A_\sigma$
- the chiral magnetic effect: $j_\nu = \frac{e^2}{2\pi^2}b_0\epsilon^{0\nu\rho\sigma}\partial_\rho A_\sigma$

For the experimental aspects, in 2015 Weyl semimetal and Fermi arcs were observed in tantalum arsenide(TaAs) by ARPES measurements [48, 49]. Transport properties are also intensively investigated [52, 53].

# Chapter 3

# Quasiparticle renormalization in ABC-stacked trilayer graphene

## 3.1 Overview

The low energy spectrum of a few-layer graphene sample strongly depends on how single graphene layers are stacked. For trilayer graphene, a particularly interesting stacking pattern is the ABC stacking. In ABC trilayer graphene, the low energy dispersion is cubic in momentum and quasiparticles have a $3\pi$ Berry phase. We study the many-body effects due to Coulomb interactions in an ABC graphene trilayer in the large $N$ limit. Using renormalization group techniques, we obtain the renormalization of the dynamical exponent, which is renormalized to $z = 3 + \alpha_1/N$, with $\alpha_1 \approx 0.5$ and $N$ is the number of fermionic species. We also analyze the properties of the quasiparticles, including the lifetime and quasiparticle residue. The quasiparticles are robust but acquire non-Fermi liquid renormalization effects which lead to possible signatures in experiments. We also calculate how other physical observables, such as the electronic compressibility

and the specific heat, are affected by Coulomb interactions.

## 3.2 Background

### 3.2.1 Trilayer graphene systems

Multilayer graphene systems have quite distinct electronic properties from a single layer graphene film. This is largely due to the inter-layer couplings and the pattern of stacking graphene layers. There are two kinds of stacking forms which are known in the bulk graphite: ABA form (also called Bernal) and ABC form (also called rhombohedral). These two stacking patterns are shown in Fig. 3.1(from [18]).

For the ABA multilayer, the two adjacent layers can be seen as being displaced horizontally by a vector $\vec{r}_{AB}$ which points from the sublattice A to the sublattice B in a single graphene layer. In ABC multilayers, three successive layers can be seen as being displaced by two different vectors pointing to B sub-sites from the A sub-site. The energy spectrum properties of these two multilayers are different. In ABA graphene multilayers, the Hamiltonian can be decomposed around the $K$ point into a set of AB-stacked graphene bilayers and graphene monolayers. For a ABA trilayer, the Hamiltonian can be decomposed into one graphene monolayer and one graphene bilayer. Here we set $\gamma_0$ to be the nearest-neighbor hopping constant in the plane, and $\gamma_1$ is the perpendicular hopping. The eigenvalues of the single layer part are $\epsilon_0 = svp$, and the eigenvalues of the bilayer part are $\epsilon_2 = s[\mu\gamma_1 \cos\kappa_2 + \sqrt{(\gamma_1 \cos\kappa_2)^2 + (vp)^2}]$, where $\mu = \pm 1$, $s = \pm 1$, $p = \sqrt{p_x^2 + p_y^2}$, and $\kappa_2 = \pi/4$.

For the ABC-stacked trilayer, the focus of this chapter, the low energy degrees

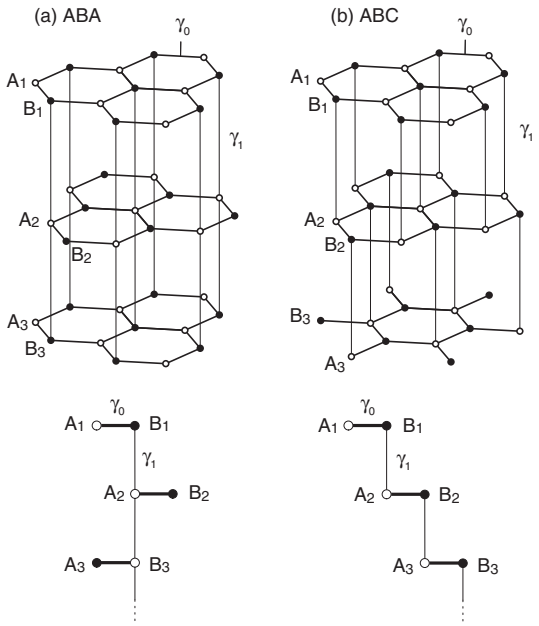


Figure 3.1: ABA stacking pattern and ABC stacking pattern. This figure is from [18]

of freedom are those on the top and the bottom layer of the system [18][19][24]. The low energy Hamiltonian around the K point is

$$H_{\text{tri}} = \frac{v^3}{\gamma_1^2} \begin{pmatrix} 0 & (\pi^\dagger)^3 \\ \pi^3 & 0 \end{pmatrix}, \tag{3.1}$$

where $\pi = p_x + ip_y$. For the ABC case, generalization to $N$ layers is straightforward: the energy band grows as $\epsilon \approx s\gamma_1(vp/\gamma_1)^N$. The band becomes flatter. By using this simplified model for the low energy degrees of freedom, the density of states grows as $D(\epsilon) \sim \epsilon^{(2-N)/N}$. For $N > 2$, the density of states $D(\epsilon)$ diverges as $\epsilon$ goes to zero.

From the perspective of experiments, the ABC-stacked trilayer graphene has some attractive properties [15], such as a gap observed which may provide promising guidance for future applications. Depending on the stacking pattern, the elec-

tric structures of graphene trilayer can be quite different. While an ABA-stacked graphene trilayer always exhibits a gapless metallic phase in the presence of an external electric field, the ABC-stacked trilayer is found to possess a tunable gap [16][17]. Interactions among quasiparticles in graphene trilayer are critical to its electric properties. Without external fields, a 6meV gap was reported in [17], which is believed to be induced by the interactions in the ABC-stacked graphene trilayer.

### 3.2.2 Large N

In this section, I briefly review the large $N$ technique used in the calculation in this chapter, and the main references of this part are [20][21] . In the study of strong coupling field theories, the perturbative calculations in the successive orders of the coupling constant break down. For example, in asymptotic free theories like QCD, the coupling grows as the energy scale increases, which hinders the use of a perturbative method in the coupling constant in the high energy regime. One route is looking for another parameter other than the coupling constant to perform the perturbative calculation.

One class of such method is the $1/N$ expansion, where $N$ comes from the symmetry group of the theory, for example $SU(N)$ or $SO(N)$ groups. In statistical mechanics, for $O(N)$ symmetric systems, the large $N$ limit results are better than the mean field level results. The large $N$ analysis can be summarized in several steps. First, one should choose a proper parameter $t_0$, such that $t_0 = Ng_0^2$. $g_0$ is the coupling constant of the theory. The large $N$ limit corresponds to $N \to \infty$, $g_0 \to 0$. Second, introducing an ancillary field which serves as a Lagrangian multiplier. This field helps to count the $1/N$ powers. Third, we integrate out the

original fields and obtain the effective Hamiltonian of the ancillary field. Fourth, diagrammatic calculations in the ancillary field are carried out, while in this calculation the propagator is always proportional to $1/N$. For more details, see [20] and [21].

In this work, we use the large $N$ expansion to organize the diagrammatic calculations. In this calculation about graphene, a simplified structure of the polarization function can also be obtained. In the large $N$ approximation, the dressed Coulomb interaction scales as $\frac{1}{N}$ which helps the bookkeeping of the expansion terms. The polarization function in one loop can be calculated as

$$\Pi^{(0)}(q,\omega) = -\frac{2N}{\beta}\sum_{ip_n}\int \frac{\mathrm{d}^2 p}{(2\pi)^2}\frac{1}{i\omega + ip_n - E(\mathbf{p}+\mathbf{q})}\frac{1}{ip_n - E(\mathbf{p})}, \tag{3.2}$$

where the prefactor $N$ is the flavor of the fermions. For single layer graphene after tracing out the sublattice indices, this number is $N = 4$, i.e. two valleys, and two spins.

The effective interaction function is

$$\tilde{V}(\mathbf{q},\omega) = \frac{V(\mathbf{q})}{1 - \Pi(\mathbf{q},\omega)V(\mathbf{q})}, \tag{3.3}$$

If $N$ is large, the effective interaction becomes

$$\tilde{V}(\mathbf{q},\omega) \sim -\frac{1}{\Pi(\mathbf{q},\omega)}, \tag{3.4}$$

which no longer depends on the bare interaction $V(\mathbf{q})$. In each order of $1/N$, an infinite numbers of diagrams are taken into account.

## 3.3 Interactions

In this chapter we study the effect of Coulomb interactions and polarization effects on the behavior of the quasiparticles at small but finite temperature, when the many-body gap is zero. Because of the scaling of the kinetic energy, Coulomb interactions are relevant operators in the renormalization group (RG) sense, and can strongly renormalize different physical quantities. Different spontaneous broken symmetry ground states have been already proposed for trilayer graphene [25, 26, 27]. Very recently, transport experiments revealed a robust many-body gap of $\sim$40 meV at temperatures below $T_c \sim 34$K [139].

We investigate the analytical structure of the polarization bubble and the leading self-energy corrections due to dynamically screened Coulomb interactions. In the gapless regime, we show that the dynamical critical exponent is renormalized to

$$z = 3 + \alpha_1/N + O(N^{-2}),$$

where $\alpha_1 \approx 0.52$ and $N = 4$ is the number of fermionic flavors. Although the quasiparticle residue is suppressed by interactions, the scattering rate has a sublinear scaling with energy and the quasiparticles remain well defined. We predict the renormalization of several physical observables in the metallic phase, such as the electronic compressibility, the specific heat, the density of states (DOS) and the spectral function, which can be measured with angle resolved photoemission spectroscopy (ARPES) experiments.

## 3.4 Low energy Hamiltonian

We start with a simplified two-band model where the high energy bands are separated in energy by interlayer hopping processes, which set the ultraviolet cut-off for the excitations in the low-energy bands, $t_\perp \sim 0.4$eV. We will assume a temperature regime above the ordering temperature $T \gtrsim T_c \sim 4$ meV, where the band structure is gapless. The infrared cut-off of the model is the trigonal warping energy $\sim 10$ meV, below which the bands disperse quadratically [24].

The low energy physics of the non-interacting ABC-trilayer in the gapless regime is described by the $2 \times 2$ Hamiltonian $\mathcal{H}_0 = \sum_{\mathbf{p}} \Psi^\dagger_{\mathbf{p}} \hat{\mathcal{H}}_0(\mathbf{p}) \Psi_{\mathbf{p}}$, where $\Psi_{\mathbf{k}} = (a_{,\mathbf{k}}, \bar{b}_{,\mathbf{k}})$ is a two component spinor defined in terms of one annihilation operator in sublattice $A$ of the top layer ($a_{\mathbf{p}}$) and another in sublattice $B$ for the bottom layer ($\bar{b}_{\mathbf{p}}$). The total degeneracy is $N = 4$, including spin and valley degrees of freedom. The Hamiltonian density operator is [169, 24], which is introduced in Eq. (3.1)

$$\hat{\mathcal{H}}_0 = \frac{(\hbar v)^3}{t_\perp^2} \begin{pmatrix} 0 & (\pi)^3 \\ (\pi^\dagger)^3 & 0 \end{pmatrix}, \tag{3.5}$$

where $\hbar v \approx 6$ eVÅ is the Fermi velocity, and $\pi = p_x - i p_y$ is defined by the $x$ and $y$ components of the in-plane momentum of the quasiparticles measured away from the neutrality point. In a more compact notation, $\hat{\mathcal{H}}_0(\mathbf{k}) = \gamma |\mathbf{k}|^3 \hat{h}_0(\mathbf{k})$ with

$$\hat{h}_0(\mathbf{k}) = \cos(3\theta_{\mathbf{k}})\sigma^1 + \sin(3\theta_{\mathbf{k}})\sigma^2, \tag{3.6}$$

where $\sigma^i$ $(i = 1, 2)$ are Pauli matrices, and $\tan\theta_{\mathbf{k}} = k_y/k_x$. The constant $\gamma \equiv (\hbar v)^3/t_\perp^2$, is proportional to the velocity of the quasiparticles $\mathbf{v}_0 = \partial_{\mathbf{k}} E_{\mathbf{k}}$, which have the energy spectrum $\pm E_{\mathbf{k}} = \pm\gamma |\mathbf{k}|^3$.

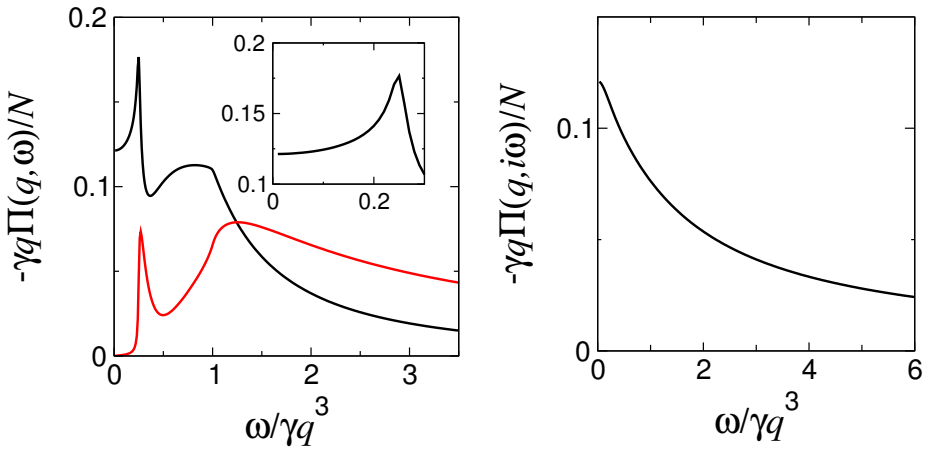


Figure 3.2: Left: Polarization bubble in one loop calculated numerically. The real part (black curve) has a logarithmic singularity at the edge of the particle-hole continuum, at $\omega = \gamma q^3/4$, shown in detail in the inset. Red curve: imaginary part. Right panel: Polarization in imaginary frequencies, which is a purely real function. For $\omega/\gamma q^3 \gg 1$, $\Pi^{(0)}(q, i\omega) \to -3Nq^2/(16\omega)$ (see text).

In ABC trilayers, Coulomb interactions are relevant in the RG flow at the tree level, and hence standard perturbation theory is not possible. We organize the expansion of the self-energy corrections in powers of the dynamically screened Coulomb interaction, which can be rigorously justified in the large $N$ limit. At long wavelengths, $k \ll 1/d$, where $d \sim 2.4$Å is the interlayer distance, the bare Coulomb interaction is

$$\mathcal{H}_I = \frac{1}{2}\sum_{\mathbf{q}} V(q)\hat{n}(\mathbf{q})\hat{n}(-\mathbf{q}), \tag{3.7}$$

with $\hat{n}(\mathbf{q})$ a density operator and $V(q) \approx 2\pi e^2/q$, as in a 2D system. In the long wavelength regime where this approximation is valid, the DOS scales as $\rho(\mathbf{q}) = (6\pi\gamma)^{-1}/q$ and the screened Coulomb interaction is $\tilde{V}(q,\omega) = V(q)/\left[1 - V(q)\Pi(\mathbf{q},\omega)\right]$, where $\Pi(\mathbf{q},\omega)$ is the dynamical polarization function. In trilayers, the large $N$ approximation becomes asymptotically exact at small momentum, where the DOS diverges and screening becomes strong.

## 3.5 Polarization bubble

In order to address the screening effects, we consider the bare polarization function, which is defined as $\Pi^{(0)}(\mathbf{q},\omega) = \frac{1}{\beta}\mathrm{tr}\sum_{i\nu}\sum_{\mathbf{p}}\hat{G}_0(\mathbf{p},i\nu)\hat{G}_0(\mathbf{p}+\mathbf{q},i\omega+i\nu)$, where

$$\hat{G}_0(\mathbf{q},i\omega) = \frac{1}{2}\sum_{s=\pm}\frac{1+s\hat{h}_0(\mathbf{q})}{i\omega - s\gamma q^3} \tag{3.8}$$

is the fermionic Greens function, described by a 2×2 matrix. After performing the sums over the Matsubara frequencies, the polarization function is given by

$$\Pi^{(0)}(\mathbf{q},\omega) = -\frac{N}{2}\int\frac{d^2p}{(2\pi)^2}\sum_{s=\pm}\frac{1-\cos(3\theta_{\mathbf{pq}})}{E_{\mathbf{p+q}}+E_{\mathbf{p}}-s\omega} \tag{3.9}$$

where $\theta_{\mathbf{pq}} = \theta_{\mathbf{p+q}} - \theta_{\mathbf{p}}$ is the angle between vectors $\mathbf{p}+\mathbf{q}$ and $\mathbf{p}$. By sending the ultraviolet cut-off to infinity, a simple dimensional analysis reveals the functional form of the polarization function to be $\gamma q\Pi^{(0)}(\mathbf{q},i\omega) = -Nf(i\omega/(\gamma q^3))$. After some algebra, the scaling function $f(z)$ can be written in the form

$$\begin{aligned} f(iz) = &\frac{1}{2}\int_0^{2\pi}\mathrm{d}\theta\int_0^{\infty}\frac{\mathrm{d}x\,x}{(2\pi)^2}\sum_{s=\pm}\frac{s}{iz+s\left[x^3+h^3(x,\theta)\right]} \\ &\times\left[1-4\left(\frac{1+x\cos\theta}{h(x,\theta)}\right)^3+3\left(\frac{1+x\cos\theta}{h(x,\theta)}\right)\right], \end{aligned} \tag{3.10}$$

where $z = \omega/(\gamma q^3)$ and $h(x,\theta)\equiv\sqrt{1+x^2+2x\cos\theta}$. $f(z)$ is a well-defined function in imaginary frequency but has branch cuts related to the edge of the particle-hole continuum on the real axis. Due to the cubic dispersion, it is difficult to come up with a closed form solution for the polarization function. However the analytical structure of $f(z)$ near the particle-hole threshold $z = 1/4$ can be ex-

tracted in the collinear scattering approximation, which dominates the processes near that region [30]. We consider the singular contribution of the integrand around the momenta $\mathbf{p}+\mathbf{q} \approx -\mathbf{p}$. Within this window it is safe to assume $1-\cos(3\theta_{\mathbf{pq}}) \approx 2$. After expanding $\cos\theta$ around $\theta=\pi$ to the second order, we arrive at the following integral representation for $f(z)$,

$$f(z) \cong \int \frac{xdx}{(2\pi)^2} \int \frac{d\theta}{x^3+(1-x)^3+\frac{3}{2}x(1-x)\theta^2-z}. \tag{3.11}$$

Considering the rapid fall of the integrand with respect to $\theta$ around $\pi$, one can conveniently extend the upper limit of the angular integral to infinity, $\theta \in [0,\infty[$. After performing the integrals, we arrive at the most dominant part of $f(z)$ near $z \sim 1/4$,

$$f(z) = -\frac{1}{6\sqrt{2}\pi} \ln(1-4|z|) + \text{regular terms}, \tag{3.12}$$

which describes a logarithmic divergence near the edge of the particle hole continuum. Exploring the two asymptotic regimes, in the $z \to 0$ regime, $f(0) = c_0 \approx 0.12$ is a constant [11, 31] and in the $z \gg 1$ limit, $f(z) \to -ic_\infty/z$ is purely imaginary, with $c_\infty = 3/16$.

In Fig. 3.2, we show the behavior of the real and imaginary parts of $f(z)$ calculated numerically from Eq. (A.3). The scaling function has only one singularity near $z \sim 1/4$. For $z < 1/4$, $f(z)$ is purely real and diverges logarithmically at $z = 1/4$, in agreement with the analytical expression (3.12), as shown in the inset of Fig. 3.2. For $z > 1/4$, $f(z)$ has also an imaginary part, which decays with $1/z$. The right panel of Fig. 3.2 shows $f(iz)$ in imaginary frequency, which is a real and well behaved monotonic function.

In the optical regime, for $z \gg 1$, where $\Pi^{(0)}(q,\omega) \to iNc_\infty q^2/\omega$, the optical

conductivity can be calculated directly from the charge polarization,

$$\sigma(\omega) = \frac{e^2}{\hbar} \lim_{q\to 0} \frac{i\omega}{q^2} \frac{\Pi^{(0)}(\mathbf{q},\omega)}{1 - V(q)\Pi^{(0)}(\mathbf{q},\omega)} = \frac{3}{4}\frac{e^2}{\hbar}, \tag{3.13}$$

which is proportional to the Berry phase $3\pi$. In the general case, $\sigma(\omega) = \nu e^2/(2h)$, with $\nu = \pi$ for graphene single layer and $\nu = 2\pi$ for bilayers.

## 3.6 Self-energy

The leading self energy correction due to the screened Coulomb interaction is diagrammatically shown in Fig. 3.3. In imaginary time, the self-energy is given by

$$\hat{\Sigma}^{(1)}(\mathbf{q}, i\omega) = -\frac{1}{\beta}\sum_{\nu} \int \frac{\mathrm{d}^2 p}{(2\pi)^2} \tilde{V}(\mathbf{p}, i\nu)\hat{G}^{(0)}(\mathbf{q}-\mathbf{p}, i\omega - i\nu). \tag{3.14}$$

Through power counting, the leading divergences appear at long wavelengths, where the large $N$ limit is a good approximation. At large $N$, the dynamically screened potential is approximated by $\tilde{V}(\mathbf{q}, i\omega) \approx \gamma q/[Nf(i\omega/\gamma q^3)] + O(N^{-2})$ [33, 34, 35]. Since $f(iz)$ is a well behaved function, with no singularities or branch cuts, the self energy in one loop can be calculated directly in the zero temperature limit. The leading contribution is logarithmically divergent,

$$\Sigma^{(1)}(\mathbf{q}, i\omega) = \frac{1}{2\pi^2 N}\left[\alpha_d i\omega + \alpha_o \gamma q^3 \hat{h}(\mathbf{q})\right] \ln\left(\frac{\Lambda}{q}\right), \tag{3.15}$$

where $t_\perp = \gamma\Lambda^3$ defines the ultraviolet cut-off in momentum, namely $\Lambda = t_\perp/(\hbar v)$. The coefficients

$$\alpha_o = \int_0^\infty dz \frac{1}{f(iz)} \frac{z^2(10 - 16z^2 + z^4)}{(1+z^2)^4}, \tag{3.16}$$

and

$$\alpha_d = \int_0^\infty dz \frac{1}{f(iz)} \frac{1-z^2}{(1+z^2)^2}, \tag{3.17}$$

can be found though numerical integration using the exact $f(iz)$. Although $\alpha_o$ and $\alpha_d$ both diverge logarithmically with the upper limit of integration at large $z$, we will postpone their regularization for the moment, since these divergences cancel exactly in the renormalization of $\gamma$ and hence have no consequence to the renormalization of the spectrum.

The self-energy can be separated in two terms, $\hat{\Sigma}(\mathbf{q}, i\omega) = i\omega\Sigma_d\sigma_0 + \Sigma_0 q^3 \hat{h}_0(\mathbf{q})$, where $\Sigma_d$ is the diagonal term, and $\Sigma_o$ describes the off-diagonal matrix elements. The diagonal part of the self-energy has frequency dependence and defines the quasiparticle residue renormalization,

$$Z_\psi^{-1} = 1 - \partial\hat{\Sigma}/\partial(i\omega) = 1 - \Sigma_d. \tag{3.18}$$

The renormalized Green's function is $\hat{G}(\mathbf{q}, i\omega) = Z_\psi[i\omega - \gamma\hat{h}_0(\mathbf{q})Z_\psi(1+\Sigma_o)]^{-1}$. In one loop, the renormalized energy spectrum is

$$\frac{\gamma(q)}{\gamma} = \frac{1+\Sigma_o}{1-\Sigma_d} \approx 1 - \frac{\alpha_1}{N} \ln\left(\frac{\Lambda}{q}\right) + O(1/N^2), \tag{3.19}$$

where

$$\alpha_1 = \frac{\alpha_0 + \alpha_d}{2\pi^2} = \int_0^\infty \frac{\mathrm{d}z}{2\pi^2} \frac{1}{f(iz)} \frac{17z^4 - 11z^2 - 1}{(1+z^2)^4} \approx 0.52 \tag{3.20}$$

is a finite well defined quantity.

The logarithmic renormalization of the quasiparticle velocity in one loop dic-

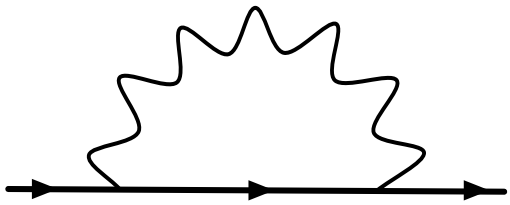

Figure 3.3: One-loop correction to the self-energy with the dressed Coulomb interaction.

tates the RG equation of $\gamma$,

$$\beta_\gamma \equiv \frac{\mathrm{d}\gamma}{\mathrm{d}l} = -\gamma\frac{\alpha_1}{N}, \tag{3.21}$$

where $l = \ln(\Lambda/\Lambda')$, with $\Lambda' < \Lambda$ the renormalized cut-off, whose solution is

$$\gamma(q) = \gamma \times [(\hbar v/t_\perp)q]^{\alpha_1/N}. \tag{3.22}$$

The energy spectrum acquires an anomalous dimension $\eta = \alpha_1/N$, which leads to the renormalization of the dynamical exponent, $\omega \propto q^z$, with $z = 3 + \alpha_1/N + O(N^{-2})$. This result can be related with the graphene bilayer case, where $\eta = 0.078/N$ [36] and with the large $N$ limit of the single layer case, where $\eta = -4/(\pi^2 N)$ [33, 34].

This analysis can be explicitly verified by checking the two loop correction in the self energy. The RG equation describes a resummation of leading logs to all orders in $1/N$. The $N^{-2}\log^2$ terms cancel exactly in the vertex correction diagram at two loop, and hence vertex corrections do not renormalize in the RG flow [36]. The leading logarithmic terms appear in the remaining diagrams of the same order, and lead to a second order correction to Eq. (3.19), $\gamma^{(2)}(q)/q = \frac{1}{2}\alpha_1^2/N^2 \ln^2(\Lambda/q)$, in agreement with the result of the RG equation up

to $1/N^2$ order.

## 3.7 Quasiparticle residue

To calculate the quasiparticle residue renormalization $Z_\psi$ through Eq. (3.18), one needs to regularize integral (3.17). That can be done introducing an upper cut-off $z_c$ which accounts for the condition where the large $N$ limit breaks down, namely $-V(p)\Pi^{(0)}(p,i\nu) = 2\pi N e^2\Lambda^2/(\hbar v p^2) f(iz_c) \sim 1$. At large $z$, where $f(iz) \to 3/(16z)$, the leading contribution is $\alpha_d \sim -16\ln(\Lambda/p)$. Replacing $\ln(\Lambda/q) \to \int_q^\Lambda \mathrm{d}p/p$ in Eq. (3.15) and carrying out the momentum integration, the quasiparticle residue $Z_\psi$ is given by

$$Z_\psi^{-1} \to 1 + \frac{4}{\pi^2 N}\ln^2(\Lambda/q) + O(1/N^2), \tag{3.23}$$

in one loop, and is suppressed logarithmically in the infrared.

In the RG spirit, we now reestablish the bare value of the quasiparticle residue $Z_0$ in the bare Green's function $\hat{G}_0 \propto Z_0$ [158], and set $Z_0 \to 1$ at the end. Since $\delta\hat{G} = \hat{G}_0\hat{\Sigma}\hat{G}_0 \propto \delta Z_\psi$ in lowest order in the Dyson equation, then $\delta Z_\psi = Z_0^2\hat{\Sigma}_d \propto Z_0$ in large $N$. Eq. (3.23) then becomes $\delta Z_\psi = -4Z_0/(\pi^2 N)\delta\ln^2(\Lambda/q)$, which corresponds to the RG equation

$$\beta_\psi = \frac{\mathrm{d}Z_\psi}{\mathrm{d}l} = -\frac{8}{\pi^2 N} l Z_\psi, \tag{3.24}$$

with $l = \ln(\Lambda/\Lambda')$, whose solution is

$$Z_\psi(q) = \exp\left[-4/(\pi^2 N)\ln^2(\Lambda/q)\right], \tag{3.25}$$

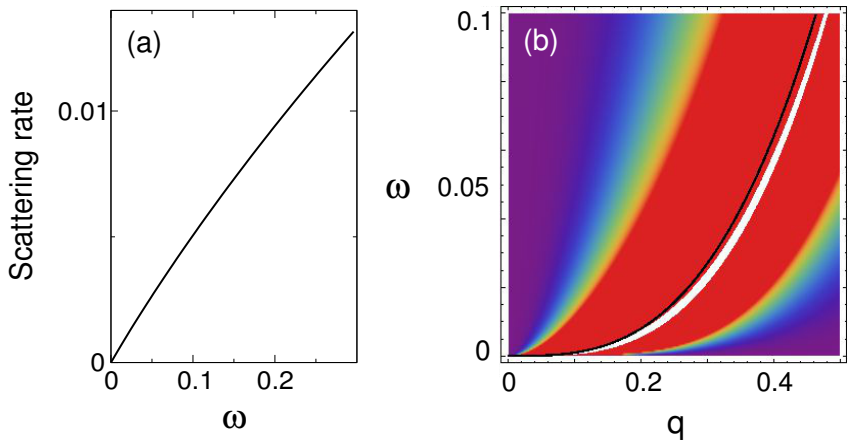


Figure 3.4: a) On-shell scattering rate $\tau(\omega)$ vs energy in units of $t_\perp \sim 0.4$eV. b) Density plot of the spectral function as a function of energy $(\omega/t_\perp)$ and momentum $(q/\Lambda)$. Solid black line: bare energy spectrum. White line: renormalized one. Light regions indicate higher intensity.

in agreement with Eq. (3.23) up to $1/N$ order.

## 3.8 Quasiparticle lifetime

In real frequency, the polarization function has a logarithmic branch cut. To calculate the quasiparticle scattering rate $\tau = Z_\psi \mathrm{Im}\hat{\Sigma}$, we use the method in ref. [38] to separate the self-energy into the line part and the residue part, $\hat{\Sigma} = \hat{\Sigma}_{\mathrm{line}} + \hat{\Sigma}_{\mathrm{res}}$. The line part is obtained by performing Wick rotation $i\omega \to \omega + i0_+$ in the self-energy (3.14), and is purely real. The residue part follows from the residue calculated around the pole of the Green's function,

$$\Sigma^{(1)}_{\mathrm{res}}(\mathbf{q},\omega) = -\frac{1}{2}\sum_{s=\pm}\int \frac{\mathrm{d}^2 p}{(2\pi)^2}\tilde{V}(|\mathbf{q}|,\omega)[1+s\hat{h}(\mathbf{q}-\mathbf{p})]$$
$$\times[\theta(\omega - s\gamma|\mathbf{q}-\mathbf{p}|^3) - \theta(-s\gamma|\mathbf{q}-\mathbf{p}|^3)], \tag{3.26}$$

with $\theta$ a step function. The scattering rate is given by $\tau(\mathbf{q},\omega) = Z_\psi \mathrm{Im}\Sigma_{\mathrm{res}}(\mathbf{q},\omega)$. In the on-shell region, near $\omega \sim \gamma q^3$, $\tau(\omega) = \omega Z_\psi g(\omega/t_\perp)$, where

$$g(y) = \frac{1}{2N}\,\mathrm{Im}\int_{|\mathbf{x}|<1} \frac{\mathrm{d}^2x}{(2\pi)^2} \frac{|\hat{q}-\mathbf{x}|}{\bar{\alpha}y^{2/3}|\hat{q}-\mathbf{x}|^2 + f\left(\frac{1-x^3}{|\hat{q}-\mathbf{x}^3|}\right)} \tag{3.27}$$

is a scaling function in one loop, with $y = \omega/t_\perp$, $\bar{\alpha} = \hbar v/(2\pi N e^2)$ is a dimensionless constant and $\hat{q} = \mathbf{q}/q$. The function $g(y)$ has a very slow variation, as shown in Fig. 3.4 a, and as a consequence $\tau(\omega) \sim \omega Z_\psi[(\omega/\gamma)^{1/3}]$ has a sublinear scaling with energy within logarithmic accuracy. In the large $N$ limit ($\bar{\alpha} \to 0$), which is valid at low energy, $g(y) \approx 0.043$ is a constant. Since the ratio $\tau(\omega)/\omega \ll 1$, the quasiparticles are well defined even in the $\omega \to 0$ limit.

The spectral function is given by $A(\mathbf{q},\omega) = -2\mathrm{tr}\,\mathrm{Im}G^R(\mathbf{q},\omega)$, where

$$\hat{G}^R(\mathbf{q},\omega) = \frac{1}{2}\sum_{s=\pm} \frac{Z_\psi(q)[1+s\hat{h}_0(\mathbf{q})]}{\omega - s\gamma(q)q^3 - i\tau(\omega) + i0^+} \tag{3.28}$$

is the retarded part of the renormalized Green's function. The spectral function is shown in Fig. 3.4b. The solid black line describes the bare energy spectrum, while the light region describes the renormalized one, which corresponds to the pole of the renormalized Green's function. There is a clear deviation of the two curves, which could be observed with ARPES experiments.

## 3.9 Other physical observables

The renormalization of the quasiparticle velocity encoded in the RG flow of $\gamma$ leads to the renormalization of many physical observables. For instance, the specific heat for non-interacting particles with cubic dispersion in 2D scales with

$C \sim (T/\gamma)^{2/3}$, where $T$ is the temperature. From Eq. (3.22), the scaling of $\gamma$ with energy is $\gamma \sim \omega^{\alpha_1/(3N)}$. At $\omega \sim T$, the temperature scaling of the specific heat is renormalized to

$$C \sim T^{2(1-\alpha_1/(3N)]/3} \approx T^{2/3-0.1/N}, \tag{3.29}$$

neglecting slower logarithmic corrections due to the scaling of $Z_\psi$, with $T \gtrsim T_0$, where $T_0$ is defined by the infrared energy cut-off of 10 meV due to trigonal warping effects [24]. In the same way, the renormalized DOS is $\rho(q) = [6\pi\gamma(q)]^{-1}/q \sim q^{-(1+\alpha_1/N)}$, which can be measured directly on surfaces with scanning tunneling spectroscopy experiments [150, 40]. In scanning tunneling spectroscopy experiments, the variation of the tunneling current with respect to the bias voltage is related to the surface density of states.

In 2D systems, the electronic compressibility can be characterized with single electron transistor measurements [41]. By dimensional analysis, the free electronic compressibility scales with temperature as $\kappa \sim \gamma^{-2/3}T^{-1/3}$ [42]. In the same spirit, interactions renormalize the scaling of the inverse compressibility,

$$\kappa^{-1} \sim T^{[1+2\alpha_1/(3N)]/3} \approx T^{1/3+0.1/N}, \tag{3.30}$$

which strongly deviates from the non-interacting result.

In summary, we derived the effect of electron-electron interactions in the renormalization of a variety of different physical observables in the metallic phase of ABC graphene trilayers.

# Chapter 4

# Designing Quantum Spin-Orbital Liquids in Artificial Mott Insulators

## 4.1 Overview

Quantum spin-orbital liquids are experimentally elusive strongly correlated states of matter that emerge from quantum frustration between spin and orbital degrees of freedom. A promising route towards the observation of those states is the creation of artificial Mott insulators where antiferromagnetic correlations between spins and orbitals can be designed. We show that Coulomb impurity lattices on the surface of gapped honeycomb substrates, such as graphene on SiC, can be used to simulate SU(4) symmetric spin-orbital lattice models. We exploit the property that massive Dirac fermions form mid-gap bound states with spin and valley degeneracies in the vicinity of a Coulomb impurity. Due to electronic repulsion, the antiferromagnetic correlations of the impurity lattice are driven

by a super-exchange interaction with SU(4) symmetry, which emerges from the bound states degeneracy at quarter filling. We propose that quantum spin-orbital liquids can be engineered in artificially designed solid-state systems at vastly higher temperatures than achievable in optical lattices with cold atoms. We discuss the experimental setup and possible scenarios for candidate quantum spin-liquids in Coulomb impurity lattices of various geometry.

## 4.2 Background

### 4.2.1 Mott insulator and the Hubbard model

The concept of Mott insulators plays a vital role in the physics of high temperature superconductors and quantum spin liquids. We give a brief review of Mott insulators, and some of the discussions follow [54][55].

Electrons in crystals move in the background of periodic potentials provided by the positive charges from atomic nuclei. For weakly interacting systems, free electron band theory is a good approximation to describe electron behaviors in crystals. For a band insulator, the highest band is separated by a finite energy gap from the lower completely filled valence bands. When strong interactions between electrons are considered, the situation can be quite different. There is a new class of insulator, Mott insulators, appearing. In a Mott insulator, the opening of a band gap is due to the large interaction strength. We begin with a lattice model

$$H = H_0 + H_I, \tag{4.1}$$

$$H_0 = -t \sum_{ij} (c^\dagger_{i\alpha} c_{j\alpha} + \text{h.c.}) - \mu \sum_i n_i, \tag{4.2}$$

$$H_I = \frac{1}{2}\sum_{ij} V_{ij} n_i n_j. \tag{4.3}$$

where $\alpha = \uparrow, \downarrow$ is the spin index, the density operator is $n_i = c_i^\dagger c_i$. The non-interacting Hamiltonian $H_0$ can be used to describe a metal, where there is only one electron on each lattice site (half-filling). In the interaction Hamiltonian, $V_{ij}$ is the interaction strength for a long-ranged Coulomb interaction, $V(|r|) = \frac{e^2}{4\pi}\frac{1}{|r|}$. To model the Mott insulator, the Hubbard model is often used, where a short-ranged interaction is considered. The Hubbard on-site repulsive interaction term is

$$H_U = U\sum_i n_{i\uparrow} n_{i\downarrow}. \tag{4.4}$$

We can see in the $U \to \infty$ limit, the $H_0$ term is ignored and electrons cannot jump to other sites because this would cost a large amount of energy, so the system is insulating due to *interaction*. The model has two parameters $t$ and $U$, and the competition between the hopping constant $t$ and the Hubbard term $U$ determines the behavior of the model. For the intermediate value of $t/U \sim 1$, the analysis of the model is highly non-trivial. For large $U$ and small $t/U$, the hopping terms can be treated as a perturbation, and the Hubbard model can be written in a spin interaction form which is very helpful for looking at the spin physics of the model. In this limit, the model is called $t - J$ model which, in the second order in the hopping constant $t$, can be written as [55]:

$$H_{tJ} = \frac{1}{2}\sum_{ij} J(\vec{S}_i \cdot \vec{S}_j - \frac{n_i n_j}{4}), \tag{4.5}$$

where $J = 4t^2/U$. Hence, in the large $U$ limit and up to the order of $t^2/U$, the Hubbard model is equivalent to an antiferromagnetic Heisenberg model. The job of studying the Hubbard model is mapped to the study of the antiferromagnetic

model: a spin model. There are many questions concerning this spin model. An important one is what is the ground state of this antiferromagnet model? If the spins are actual classical vectors, the ground state of the antiferromagnet consists of two sublattices with opposite spin orientations (ignoring frustration for the moment). This ground state is called Néel state. It seems that quantum effects would prohibit such kind of "static" spin configuration. However, experiments find that $Cu^{2+}$ ions have the Néel antiferromagnetic ground state. [56]

### 4.2.2 Quantum spin liquid

Other states are proposed to be the ground states of the quantum Heisenberg antiferromagnets. The leading aim is to find non-magnetic ground states which break no symmetries, leading to the concept of quantum spin liquids. Philip Anderson proposed [57] the concept of the resonating valence bond state in the triangular lattice, in which geometric frustration may prevent the formation of Néel state. Consider any two spins belonging to two sites, and pair them into a spin singlet state. If every spin is paired with another spin in the system, we have a configuration of these "bond states", but this configuration breaks the space symmetry of the underlying lattice. To restore the symmetry, one needs to have a set of many configurations, which include every symmetry operation counterparts (the summation of different configurations is the process of "resonating"). Because every spin singlet in such configurations has the magnetic quantum number $m = 0$, the system is not magnetic. However, in experiments [58] a spiral Néel state called 120° Néel state is found in frustrated triangular lattices, for example on monolayer Mn on Ag(111) [59]. The 120° Néel state has in-plane spins which are rotated 120° relative to their neighbors in a triangular

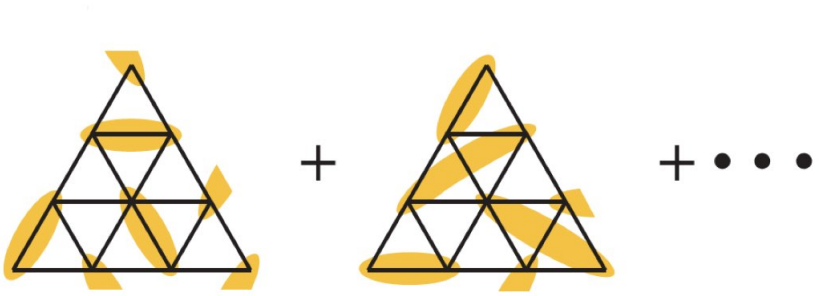

Figure 4.1: An pictorial representation of the resonating valence bond state in the edge-sharing triangular lattice. This figure is from [61].

lattice.

Although in some antiferromagnetic models defined on a triangular lattice the experiments show ground states are not spin liquids, the theory of quantum spin liquids has been developed further, since they may be realized in other systems. The modern understanding of the quantum spin liquid, particularly its connection with topological phases, has become a core research topic in condensed matter theory. The search for generic spin liquids in real materials is progressing rapidly. For a thorough review which emphasizes the theory aspects, see [60]. A short overview on this topic is given in [61].

From the construction of the resonating valence bond state, we can see two important defining properties of quantum spin liquids: a disordered ground state and quantum entanglement. In quantum spin liquids, spins do not arrange themselves in an ordered way like in a ferromagnet. In a ferromagnet, the SU(2) rota-

tional symmetry of spins is broken: a particular orientations of spins is chosen. Order parameters and the Ginzburg-Landau paradigm of describing the dynamics of order parameters are the standard language for broken symmetry phases. The rotational symmetry of spins persist even in the zero temperature limit in quantum spin liquids. (Notice there is a special class of the quantum spin liquid, the chiral spin liquid, which can violate the time reversal symmetry and the inversion symmetry spontaneously [62].)

The entanglement properties of quantum spin liquids are fundamental for understanding these phases in the sense of topological phases. The key point is the connection between the non-local excitation and quantum entanglement. Because subsystems are entangled, one can not define local excitations in one subsystem without the interference from others. Consequently, quantum spin liquids support non-local excitations: an excitation is created by non-local operators. These excitations involve a string of local degrees of freedom, but the interplay among these excitations is still like quasiparticles.

Let us take two examples: one is the toric code from the perspective of topological phases; the other is an antiferromagnet. In the toric code model [63][64], spin 1/2 operators are definded on the bonds of a square lattice (Fig. 4.2), the Hamiltonian is

$$H_T = -J_e \sum_s A_s - J_m \sum_p B_p, \tag{4.6}$$

where $s$ labels all vertices of the lattice and $p$ means plaquette of the square lattice. Two operators are $A_s = \prod_{j \in s} \sigma_j^x$ and $B_p = \prod_{j \in p} \sigma_j^z$. Because $A_s$ and $B_p$ commute (can be proved by calculating the commutator straightforwardly), the ground states are defined by $A_s = B_p = 1$. For the ground state degeneracy, the original article is [63].

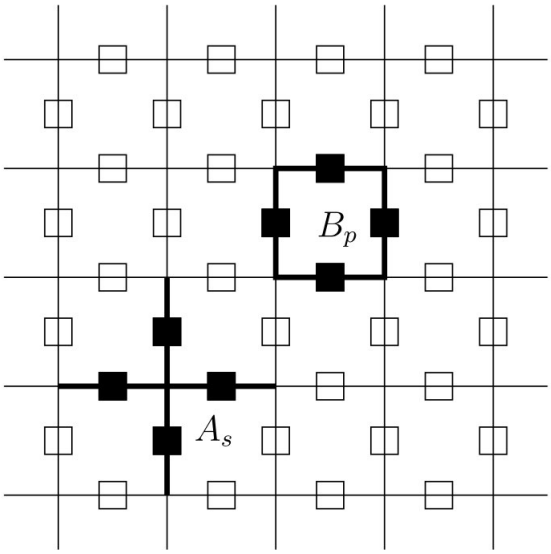


Figure 4.2: Two operators are defined: $A_s$ is defined on the vertices, and $B_p$ is defined on plaquettes. The figure is from [64].

Let us say a little bit about the excitations. There are two kinds of excitations appearing in toric code: the electric charge and the magnetic vortices. The electric particle is defined by

$$W^e(L) = \prod_{j \in L} \sigma_j^z, \tag{4.7}$$

and this is a string of operators defined along a path $L$. Let us consider $L$ is just a single bond, $W^e(L) = \sigma_j^z$. We see two $A_s$ are flipped. For a long string, the two ends are flipped and the energy increased is $2J_e$. The point is that one can not flip a single $A_s$ operator. A similar magnetic particle can be defined: $W^m(L^*) = \prod_{j \in L^*} \sigma_j^x$, where $L^*$ is defined in the dual lattice. The mutual statistics of the electric charges and the magnetic vertices are semion-like, a signature of many-body entanglement [65][66].

Now we turn to the second example, the antiferromagnet. In the Néel state,

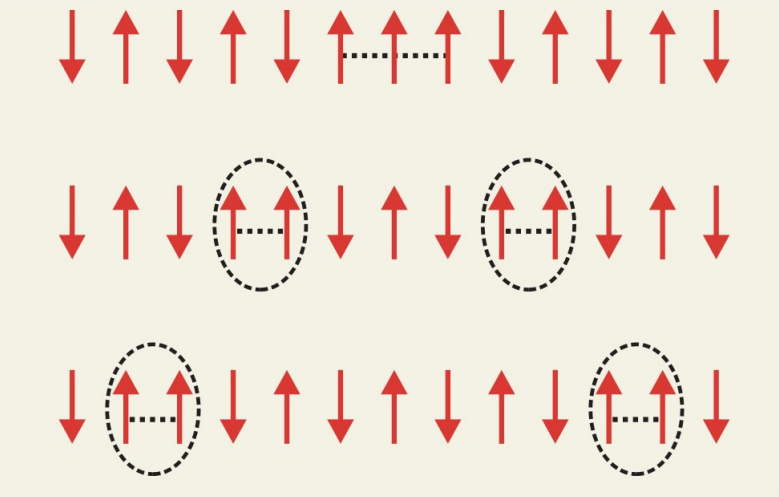

Figure 4.3: Spinon excitations in a 1D antiferromagnet. One spin flip creates domain walls (indicated by ovals), which can move without paying energy costs. The figure is from [61].

flipping one spin would change two bonds, so the energy is increased by $2J$($J$ is the bond energy). These two bonds can be seen as domain wall excitations which can propagate separately, and it costs no energy to move domain walls. The progress of spinon excitation and domain walls movement is shown in Fig. 4.3. These excitations can only be created in pairs and each of them carry spin 1/2, since one spin flip creates two domain walls. Proliferation of spinons in the antiferromagnetic state can lead to quantum frustration, which could stabilize a spin liquid as the ground state. This scenario contrasts with the classical spin case, where spin flips are not allowed, since they cost too much energy. For the later, the low energy excitations are classical Goldstone modes in the form of spin waves.

We comment on some spin liquid models. Based on the Hamiltonian $H = J_{ij} \sum_{ij} \vec{S}_i \cdot \vec{S}_j$, Heisenberg $SU(N)$ antiferromagnet systems on different lat-

tices have been extensively studied, like in square lattices, triangular lattices, and kagomé lattices. In kagomé lattice, $Sp(N)$ symmetric antiferromagnet was investigated by using the large $N$ technique [68][69]. Two ground states are found in two different limits of the control constant $\kappa = \frac{n_b}{N}$, here $n_b$ is the boson density on each lattice site. For large $\kappa$, the ground state is magnetic-ordered. Classical state degeneracy is lifted by quantum fluctuations. This is the so-called order by disorder. For small values of $\kappa$, the ground state is argued to be a quantum spin liquid which is quantum-disordered, and symmetries are not broken.

By using projective symmetry groups proposed by Wen [67], hundreds of symmetric spin liquids have been constructed, but the question one must ask is: how can we find them? There are some experiment measurements which provide evidences of quantum spin liquids. A subset of these experiment methods includes specific heat measurement, neutron scattering, and magnetic susceptibility measurement. The specific heat measurements help elucidate the low energy excitation properties of the system. [70] reports the thermodynamic properties of an organic Mott-insulator $EtMe_3Sb[Pb(dmit)_2]_2$ (dmit represents 1,3-dithiole-2-thione-4,5-dithiolate). A temperature-linear heat capacity is found below $1K$, which provides evidence supporting a gapless spin liquid. One important physical observable quantity is the structure factor, which is defined by the spin-spin correlation function:

$$S(\vec{k}) = \frac{1}{N}\sum_{i,j}\langle S_i \cdot S_j\rangle \mathrm{e}^{i\vec{k}\cdot(\vec{r}_i-\vec{r}_j)} \tag{4.8}$$

This quantity can be used to characterized the ground state of an antiferromagnetic system and provide indirect signatures of a quantum spin liquid state [116]. Inelastic neutron scattering measurements in kagomé antiferromagnet $ZnCu_3(OD)_6Cl_2$ (herbertsmithite) are reported in [71]. They give insights be-

cause the neutron scattering cross section is proportional to the structure factor.

## 4.3 Artificial Mott insulator and spin-orbital liquids realization

Spin-orbital liquids result from systems that have not only spin degeneracies but also orbital degeneracies [139, 73]. Those states are strongly correlated, have non-local excitations, but nevertheless do not break any symmetries. In spite of mounting theoretical effort [74, 75, 76, 77, 78], a significant difficulty in finding viable candidates for quantum spin-orbital liquids is the fact that normally the interactions governing spin and orbital degrees of freedom have very different energy scales [79, 80, 81]. Consequently those degrees of freedom are decoupled at sufficiently low temperatures, hindering the quantum frustration that is required to entangle orbitals and spins. Very recently, x-ray scattering studies in magnetic honeycomb based $BaCuSb_2O_9$ crystals reported indications of spin-orbital entanglement at low temperature [82, 83].

An alternative to identifying crystals where spins and orbitals are strongly coupled would be instead to create artificial crystals where spin and orbital quantum numbers become interchangeable. Such a property appears in magnetic Hamiltonians that display SU(4) symmetry [150]. Recent experiments with cold atoms reported spectroscopic quantum simulations in small artificial magnetic systems with SU($N \leq 10$) symmetry at ultra low temperature [85, 86]. Mott physics with SU(2) spins has been observed in optical lattices with ultracold atoms inside a parabolic potential [87]. In those systems, strong correlations emerge only at extremely low temperatures, making a possible detection of

quantum spin-liquids challenging [88]. Solid-state systems where antiferromagnetic interactions have SU(4) symmetry are not common, since in real materials, anisotropies and off-diagonal hopping matrix elements in the degenerate orbital space usually lower that symmetry [89].

We propose a solid-state system that can be experimentally designed with scanning tunneling microscopy (STM) tips by positioning Coulomb impurity adatoms in a periodic array on top of an insulating honeycomb substrate. The electrons in those substrates can be described by massive Dirac fermions, which form bound states around the impurities [90, 91, 92]. Those bound states have spin and valley degeneracies, which are dual to spin-orbital degrees of freedom. We theoretically construct an artificial lattice where each impurity site is quarter filled with valley and spin polarized states. The problem has an emergent SU(4) symmetry that follows from the orthogonality between the two different valley spaces. In systems like graphene, SU(4) symmetry is known to emerge in the quantum Hall regime [93]. Electronic interactions lead to a variety of broken symmetry states in both spins and valleys [94, 95, 96, 138, 98, 99].

The spin-orbital exchange interactions are calculated in three different impurity lattice geometries: triangular, square and honeycomb, shown in Fig. 1. We find the constraints on the impurity lattice in the regimes where the system is expected to behave as a Mott insulator dominated by antiferromagnetic interactions between sites. We propose the experimental conditions for the observation of those states. For honeycomb substrates such as graphene grown on SiC [100, 101], we show that the Mott regime of entangled spins and orbitals is experimentally accessible and that the superexchange interaction can be as large as $J_s/k \sim 60 - 120$ K. The experimental signatures of strongly correlated states are discussed based on possible scenarios predicted for SU(4) spin-orbital models

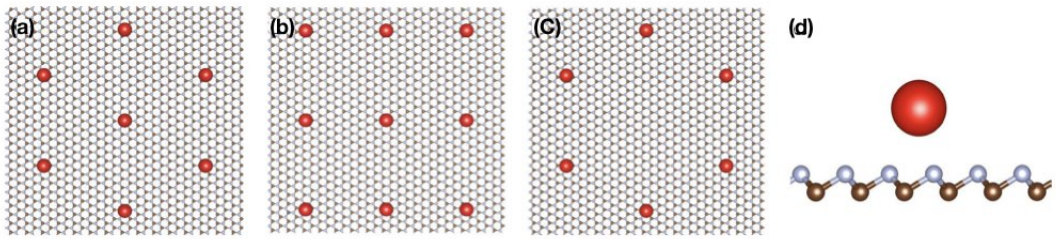


Figure 4.4: Honeycomb substrate with unequal sublattices decorated with a superlattice of charged impurities. In the three configurations, triangular (a), square (b) and honeycomb (c), the impurities are separated by a superlattice constant $L$, and sit at a distance $d$ away from the plane of the substrate (d). All impurities interact with electrons via Coulomb, $1/r$ potential.

[102, 103, 104, 105], including quantum spin-orbital liquids.

## 4.4 Coulomb impurity problem

The wavefunction of the Coulomb impurity bound states for 2D massive Dirac fermions, $\Psi(\mathbf{r})$, can be derived from the Dirac equation

$$(-i\hbar v\boldsymbol{\sigma}\cdot\boldsymbol{\nabla}+V(r)+mv^2\sigma_z)\Psi(\mathbf{r})=\epsilon\Psi(\mathbf{r}). \tag{4.9}$$

$\boldsymbol{\sigma}=(\sigma_x,\sigma_y)$ is a vector with off-diagonal Pauli matrices, $\sigma_z$ is the diagonal Pauli matrix, $v$ is the Fermi velocity and $m$ is the mass term of the substrate, that describes a gap in the electronic spectrum, $\Delta=2mv^2$. $V(r)=-Ze^2/\kappa\sqrt{r^2+d^2}$ is the Coulomb impurity potential, where $Z$ is the number of charges of the impurity, $e$ is the electron charge, $\kappa$ the dielectric constant of the surface, and $d\approx 2-3$Å is the out-of-plane distance between the impurity and the plane of the substrate.

The impurity potential decays as $V(r)\sim 1/r$ in the $r\gg d$ limit and saturates

into a constant in the opposite limit. The potential can be written as

$$V(r) = -Z\frac{e^2}{\kappa}\left[\frac{1}{r}\theta(r-a) + \frac{1}{a}\theta(a-r)\right] \tag{4.10}$$

where $a$ is an effective real space cut-off which regularizes the Coulomb potential. The size of the cut-off can be chosen as $a \sim d$ and is typically of the order of the impurity size. This regularization procedure is well known in quantum electrodynamics in 3+1 dimensions ($\mathrm{QED}_{3+1}$) and has been successfully used to explain the experimentally observed dive of bound states in the lower continuum around super-heavy nuclei with atomic number $Z > 137$ [106, 107]. Both in $\mathrm{QED}_{3+1}$ as in the 2D case, the wavefunction of the Coulomb impurity bound states decay over a characteristic distance defined by the Compton wavelength $\lambda_C = \hbar/mv$.

In cylindrical coordinates, the solution of Eq. (4.9) is in the form

$$\Psi(r,\phi) = \frac{c}{\sqrt{2\pi}}\begin{pmatrix} F_j^{(-)}(r)\mathrm{e}^{i(j-\frac{1}{2})\phi} \\ iF_j^{(+)}(r)e^{i(j+\frac{1}{2})\phi} \end{pmatrix}, \tag{4.11}$$

where $j = \pm\frac{1}{2}, \pm\frac{3}{2} \ldots, m+\frac{1}{2}$ ($m \in \mathbb{Z}$) are the possible angular momentum states, and $c$ is the normalization constant. The energy spectrum is quantized by the usual quantum numbers in the Hydrogen atom problem, $n \in \mathbb{N}$ and $j$ [90, 91, 92]. The degeneracy of the $\pm|j|$ angular momenta states for a given $n > 0$ however is lifted. At $n = 0$, only the $j = \frac{1}{2}$ state is allowed. For more details of this solution, please read the appendix.

Defining the impurity strength by the dimensionless coupling $g \equiv Z\alpha$, where $\alpha = e^2/\kappa\hbar v$ is the screened fine structure constant of the substrate, there are two known regimes of the problem: the perturbative regime $g \ll 1$, where the bound

states are shallow, and the strong coupling regime $g \gtrsim 0.5$, where they dive in the negative sector of the energy spectrum, as shown in Fig. 4.5 a. At fixed $g$, the lowest energy level is the $n = 0$, $j = \frac{1}{2}$ state, followed by the first excited state $n = 1$, $j = -\frac{1}{2}$. There is an infinite number of higher excited states inside the gap $\Delta$. The latter states have very small binding energies and are not relevant to this discussion.

We are interested in the strong coupling regime of the problem ($g \gtrsim 0.5$), where the confining potential is deep and the energy separation between the ground state level and the first excited state is of the order of $\sim \Delta/2$. At sufficiently large coupling, $g > g_c$, the lowest energy state level dives in the continuum of negative energy states outside of the gap. This regime is known as the supercritical regime. At the critical one, when $g = g_c$ the energy of the lowest level is exactly at the edge of the gap, $\epsilon = -mv^2$. In the subcritical regime, $0.5 \lesssim g < g_c$, which is the focus of this paper, the levels are strongly localized and sharply defined inside the gap. For a Coulomb impurity on top of graphene epitaxially grown on SiC, where $\Delta \sim 0.26$ eV [100], and for a typical small distance cut-off $a \approx 2.8$Å, $g_c = 0.916$. In general, the critical coupling $g_c \sim 1$. The energy of the levels follows directly from matching the wave function at $r = a$, similarly to the procedure in the QED$_{3+1}$ case. The solution of the subcritical regime can be calculated either numerically [90] or for the purposes of this work, analytically, as detailed in the appendix.

### 4.4.1 Impurity lattice model.

In a honeycomb lattice with massive Dirac fermions, the quasiparticles also have two valley flavors, in addition to the spin. The Coulomb impurity bound states

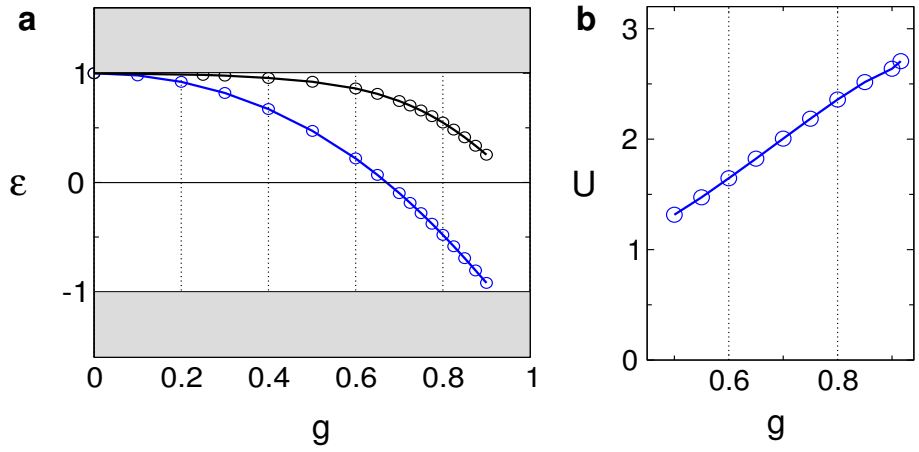


Figure 4.5: (a) Energy of the Coulomb impurity bound states $\epsilon$, in units of $mv^2 = 0.13$ eV, as a function of the dimensionless coupling $g = Z\alpha$. Blue dots: ground state level, $n = 0$, $j = \frac{1}{2}$. Black dots: first excited state, $n = 1$, $j = -\frac{1}{2}$. At $g = g_c \approx 0.916$, the lowest energy level dives in the continuum of negative energy states at $\epsilon = -mv^2$. In the subcritical regime $g \lesssim g_c$, the two levels have an energy separation $\sim mv^2$. (b) Hubbard $U$, in units of $mv^2\alpha$, versus $g$ in the strong coupling regime $0.5 \leq g \leq g_c$. $U$ is comparable to the energy of the gap $\Delta = 2mv^2$.

therefore must have both spin and valley degrees of freedom. The Dirac equation in this case is

$$\begin{pmatrix} \hat{\mathcal{H}}_+(\mathbf{r}) & 0 \\ 0 & \hat{\mathcal{H}}_-(\mathbf{r}) \end{pmatrix} \Phi(\mathbf{r}) = \epsilon\Phi(\mathbf{r}), \tag{4.12}$$

where $\hat{\mathcal{H}}_+(\mathbf{r}) = -i\hbar v\boldsymbol{\sigma}\cdot\boldsymbol{\nabla} + V(r) + mv^2\sigma_z$ is the Dirac Hamiltonian matrix in valley + and $\hat{\mathcal{H}}_-(\mathbf{r}) = \hat{\mathcal{H}}_+^*(\mathbf{r})$ in the opposite valley. The eigenvectors are the four component spinors $\Phi_{j,+}(\mathbf{r}) = (\Psi_j(\mathbf{r}), \mathbf{0})$ and $\Phi_{j,-}(\mathbf{r}) = (\mathbf{0}, \Psi_j^*(\mathbf{r}))$, which are degenerate. The $j$-th energy level is four-fold degenerate, with two spins and two valleys. The valleys describe the orbital motion of an electron around a Coulomb impurity. They effectively behave as a pseudo-spin with SU(2) symmetry, as the actual spins.

Once Coulomb interactions among the electrons in the bound state are included, those states tend to spin and valley polarize due to correlations and Pauli

blocking. In the ground state, $j = \frac{1}{2}$, the Coulomb interaction can be expressed in terms of a Hubbard $U$ term

$$\mathcal{H}_U = \frac{1}{2} U \sum_{\{\nu\},\{\sigma\}} \hat{n}_{\nu,\sigma} \hat{n}_{\nu',\sigma'} (1 - \delta_{\nu,\nu'} \delta_{\sigma\sigma'}), \tag{4.13}$$

where

$$U = \int \mathrm{d}^2 r \mathrm{d}^2 r' |\Phi_{\frac{1}{2},\nu}(\mathbf{r})|^2 \frac{e^2}{\kappa |\mathbf{r} - \mathbf{r}'|} |\Phi_{\frac{1}{2},\nu'}(\mathbf{r}')|^2 \tag{4.14}$$

is a valley independent local repulsion. $\hat{n}_{\nu,\sigma} = c^\dagger_{\nu,\sigma} c_{\nu\sigma}$ is the number operator per valley and spin at the bound state, where $c_{\nu,\sigma}$ annihilates one electron in the $j = \frac{1}{2}$ level on valley $\nu$ with spin $\sigma$. Due to the orthogonality of the eigenspinors, $\Phi^\dagger_{j,+}(\mathbf{r}) \Phi_{j,-}(\mathbf{r}) = 0$, the exchange interaction between electrons in different valleys around the same Coulomb impurity is zero.

In Fig. 4.5 b, we calculate $U$ as a function of the dimensionless impurity coupling $g$ in the strong coupling regime $0.5 \lesssim g < g_c$. At $g = g_c$, $U = 2.7\, mv^2\alpha$, dropping to $U = 1.35\, mv^2\alpha$ at $g = 0.5$. When $U$ is large and only the $j = \frac{1}{2}$ level is filled, the ground state will be singly occupied in one of the four possible states: $|\bullet\rangle = |+,\uparrow\rangle$, $|\bullet\rangle = |+,\downarrow\rangle$, $|\bullet\rangle = |-,\uparrow\rangle$, and $|\bullet\rangle = |-,\downarrow\rangle$.

We would like to write down an effective lattice model for a strongly correlated lattice of Coulomb impurities, each one having a quarter filled bound state in one of the four possible states above. Those electrons can hop between different Coulomb impurity sites, with each one having a Hubbard $U$ energy, that penalizes multiply occupied sites, and also having a well defined valley and spin. The hopping term is

$$\mathcal{H}_t = -t \sum_{\langle ij \rangle} \sum_{\nu,\sigma} c^\dagger_{i,\nu,\sigma} c_{j,\nu,\sigma}, \tag{4.15}$$

with $c_i$ describing the annihilation operator of an electron in the $j = \frac{1}{2}$ level

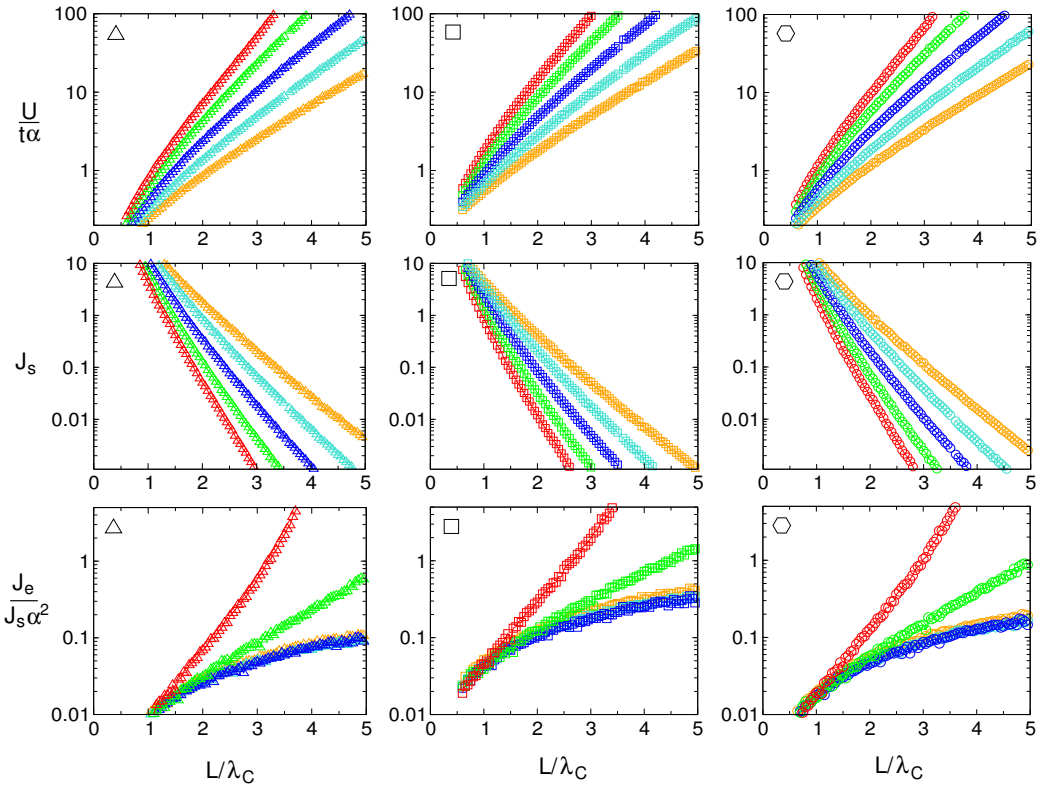


Figure 4.6: Left column : triangular lattice; middle column square lattice; right column : honeycomb lattice. Red dots: $g = 0.9$; green: $g = 0.8$; blue: $g = 0.7$; cyan: $g = 0.6$; orange: $g = 0.5$. Top row: ratio between the onsite repulsion ($U$) and the kinetic energy ($t$) times the fine structure $\alpha$ versus the superlattice constant $L$ normalized by the Compton wavelength $\lambda_C = \hbar/mv$. For a substrate with a gap of of $\Delta = 0.26$ eV (graphene on SiC), $\lambda_C \approx 46$Å. When $U/t \sim 5$, the system is strongly correlated: the Coulomb impurities form a lattice of local spin-orbitals. Middle row: Superexchange interaction, $J_s = t^2/U$ in units of $mv^2/\alpha$, versus $L/\lambda_C$. Bottom row: ratio between the exchange interaction $J_e$ and the superexchange interaction $J_s$ times $\alpha^2$.

siting on an impurity site located at $\mathbf{R}_i$, and $\langle ij \rangle$ denotes summation over nearest neighbor (NN) sites. The hopping parameter of the Coulomb impurity lattice is

$$t_{ij} = \int \mathrm{d}^2 r \Phi^{\dagger}_{\frac{1}{2},\nu}(\mathbf{r}_i) \sum_{k \neq i} V(|\mathbf{r}_k|) \Phi_{\frac{1}{2},\nu}(\mathbf{r}_j) \tag{4.16}$$

where $\mathbf{r}_i \equiv \mathbf{r} - \mathbf{R}_i$ is the position relative to site $i$. Hopping between Coulomb impurity sites conserves valley due to the orthogonality of eigenspinors in the valley space, $\Phi^{\dagger}_{\frac{1}{2},+}(\mathbf{r}_i)\Phi_{\frac{1}{2},-}(\mathbf{r}_j) = 0$. Because of the summation of the potential over lattice sites and the long range nature of the Coulomb interaction, the value of $t$ is influenced by the geometry of the lattice.

In the limit $U \gg t$, we can expand the effective Hamiltonian in second order perturbation theory in the hopping, $\mathcal{H}_s = -\mathcal{H}_t \mathcal{H}_U^{-1} \mathcal{H}_t + \mathcal{O}(t^4)$. The Hamiltonian that results is the superexchange interaction, which favors antiferromagnetic alignment of spins or valleys. This interaction is of order $J_s = t^2/U$ and lowers the energy cost for electrons to hop back and forth between two NN sites. The superexchange competes with the exchange interaction between NN sites, which is ferromagnetic and defined by

$$J_{e,ij} = -\frac{1}{2} \int \mathrm{d}^2 r \mathrm{d}^2 r' \, \Phi^{\dagger}_{\frac{1}{2},\nu}(\mathbf{r}_i)\Phi_{\frac{1}{2},\nu}(\mathbf{r}_j) \frac{e^2}{\kappa|\mathbf{r} - \mathbf{r}'|} \Phi^{\dagger}_{\frac{1}{2},\nu'}(\mathbf{r}'_j)\Phi_{\frac{1}{2},\nu'}(\mathbf{r}'_i), \tag{4.17}$$

with $J_{e,\langle ij \rangle} \equiv J_e < 0$. As shown in Appendix A, both the superexchange and the exchange interactions map into a Kugel-Khomskii type Hamiltonian [108] with exact SU(4) symmetry,

$$\mathcal{H} = J \sum_{\langle ij \rangle} \left( \frac{1}{2} + 2\boldsymbol{\tau}_i \cdot \boldsymbol{\tau}_j \right) \left( \frac{1}{2} + 2\mathbf{S}_i \cdot \mathbf{S}_j \right), \tag{4.18}$$

where $\boldsymbol{\tau}_i$ is the valley pseudospin operator and $\mathbf{S}_i$ the spin operator on a given

site. Hamiltonian (4.18) is symmetric under any permutation among the four different valley-spin flavors (colors).

The coupling $J \sim J_s > 0$ in the regime where the superexchange coupling dominates ($t^2/U \gg J_e$). The superexchange interaction is antiferromagnetic, and can drive the spin-orbital lattice into frustrated phases where no symmetry is broken. In the opposite regime ($J_e \gg t^2/U$), the coupling $J = -J_e < 0$ changes sign, and the system tends to order in a ferromagnetic state at zero temperature.

### 4.4.2 Numerical results.

In Fig. 4.6 we show the ratio of $U/t\alpha$ as a function of the impurity lattice constant $L$ for three different geometries: triangular, square, and honeycomb. $L$ is normalized by the Compton wavelength $\lambda_C$, which is inversely proportional to the mass gap of the substrate. In the regime where $U/t \gtrsim 5$, the system is a strongly correlated insulator and can be effectively described as a lattice of local valley-orbitals and spins. The different curves in each panel correspond to different impurity couplings, with $g$ ranging from 0.5 to the critical value $g_c \sim 0.916$. At the middle row panels, we display the superexchange coupling $J_s$ (in units of $mv^2/\alpha$) as a function of $L$. For couplings $g < g_c$, when $U/t\alpha \sim 12$ the superexchange coupling ranges from $J_s\alpha/mv^2 \approx 0.01 - 0.02$ for $g$ running between 0.5 and 0.9 in all geometries we tested, as indicated in Fig. 4.6. In the regime $U/t\alpha \sim 20$, the super exchange is in the range $J_s\alpha/mv^2 \approx 0.003 - 0.007$.

For graphene on SiC substrate with $\Delta = 2mv^2 \sim 0.26$ eV, the Compton wavelength $\lambda_C \approx 46$Å. On the surface of SiC ($\kappa \sim 5.2$) the fine structure constant $\alpha \approx 0.42$. The size of the superlattice constant $L$ that corresponds to a fixed value of $J_s$ varies slightly depending on the geometry of the lattice. At $g \approx g_c$ (red dots),

the impurity valence $Z \sim 2$. When $U/t\alpha = 12$ ($U/t \approx 5$), the superexchange interaction between NN sites is $J_s/k \sim 59$ K and corresponds to impurity lattice constants $L/\lambda_C \approx 2.25\,(\triangle)$, 1.9 , and 2.1 , resulting in $L \sim 90 - 100$Å. At $g = 0.5$ or $Z \sim 1$ (orange dots), the wavefunctions are more weakly bounded to the impurities and hence more extended. The same ratio of $U/t \approx 5$ corresponds to $J_s/k \sim 28$ K and larger superlattice constants $L/\lambda_C \sim 4.6\,, 3.9\,,$and $4.3\,,$ respectively, with $L \sim 180$Å $- 200$Å. For a larger gap of $\Delta \sim 0.5$ eV [101], the superexchange nearly doubles ($J_s \sim 56 - 118$ K) while the Compton wavelength is halved. When $U/t\alpha = 20$ ($U/t \approx 8.5$), $J_s/k \sim 10 - 20$ K.

In the regime of interest, where $U/t$ is large, $U$ is the largest energy scale in the problem. The superexchange interaction competes with the exchange one $J_e$ and, in principle, both can be of the same order. In the bottom row of the panels in Fig. 4.6 we plot the ratio between $J_e/J_s\alpha^2$. For $\alpha < 1$, the superexchange interaction clearly dominates the exchange interaction, and is at least three times larger for $U/t\alpha \lesssim 20$. When considering Coulomb impurities on graphene-SiC substrates, where $\alpha = 0.42$, the ratio $J_e/J_s < 0.07$ in all geometries considered in the range $U/t \lesssim 8.5$. The dominant interactions are therefore clearly antiferromagnetic. Due to the SU(4) symmetry, valley and spin degrees of freedom are strongly entangled and may give rise to a spin-orbital liquid in the Mott insulator regime.

### 4.4.3 Experimental setup.

The lattice of Coulomb impurities can be experimentally created with STM tips, which can drag atoms on a surface with atomic precision [109]. Possible substrates include graphene epitaxially grown on SiC, which was shown to develop a gap ranging from $\Delta = 0.26 - 0.5$ eV [100, 101]. In high quality samples, the Fermi

level was observed in the middle of the gap [101]. Other crystals, such as $MoS_2$, $MoSe_2$, and other dichalcogenides [110], have even larger gaps, however they also exhibit large spin-orbit couplings [111], which will lift the SU(4) symmetry of the problem, lowering it to SU(2). Strong unitary disorder connects the two valleys and can also have a similar effect. Disorder effects, however, can be inhibited by properly annealing the substrate.

Among alkaline metals, potassium adatoms ($Z = 1$) are known to spontaneously form two dimensional crystals on honeycomb substrates such as graphite [112]. Higher valence cobalt adatoms have already been studied with STM on graphene and are also possible candidates [113]. The strong coupling regime, where the bound states are deep and well separated, is experimentally accessible for impurities with a valence $Z \sim 1$. That contrasts with the standard relativistic scenario, where the strong coupling regime can be achieved only when the valence is of the order of the inverse of the QED fine structure constant $Z \sim 1/\alpha_{QED} = 137$.

The determination of the impurity lattice constant $L$ that is required to create a Mott insulator with strong antiferromagnetic correlations can be achieved with local spectroscopy measurements around a single impurity. Those measurements can accurately determine the energy of the bound states inside the gap. With the theoretical wavefunctions, one can extract the effective impurity coupling $g$ by comparing the measurement of the energy levels with the calculated result, as shown in Fig. 4.4. The appropriate range for the impurity lattice constant is indicated in the plots of Fig. 4.6. Integration of the measured local density of states over the area around the impurity gives the occupation of the ground energy level inside the gap. When the impurity lattice is in the Mott regime, each four-fold degenerate impurity level will remain singly occupied (quarter filling).

## 4.5 Discussion

Recent numerical evidence [102] suggests that the ground state of the antiferromagnetic Hamiltonian (4.18) in the honeycomb lattice is a strongly correlated state that preserves all the symmetries of the system. This state is a quantum spin-orbital liquid schematically drawn in the left panel of Fig. 4.7. Every site has a well defined spin-valley state (color) among the four possible colors. Each color has the same neighbors up to color permutations. The pattern preserves both the lattice symmetry and the SU(4) color symmetry.

Color-color correlations appear to decay as a power law, indicating a gapless state, or equivalently, an algebraic quantum spin-orbital liquid with no true long range order. Algebraic spin liquids are generally known to be robust two-dimensional interacting critical states, relevant to a variety of correlated physical models [114]. After comparison of the energy of several different states, the quarter filled $\pi$-flux state currently appears as the leading candidate [102]. In the honeycomb lattice, a $\pi$-flux in the honeycomb plaquette creates Dirac fermions at quarter filling, which is the regime of interest for Mott insulators with SU(4) symmetry. Those Dirac fermions are spinon excitations, which are four-fold degenerate due to the color symmetry.

Low-energy characteristic probes amenable to 2D systems have been proposed, such as injecting a spin current into the insulator and monitoring the spin bias dependence of the current [116, 117]. In the simplest experimental setup with a single metal-insulator interface, spin accumulation is achieved via the spin Hall effect. In the four-terminal setup, the spin-liquid insulator is coupled to left and right metal leads. Spin current detection occurs through the reverse spin Hall effect in one of the metallic contacts.

In the spin-orbital (valley) case at hand, the spin degrees of freedom in the insulator and in the metal are coupled at the interface. The valleys are decoupled from the orbital degrees of freedom in the metal. Hence the valleys do not experience flips due to the spin current injection. The result is the propagation of a pure spin current with additional valley degeneracy. Consequently, in this case, the spin current will scale in the same way with the bias voltage as in pure spin models. For the $\pi$-flux state, the Dirac cone of the spinons is degenerate in all quantum numbers (spin and valley). The spin current scales with the fifth power of the bias voltage, $I_s \sim V^5$ [116, 117]. This result appears to be a universal signature of both spin and spin-orbital liquid phases with gapless Dirac fermion spinons. In general, the power of the spin voltage dependence is sensitive to the nature and dispersion of the spinon excitations. The exact nature of the spin-orbital liquid state in the honeycomb lattice requires further investigation. Nevertheless, the prospects of observing a true quantum spin-orbital liquid in this geometry seem quite promising.

Triangular lattices are natural candidates for quantum disordered states due to their strongly frustrated nature. It was proposed at first that their ground state has plaquette order [150], with plaquettes formed by SU(4) singlets. However more recent work [103] found strong local resonances between plaquette configurations. While more complicated orders with large unit cells can not be ruled out, the ground state appears to be a spin-orbital liquid with no plaquette order. The presence of next-nearest neighbor superexchange $J_s'$ drives the system into magnetically long range ordered state via a quantum phase transition at a critical value $J_s'/J_s \approx 0.12$ [103]. In the proposed Coulomb impurity lattice, we find that ratio to be $\sim 10^{-2}$. On the basis of the existing knowledge about the model, we conclude that a spin-orbital liquid state can be realized in the Mott

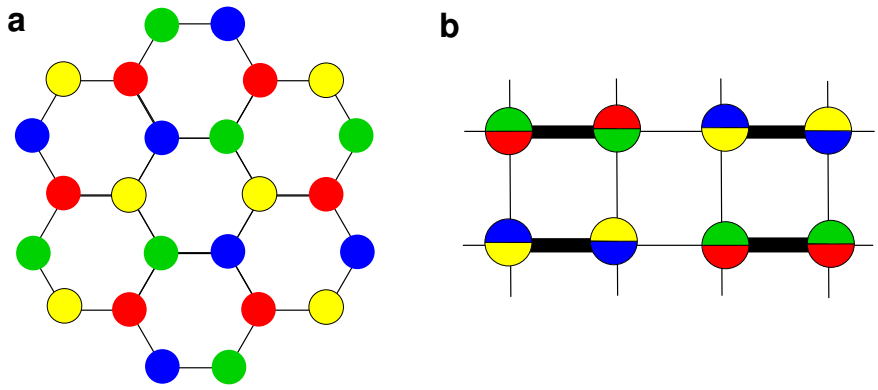


Figure 4.7: (a) Possible algebraic quantum spin-orbital liquid for the honeycomb lattice in the SU(4) Heisenberg model, numerically predicted in Ref. [102]. This state may correspond to a quarter filled $\pi$-flux phase. Each color is surrounded by the same states, up to color permutations. Both crystalline and SU(4) symmetries are intact. (b) Possible dimerized state in the square lattice, with alternating singlets of two colors (after Ref. [104].) This state has long range order and breaks both lattice and color symmetry.

regime. The nature of this state is not yet known.

There have been suggestions of a variety of different ground states for Hamiltonian (4.18) in the square lattice. Possibilities include a gapless spin liquid with nodal fermions [105], and a plaquette state [150, 118]. A more recent numerical work has laid more concrete evidence towards a dimerized state depicted in Fig. 4.7 b, which breaks both lattice and color symmetry [104]. The thick bonds represent strong bonds, while the thick lines are weaker. This particular state has two sets of dimers with two colors each, which alternate along the two main directions of the lattice. Because of the broken symmetry, the elementary excitations are Goldstone modes in the form of gapless magnons. These could also lead to characteristic power law dependencies in the spin current as a function of spin bias [116, 117], with the power being generally smaller than for gapless Dirac spinons ($\pi$-flux phase).

Coulomb impurity lattices offer wide possibilities for different frustrated sce-

narios due to the inherent flexibility in their design. Recent experiments observed evidence for a spin-liquid ground state in the antiferromagnetic Kagome lattice [145]. We conjecture that gapped honeycomb substrates with large spin orbit coupling, such as $MoS_2$ [111], could be experimentally used to design frustrated artificial Coulomb impurity lattices where the spin degeneracy is explicitly lifted, leaving a pure quantum orbital (valley) liquid in the ground state. The tendency towards frustration is not the unique scenario for artificial lattices supported on gapped honeycomb substrates. For instance, color ferromagnetism is possible in superlattices of mass defects forming quantum rings [120].

In summary, we have shown that Mott insulators having spin and orbital degeneracies can be artificially designed in a solid state system. The emergent SU(4) symmetry of the problem follows from the unique nature of the valley degrees of freedom in honeycomb substrates and does not require fine tuning. We have predicted the conditions for Coulomb impurity lattices to be in the Mott regime and discussed experiments that could detect quantum spin-orbital liquid states.

Most of the current efforts to simulate quantum spin liquids are concentrated in cold atom systems, where the Mott physics is present only at ultra low temperatures [87, 88]. This proposal may lead to significant advances in the experimental design and observation of quantum spin-orbital liquids in solid-state settings.

# Chapter 5

# Chiral Topological Superconductivity in $CrO_2$ bilayers

## 5.1 Overview

A chiral superconductor is defined as a superconductor the phase of whose order parameter $\Delta(\vec{p})$ changes as $\vec{p}$ rotates around some axis in the momentum space. The simplest case in this class of superconductor has an order parameter which has the form $p_x + ip_y$. In this chapter, we address the emergence of spin triplet $p+ip$ superconductivity in $CrO_2$ bilayers. $CrO_2$ is a half-metal, which have fully spin polarized conduction bands. Starting from a lattice model, we show that at large doping the system has a sequence of topological phase transitions that can be tuned by gating effects and interaction strength. Among several phases, we find chiral topological phases having a single Majorana mode at the edge. We show that different superconducting topological phases could spontaneously

emerge in the vicinity of the van Hove singularities of the band.

By definition, half metals have only one species of spin, either spin up or spin down, near Fermi energy. In contrast, in normal metals like aluminum, both spin up and spin down electrons are present at the Fermi level. This striking spin polarization in half metals has inspired lots of research activities in spintronics device implementations [124][125]. Half-metals such as $CrO_2$ [129, 130] are promising materials for the prospect of emergent topological superconductivity. By having a metallic Fermi surface with a single spin, they raise the possibility of chiral superconductivity in the triplet channel [131], which is believed to occur only in a handful of systems such as $Sr_2RuO_4$ [134], which may have a spinful triplet state, $UPt_3$ and some heavy fermions superconductors [132, 133]. A distintictive property of chiral topological superconductivity is the presence of Majorana fermions propagating at the edges [135, 136, 137, 139, 138, 140] and half-flux quantum vortices [143, 144] that can trap Majorana modes [141, 142]. Majorana edge states were predicted to exist in different heterostructures with strong spin-orbit coupling [145, 146, 147, 148, 149, 150] and may have been recently observed in an anomalous Hall insulator-superconductor structure [151, 152].

## 5.2 Background knowledge

### 5.2.1 A brief review on Chiral $p_x + ip_y$ superconductors

In this section, we give a brief review of the spinless chiral $p$-wave superconductor. We mainly review the basic formalism of a simple $p+ip$ model, the appearance of Majorana states along the sample edge or inside the vortex. The author learned the subject from the article [135], and the presentation follows the paper closely.

We begin with the spinless Hamiltonian of a two dimensional superconductor in the mean field level,

$$H = \sum_k [(\epsilon_k - \mu) c_k^\dagger c_k + \frac{1}{2}(\Delta_k c_k^\dagger c_{-k}^\dagger + \text{h.c.})], \tag{5.1}$$

where the concrete form of the spectrum of the free particle part $\epsilon_k$ is not important, and in the mean field level we consider the order parameter has the form

$$\Delta_k = |\Delta|(k_x - ik_y). \tag{5.2}$$

The excitations of the system are obtained by the Bogoliubov transformation

$$\eta_k = u_k c_k - v_k c_{-k}^\dagger$$
$$\eta_k^\dagger = u_k^* c_k^\dagger - v_k^* c_{-k},$$

which yields

$$H = \sum_k E_k \eta_k^\dagger \eta_k + \text{const.} \tag{5.3}$$

To determine the edge state, we can put the system on a strip geometry in real space. Along the $y$ direction, the system is extended and the momentum $k_y$ can be used to label different states. We set a domain wall at $x = 0$, where the chemical potential changes sign when going across the line $x = 0$. With this setup, the existence of the edge state can be obtained by solving the BdG equations in real space:

$$i\frac{\partial u}{\partial t} = -\mu u + i\Delta^*(\frac{\partial}{\partial x} + i\frac{\partial}{\partial y})v,$$
$$i\frac{\partial v}{\partial t} = \mu u + i\Delta(\frac{\partial}{\partial x} - i\frac{\partial}{\partial y})u.$$

The equations admit a solution with $u(\mathbf{x},t) = v(\mathbf{x},t)^*$. This solution means we have the condition $\eta^\dagger(\mathbf{x},t) = \eta(\mathbf{x},t)$ or $\eta_k^\dagger = \eta_{-k}$ in momentum space. This condition is the Majorana condition telling us that the quasiparticles are Majorana states whose antiparticles are themselves. For a given $k_y$ and at energy $E$, the BdG equations become

$$Eu = -\mu u + i\Delta(\frac{\partial}{\partial x} - k_y)v,$$
$$Ev = \mu v + i\Delta(\frac{\partial}{\partial x} + k_y)u.$$

If we assume the chemical potential is constant away from the domain wall, we have the equation for $u$ (similar for $v$)

$$\frac{\partial^2 u}{\partial x^2} + \left(\frac{E^2 - \mu^2}{\Delta^2} - k_y^2\right) u = 0. \tag{5.4}$$

So the the equation has solutions which have exponential decay inside the bulk of the system. For $E = 0$, the solution is

$$u \propto \mathrm{e}^{-i\pi/4} \exp\left[-\frac{1}{\Delta}\int_0^x \mu(x)\mathrm{d}x\right]. \tag{5.5}$$

If the superconductor order parameter vanishes at some points in real space, the definition of the phase of the order parameter is problematic at these points. Inside the core of a vortex, the material is in the normal state. The size of a typical core is about the coherence length of the superconductor. These "bad" points are described by the vortices due to the penetration of a magnetic flux. Furthermore, after going around the vortex the phase field of the order parameter would pick up a $2\pi$ phase, which ensures the single-valued property. Because of

the vanishing of the superconducting order parameter, the vortex core is similar to a domain wall as that discussed above, but in this different geometry [135]. The existence of the Majorana mode related to a vortex can be obtained in a similar way.

Another important property about the vortices in $p + ip$ superconductor is that it has a half quantum flux in a spin triplet superconductor when a magnetic field penetrates. A general form of the spin triplet order parameter is

$$\Delta = \Delta_0(\vec{d} \cdot \vec{\sigma})(i\sigma_y)\mathrm{e}^{i\phi} \tag{5.6}$$

where $\vec{d}$ characterizes different components of the order parameter. This order parameter has several components. When the vector $\vec{d}$ changes to $-\vec{d}$ and the phase factor $\phi$ changes by $\pi$, the order parameter will go back to itself and in this case the vortex is a half quantum vortex number. In a spin triplet p-wave superconductor, the spin up pairing channel can be seen as a superconductor with half-quantum vortices, while vortices are absent in the spin down channel. The following Cooper pair wave function captures this

$$\begin{aligned}\Psi(r,\theta) &= \Delta(r)[\mathrm{e}^{i\theta}|\uparrow\uparrow\rangle + |\downarrow\downarrow\rangle](p_x + ip_y) \\ &= \Delta(r)\begin{pmatrix} \mathrm{e}^{i\theta} & 0 \\ 0 & 1 \end{pmatrix}(p_x + ip_y).\end{aligned}$$

Inside the vortex core, a Majorana zero mode may appear. The Bogoliubov quasiparticles satisfy $\gamma^\dagger(E) = \gamma(-E)$, so the zero modes are Majorana modes

which are $\gamma^\dagger(0) = \gamma(0)$. These Majorana modes obey the interchanging statistics

$$\gamma_i \to \gamma_{i+1} \tag{5.7}$$

$$\gamma_{i+1} \to -\gamma_i \tag{5.8}$$

$$\gamma_j \to \gamma_j \quad \text{for non-neighboring sites} \tag{5.9}$$

A well-known candidate material is $Sr_2RuO_4$, which is believed to have p-wave spin triplet superconducting phase. The article [144] reports the magnetic moment response effects in $Sr_2RuO_4$. The experiments performed in [144] do not study how the order parameter winds around a vortex, instead they consider the order parameter around a hole drilled in the center of a sample. When a supercurrent winds around the hole with a magnetic field passed through, the order parameter obtains a phase factor $\Phi = \oint \vec{A} \cdot \mathrm{d}\vec{s} + (4\pi/c) \oint \lambda^2 \vec{j}_s \cdot \mathrm{d}\vec{s} = n\Phi_0$ [121][144]. $n$ is an integer: $n = (1/2\pi) \oint \vec{\nabla}\theta \cdot \mathrm{d}\vec{s}$. The magnetic moments response of the material is given by $\mu = \Delta\mu_z n + \chi H_z$, where $\chi$ is the magnetic susceptibility, and $\Delta\mu_z$ measures how the magnetic moments change with respect to the transition $n \to n'$. Because $n$ must be an integer, $\mu$ exhibits a series of steps. If the transition $n \to n + \frac{1}{2}$ happens, one-half step would appear.

In [122], a method is proposed to detect depinned vortices. Vortices in a superconductor can begin to move by the influences of non-equilibrium effects or thermal fluctuations. The sample film has a hole, through which there is a magnetic flux. Another magnetic field is applied to the rest of the sample. When a current $J_x$ is driven along the $x$ direction, the vortex current $j_y$ along the $y$ direction can induce a voltage drop $V_x = (h/e)j_y$. If the vortex moves coherently, the resistivity contributed by the vortex part contains the information about the braid statistics.

### 5.2.2 Classification

Fermionic Hamiltonians can be classified according to how they are transformed under symmetry operations [162][163]. Two types of symmetry operation called $P$ type and $C$ type are examined for doing the classification [126][127][128][162][164],

$$P : \mathcal{H} = -P\mathcal{H}P^{-1},\ PP^{\dagger} = 1,\ P^2 = 1, \tag{5.10}$$

$$C : \mathcal{H} = \epsilon_c C\mathcal{H}^T C^{-1},\ CC^{\dagger} = 1, C^T = \eta_c C, \tag{5.11}$$

where $\epsilon_c = \pm 1$ and $\eta_c = \pm 1$. The time-reversal symmetry operation and the particle-hole symmetry operation belong to these two types. A time-reversal symmetry operation for spinless or integer spin particles should satisfy the case of C type with$(\epsilon_c, \eta_c) = (1, 1)$. For particles with half-integer spin, a time reversal symmetry operation satisfies the C type symmetry with $(\epsilon_c, \eta_c) = (1, -1)$. $(\epsilon_c, \eta_c) = (-1, 1)$ and $(\epsilon_c, \eta_c) = (-1, -1)$ represent particle-hole symmetry operations for a triplet pairing Hamiltonian and a singlet pairing Hamiltonian respectively. A chiral symmetry (sublattice) is in the P type category. According to the behaviors of Hamiltonians under time-reversal, particle-hole, and chiral symmetry operations, Hamiltonians can be classified into ten classes [162][163][164]. The table of the classification is repeated in Table 5.1 [162].

The Hamiltonian of the $p_x + ip_y$ has the form of the Dirac Hamiltonian, so the same winding number can be defined for the $p_x + ip_y$ system. The BdG Hamiltonian is $H = \sum \Psi(p) h \Psi(p)$

$$h = \begin{pmatrix} \xi(p) & p_x - ip_y \\ p_x + ip_y & -\xi(p) \end{pmatrix} \tag{5.12}$$

| | | TRS | PHS | SLS | $d=1$ | $d=2$ | $d=3$ |
|---|---|---|---|---|---|---|---|
| standard (Wigner-Dyson) | A (unitary) | 0 | 0 | 0 | - | $\mathbb{Z}$ | - |
| | AI (orthogonal) | +1 | 0 | 0 | - | - | - |
| | AII (symplectic) | −1 | 0 | 0 | - | $\mathbb{Z}_2$ | $\mathbb{Z}_2$ |
| chiral (sublattice) | AIII (chiral unitary) | 0 | 0 | 1 | $\mathbb{Z}$ | - | $\mathbb{Z}$ |
| | BDI (chiral orthogonal) | +1 | +1 | 1 | $\mathbb{Z}$ | - | - |
| | CII (chiral symplectic) | −1 | −1 | 1 | $\mathbb{Z}$ | - | $\mathbb{Z}_2$ |
| BdG | D | 0 | +1 | 0 | $\mathbb{Z}_2$ | $\mathbb{Z}$ | - |
| | C | 0 | −1 | 0 | - | $\mathbb{Z}$ | - |
| | DIII | −1 | +1 | 1 | $\mathbb{Z}_2$ | $\mathbb{Z}_2$ | $\mathbb{Z}$ |
| | CI | +1 | −1 | 1 | - | - | $\mathbb{Z}$ |

Table 5.1: The classification table is from [162]. TRS means time reversal symmetry; PHS means particle hole symmetry; SLS means sublattice symmetry. In the symmetry operation column, 0 means the corresponding symmetry is broken; 1 means the system is invariant under this symmetry and the symmetry is implemented by a unitary transformation; −1 means the symmetry is implemented by an anti-unitary transformation.

The Hamiltonian has the form $h(p) = \sum_a n_a(p)\sigma^a$ with $n_a = (p_x, p_y, \xi(p))$. The winding number can be defined as [123]

$$N = \frac{1}{8\pi^2}\int \mathrm{d}^2 p \epsilon^{abc} n_a \frac{\partial n_b}{p_x}\frac{\partial n_c}{\partial p_y}. \tag{5.13}$$

The two dimensional spinless $p_x + ip_y$ superconductor does not have the time-reversal symmetry, and the BdG Hamiltonian is particle-hole symmetric by construction. According to the classification table, the system is classified by an integer, which is the winding number we just defined. In the following sections, we will compute this number in the system of bilayer $CrO_2$.

## 5.3 $CrO_2$ bilayers and lattice model

In its most common form, $CrO_2$ is a three dimensional bulk material with rutile structure [153, 154]. It was recently suggested [156] that $CrO_2/TiO_2$ heterostruc-

tures have fully spin polarized conduction bands over a wide energy window around the Fermi level, and behave effectively as a two dimensional (2D) crystal. In its simplest 2D form, $CrO_2$ will form a bilayer. It is natural to ask if this material could spontaneously develop 2D chiral topological superconducting phases and host Majorana fermions even in the absence of spin-orbit coupling effects [145].

In this Chapter, we start from a lattice model for a single $CrO_2$ bilayer to address the formation of spin triplet pairs with $p_x + ip_y$ symmetry, which may lead to a fully gapped state. We show that at large doping the system has an exotic sequence of topological phase transitions as a function of the chemical potential and interaction strength. Different non-trivial topological phases occur in the vicinity of van-Hove singularities of the band, where the density of states (DOS) diverges, allowing the possibility for both conventional and purely electronic mechanisms. We suggest that this system is a promising candidate for the experimental observation of intrinsic 2D chiral topological superconductivity in the triplet channel.

In a bilayer system, the Cr atoms form two interpenetrating square sublattices, $A$ and $B$, each one sitting on a different layer. From above, the Cr atoms are arranged in a checkerboard pattern, as shown in Fig. 5.1 a. Each site on sublattice $A$ ($B$) has two orbitals with $d_{xy}$ and $d_{xz}(d_{yz})$ symmetry. Nearest neighbors (NN) hopping between a $d_{xy}$ orbital in sublattice $B$ with a $d_{xz}$ orbital in sublattice $A$ has amplitude $t_1$ along the the $(1, \bar{1})$ direction and zero along the $(1, 1)$ direction by symmetry. In the same way, NN hopping between a $d_{xy}$ orbital in sublattice $A$ and with a $d_{yz}$ orbital in $B$ has amplitude $t_2$ along the $(1, 1)$ direction and zero along the other diagonal in the $xy$ plane. Intra-orbital NN hopping is finite between $d_{xy}$ orbitals ($t_3$) but zero between $d_{xz}$ and $d_{yz}$ orbitals ($t_4$), which are

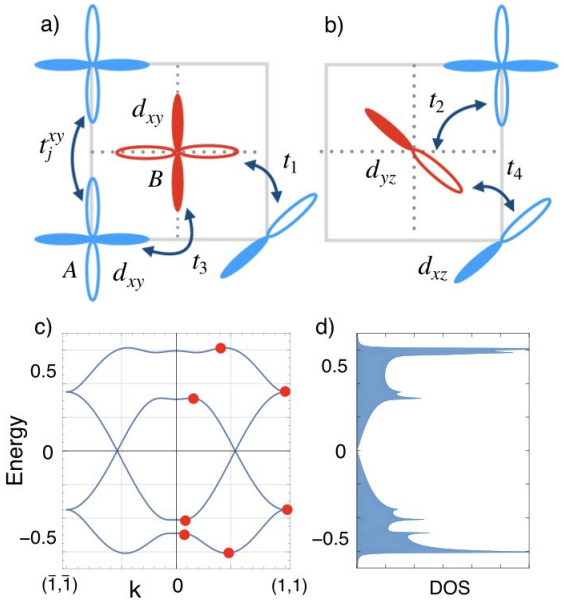


Figure 5.1: top: Lattice of a $CrO_2$ bilayer, with $d_{xy}$ and $d_{xz}$ ($d_{yz}$) orbitals in sublattice $A$ ($B$). The blue orbitals sit in the top layer ($A$ sites), and red orbitals in the lower one ($B$ sites). Hopping energies are indicated by $t_j^\alpha$ for intra-orbital hopping between next-nearest sites, with $\alpha = xy$, $xz$ for $j = A$ and $\alpha = xy$, $yz$ for $j = B$, and $t_i$ ($i = 1, 2, 3, 4$) for nearest neighbor hopping. c) Energy spectrum of the lattice model along the diagonal $(1, 1)$ direction. Energy axes in eV units. Red dots indicate the location of van Hove singularities, where the DOS (d) diverges logarithmically.

othogonal to each other. Among next-nearest neighbors (NNN), the dominant processes are described by intra-orbital hoppings $t_j^\alpha$, with $\alpha = xy$, $xz$ for sites in sublattice $j = A$ and $\alpha = xy$, $yz$ for $B$ sites.

The Hamiltonian can be described in a four component basis

$$\Psi = (\psi_{A,xy}, \psi_{A,xz}, \psi_{B,xy}, \psi_{B,yz}). \tag{5.14}$$

In momentum space, $\mathcal{H}_0 = \sum_{\mathbf{q}} \Psi^\dagger_{\mathbf{q}} h(\mathbf{q}) \Psi_{\mathbf{q}}$, with [156]

$$h(\mathbf{q}) = \begin{pmatrix} h_A & h_{AB} \\ h^\dagger_{AB} & h_B \end{pmatrix}, \tag{5.15}$$

where

$$h_A = \begin{pmatrix} \epsilon^{xy}_A(\mathbf{q}) & 0 \\ 0 & \epsilon^{xz}_A(\mathbf{q}) \end{pmatrix}, \; h_B = \begin{pmatrix} \epsilon^{xy}_B(\mathbf{q}) & 0 \\ 0 & \epsilon^{yz}_B(\mathbf{q}) \end{pmatrix}. \tag{5.16}$$

The diagonal terms incorporate NNN hopping processes, where $\epsilon^\alpha_j(\mathbf{q}) = E^\alpha_j + 4t^\alpha_j \mathrm{cos}q_x \mathrm{cos}q_y$, with $E^\alpha_j$ a local potential on obital $\alpha$ in sublattice $j$ and $q_{x,y} = \frac{1}{2}(k_x \mp k_y)$ the momentum along the two diagonal directions of the crystal. The off-diagonal terms in (5.15) describe the NN hopping terms illustrated in panels a) and b) in Fig. 5.1,

$$h_{AB} = \begin{pmatrix} -2t_3 \sum_{\nu=x,y} \mathrm{cos}q_\nu & 2it_1 \mathrm{sin}q_y \\ 2it_2 \mathrm{sin}q_x & -2t_4 \sum_{\nu=x,y} \mathrm{cos}q_\nu \end{pmatrix}, \tag{5.17}$$

where $t_4 = 0$ by mirror symmetry [155].

The energy spectrum is shown in Fig. 5.1c, and has two sets of Dirac points along the $(1,1)$ and $(1,\bar{1})$ directions, respectively. Enforcing the symmetries of the 2D lattice, namely roto-inversion $S_4$ symmetry and mirror symmetry $M$ at the diagonal directions of the unit cell, we adopt $t_1 = -t_2 \equiv t = 0.3$eV as the leading energy scale, and the set of parameters $t_3 = t/30$, $t^{xy}_j = -t^{xz}_A = -t^{yz}_B = t/3$ and $E^{xy}_j = -E^{xz}_A = -E^{yz}_B = t/6$, following ab initio results [156]. The four band model breaks down near the edge of the band, where states may hybridize with high energy bands. We also assume that the bands are spinless. The resulting band structure has several van Hove singularities at the saddle points, where

the density of states (DOS) diverges logarithmically, as depicted in Fig. 5.1d. In the vicinity of those points (red dots), the system can be unstable towards superconductivity.

## 5.4 Pairing Hamiltonian

For spinless fermions, superconductivity is allowed only in the triplet channel. The wavefunction of the Cooper pairs is anti-symmetric under inversion, and hence only states with odd angular momentum are allowed. When electrons pair accross the center of the Brillouin zone, the lowest symmetry is in the $p$-wave channel. We consider the possible instabilities of the lattice model in the chiral $p + ip$ state, which can produce a fully gapped state and hence is expected to minimize the free energy of the system. A full assessment of the stability of this state requires taking fluctuations into account [157, 158, 159], which will be considered elsewhere.

For NN sites, the effective interaction term has the form

$$\mathcal{H}_{\text{int}} = -\frac{1}{2}\sum_{\mathbf{r}\in\text{NN}} g^{\alpha\beta}\hat{n}_{i,\alpha}(\mathbf{r}_i)\hat{n}_{j,\beta}(\mathbf{r}_j) \tag{5.18}$$

where $\hat{n}_{i,\alpha} = \psi^{\dagger}_{i,\alpha}\psi_{i,\alpha}$ is the density operator in orbital $\alpha$ on sublattice $i = A$, $B$, $g^{\alpha\alpha} \equiv g_1 > 0$ is the intra-orbital coupling, and $g^{xy,yz} = g^{xz,xy} \equiv g_2 > 0$ is the coupling in the inter-orbital channel. The $p+ip$ pairing follows from the Ansatz on the lattice $\Delta^{\alpha\beta}(\delta_n) = g^{\alpha\beta}\langle\psi_{A,\alpha}(\mathbf{r})\psi_{B,\beta}(\mathbf{r}+\vec{\delta}_n)\rangle \equiv \Delta^{\alpha\beta}\mathrm{e}^{i\frac{\pi}{2}n}$, where $\vec{\delta}_{1,3} = \pm\frac{a}{2}(\hat{x}+\hat{y})$ and $\vec{\delta}_{2,4} = \pm\frac{a}{2}(\hat{x}-\hat{y})$ describe the four NN vectors, with $a$ the lattice constant.

Defining $\Delta^{\alpha\alpha} \equiv \Delta_1$ and $\Delta^{\alpha\beta} \equiv \Delta_2$ for intra-orbital and inter-orbital pairing respectively, the order parameter in momentum space $\Delta_i(\mathbf{q}) = \Delta_i(\sin q_y + i\sin q_x)$

has $p_x + ip_y$ symmetry, with $i = 1, 2$. At the mean field level, Hamiltonian (5.15) and (5.18) results in the Bogoliubov-de Gennes (BdG) Hamiltonian $\mathcal{H}_{\rm BdG} = \sum_{\mathbf{k}\in BZ} \Phi^\dagger_{\mathbf{q}} h_{\rm BdG}(\mathbf{q}) \Phi_{\mathbf{q}}$ with $\Phi_{\mathbf{q}} = (\Psi_{\mathbf{q}}, \Psi^\dagger_{-\mathbf{q}})$, which has the form

$$h_{\rm BdG}(\mathbf{q}) = \begin{pmatrix} h(\mathbf{q}) & \hat{\Delta}(\mathbf{q}) \\ \hat{\Delta}^\dagger(\mathbf{q}) & -h^T(-\mathbf{q}) \end{pmatrix}, \tag{5.19}$$

where

$$\hat{\Delta}(\mathbf{q}) = \begin{pmatrix} 0 & \Delta_1(\mathbf{q})\mathbf{1} + \Delta_2(\mathbf{q})\sigma_x \\ \Delta_1(\mathbf{q})\mathbf{1} + \Delta_2(\mathbf{q})\sigma_x & 0 \end{pmatrix} \tag{5.20}$$

is the pairing matrix, with $\sigma_x$ a Pauli matrix in the orbital space.

Minimization of the free energy $\mathcal{F}(\Delta_1, \Delta_2) = -T \mathrm{tr} \sum_{\mathbf{k}} \ln e^{-h_{\rm BdG}(\mathbf{k})/T} + \sum_{i=1,2} |\Delta_i|^2/g_i$ for a fixed chemical potential $\mu$ gives the zero temperature ($T = 0$) phase diagram shown in Fig. 5.2a as a function of the couplings $g_1$ and $g_2$. The inter-orbital channel $g_2$ may lead to gapless $p + ip$ superconductivity ($\Delta_2 \neq 0$) shown in the red region, which is topologically trivial. The dashed line around it in Fig. 2a describes a first order phase transition and sets the boundary of the gapless $p + ip$ phase with the others at $g_2 = g_{2c}(\mu)$. The intra-orbital $p + ip$ pairing state ($\Delta_1 \neq 0$) on the other hand is fully gapped and can be topological.

The gapped state has multiple minima that compete. The dashed vertical line in Fig. 5.2a indicates a first order phase transition between the weak and strong coupling phases of the gapped state at $g_1 = g_{1c}(\mu)$. At this coupling, the superconducting order parameter $\Delta_1$ jumps (see Fig. 5.2b) and different gapped phases with distinct topological numbers coexist. The resulting gap is very anisotropic around the Fermi surface. In the weak coupling phase $\bar{g}_{1c}(\mu) < g < g_{1c}(\mu)$ shown in the light blue region in Fig 5.2a, $\Delta_1$ scales as a power

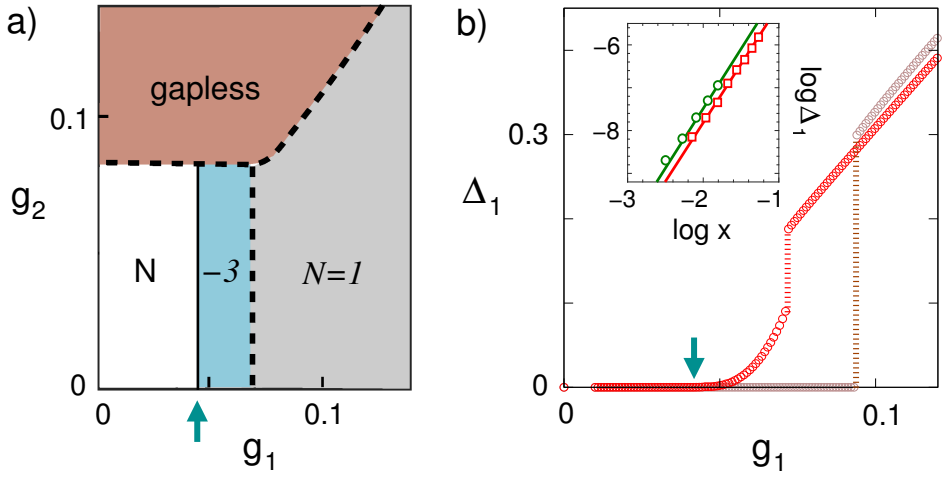


Figure 5.2: (a) Phase diagram in the spinless $p+ip$ state for gapped intra-orbital (gray and blue regions) and gapless inter-orbital pairing (red) at $\mu = 4t/3 = 0.4$ eV. Couplings $g_1$ and $g_2$ in eV units. Dashed lines: first order phase transitions. Gray area: gapped strong coupling phase with Chern number $\mathcal{N} = 1$; Blue: gapped weak coupling one ($\bar{g}_{1c} < g < g_{1c}$) with $\mathcal{N} = -3$ (see Fig. 5.3). Solid black line: second order phase transition to the normal state $N$ ($g = \bar{g}_{1c}$). b) Scaling of the gapped order parameter $\Delta_1$ with $g_1$. Red circles: $\mu = 0.4$ eV; brown: $\mu = 0$. Dotted lines indicate fist order phase transitions. Green arrows: critical coupling $\bar{g}_{1c} \approx t/7 = 0.045$ eV at $\mu = 0.4$ eV. Inset: $\log \Delta_1$ vs $\log x$, with $x = (g/\bar{g}_{c1} - 1)$, showing power law behavior near $\bar{g}_{1c}$. Green dots: $\mu = 0.3\,$eV. Red: $\mu = 0.4$eV.

law with the coupling for fixed $\mu$, $\Delta_1(g_1) \propto (g - \bar{g}_{1c})^{\beta}$, with $\beta \approx 2.7 \pm 0.1$ for $0.2 \lesssim \mu \lesssim 0.4$ eV (see inset). $\Delta_1$ vanishes at the critical coupling $\bar{g}_{1c}$, where the system has a second order phase transition to the normal state, indicated by the green arrows in Fig. 5.2. When $\mu$ is in the immediate vicinity of the van Hove singularities, $\bar{g}_{1c}$ abruptly drops towards zero. This singular behavior suggests a crossover to exponential scaling when the Fermi surface is nested at the van Hove singularities [160].

For large doping, when $\mu$ is large, both $\bar{g}_{1c}$ and $g_{1c}$ shift towards the infrared, and the discontinuity of the order parameter $\Delta_1$ decreases. In general, all the gapped phases prevail over the gapless one ($\Delta_2$). In the opposite regime, at small

doping, the two critical couplings merge ($\bar{g}_{1c} = g_{1c}$) below $|\mu| \lesssim 0.6t$ and the gapped phase has a first order phase transition to the normal state at $g < g_{1c}(\mu)$ (see Fig 5.3).

## 5.5 Topological phase transitions

In two dimension, spinless superconductors with a bulk gap that breaks time reversal symmetry belong to the C class in the ten-fold classification table [162, 163]. The topological number in this class is defined by the BdG Chern number $\mathcal{N}$, which corresponds to the number of chiral Majorana modes propagating along the edge [135, 165].

In Fig. 5.3, we numerically calculate the Chern number

$$\mathcal{N} = (i/2\pi) \int_{BZ} \mathrm{d}^2\mathbf{q}\, \Omega_z(\mathbf{q}) \tag{5.21}$$

in the gapped state as a function of $\mu$ and intra-orbital coupling $g_1$, with $\mathbf{\Omega}(\mathbf{q}) = \nabla_{\mathbf{q}} \times \langle \psi_{n,\mathbf{q}} | \nabla_{\mathbf{q}} | \psi_{n,\mathbf{q}} \rangle$ the Berry curvature from the eigenstates of the BdG Hamiltonian at the Fermi level, $|\psi_{n,\mathbf{q}}\rangle$. By changing the chemical potential, the system shows a sequence of topological phase transitions.

In the weak coupling phase, shown in the blue areas in Fig. 5.3, there are up to five transitions separating different topological phases with $\mathcal{N} = -4$, $-5$, $-6$, $-4$, $-5$, and $-3$, in the range of $-2t \leq \mu \leq 2t = 0.6$eV. The critical values of the chemical potential where the system has a topological phase transition are close to the energy of the van Hove singularities of the band (see Fig. 5.1c) and coincide with the energies where the topology of the Fermi surface changes. At those critical values, the superconducting gap closes and the

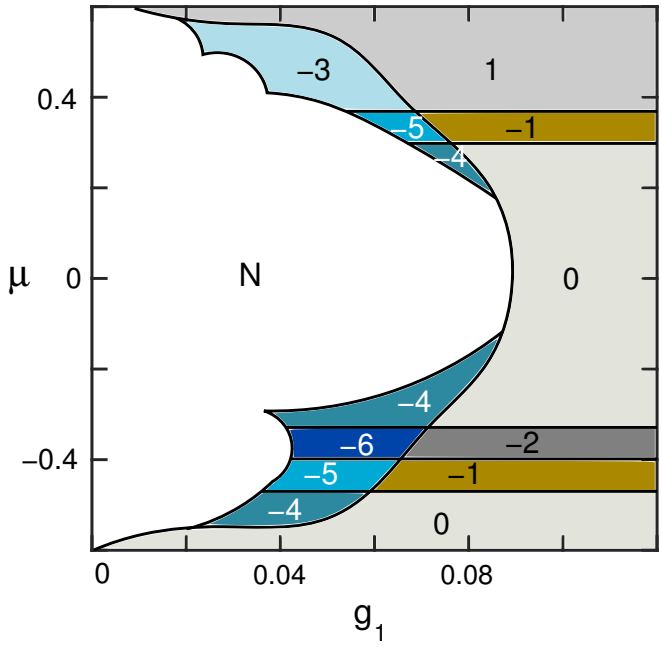


Figure 5.3: Phase diagram showing the different topological phases as a function of the chemical potential $\mu$ and intra-orbital pairing coupling $g_1$, both in eV units. The integers indicate the corresponding BdG Chern number $\mathcal{N}$. For fixed $g_1$, the system has a sequence of topological phase transitions near the van-Hove singularities of the band, where the topology of the Fermi surface changes. The blue regions correspond to the weak coupling gapped phases of superconductivity, which are topological. Gray and maroon regions: strong coupling phases. $N$ region: normal.

Chern number jumps by an integer number. The line $g_1 = \bar{g}_{1c}(\mu)$ separates the blue areas from the normal region through continuous phase transitions. As anticipated, when $|\mu| \lesssim 0.6t = 0.18\text{eV}$, $\bar{g}_{1c} = g_{1c}$, and the weak coupling phases are suppressed. The singular behavior of $\bar{g}_{1c}(\mu)$ when $\mu$ is at the van Hove singularity is not captured by the numerics shown in Fig. 5.3 due to the smallness of the gap.

The solid curve separating the blue regions in Fig. 5.3 from the strong coupling phases sets $g_{1c}(\mu)$, which describes a line of first order phase transitions between different gapped phases. At this line, the order parameter is discontinuous [161],

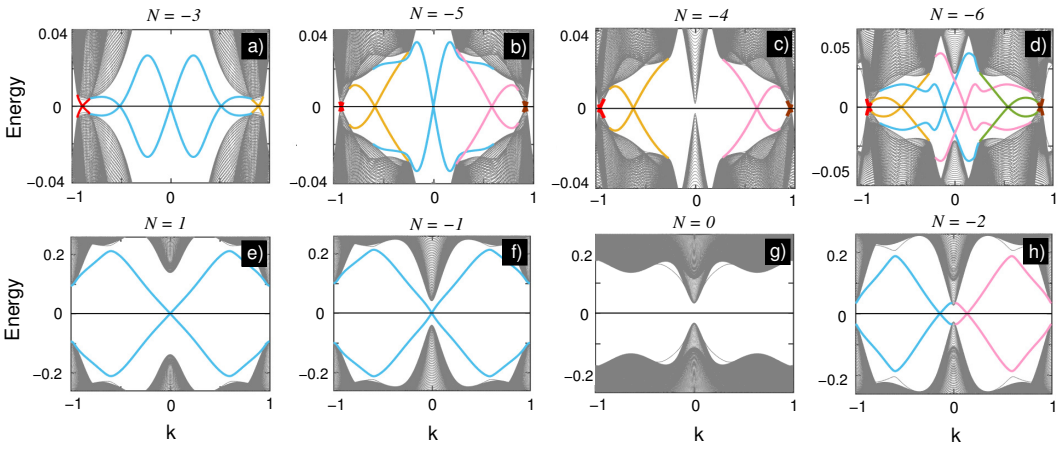


Figure 5.4: Majorana edge modes in the different topological phases in the gapped $p + ip$ state. Energy units in eV. a) BdG Chern number $\mathcal{N} = -3$ state, at $\mu = 0.44$eV. b) $\mathcal{N} = -5$ at $\mu = 0.33$eV; c) $\mathcal{N} = -4$ at $\mu = -0.49$ eV and d) $\mathcal{N} = -6$ at $\mu = -0.38$ eV in the weak coupling regime. The lower panels give the corresponding phases in the strong coupling sector: e) $\mathcal{N} = 1$ at $\mu = 0.44$eV, f) $\mathcal{N} = -1$ at $\mu = 0.33$eV; g) $\mathcal{N} = 0$ at $\mu = -0.49$ eV, which is topologically trivial and h) $\mathcal{N} = -2$ at $\mu = -0.38$eV. At the crossing from the weak to strong coupling phases, when $g = g_{1c}(\mu)$, all Chern numbers increase by 4.

indicating the onset of a topological phase transition as a function of $g_1$ for fixed $\mu$. In all cases, the Chern number changes accross the $g_{1c}(\mu)$ line by $\Delta\mathcal{N} = 4$. Deep in the strong coupling regime (gray and maroon regions), for fixed $g > g_{1c}(\mu = 0)$, there are six topological phase transitions separating the phases $\mathcal{N} =$ 0, $-1$, $-2$, 0, $-1$, 1, 0 as a function of the chemical potential. At the wide doping window $1.27t \lesssim \mu \lesssim 2t = 0.6$ eV, the elemental chiral topological superconducting phase with $\mathcal{N} = \pm 1$, and hence a single Majorana mode, can emerge at strong coupling.

## 5.6 Chiral Majorana edge states

To explicitly verify the Chern numbers for the different phases, we calculate the edge modes of the gapped state in a two dimensional strip geometry with edges

oriented along the $(1,0)$ direction.

The plots in Fig. 5.4a−d (top row) show the evolution of the edge modes in the weak coupling regime ($\bar{g}_{1c} < g < g_c(\mu)$) for different values of $\mu$. The $\mathcal{N} = -3$ state shown in Fig. 5.4a has five edge modes in total, but only three modes that are topologically protected, as indicated by the three different colors. The three modes indicated in blue can be adiabatically deformed into a single zero energy crossing at $k = 0$, and hence count as a single topologically protected mode. By decreasing the chemical potential into the contiguous $\mathcal{N} = -5$ state (Fig. 5.4b), two of those modes become topologically protected, raising the number of Majorana modes to five. By reducing $\mu$ further into the $\mathcal{N} = -4$ state, the topology of the Fermi surface changes drastically, forming gapped pockets of charge around four Dirac nodes, indicated in Fig. 5.1c. Panel d shows the edge modes of the $\mathcal{N} = -6$ state, for $\mu \lesssim -t = -0.3$ eV. The corresponding edge modes in the strong coupling regime ($g > g_{1c}(\mu)$) with $\mathcal{N} = 1$, $-1$, 0, and $-2$ are shown in the bottom row of Fig. 5.4 (e−h).

## 5.7 Pairing Mechanism

Although it is difficult to reliably predict a mechanism of superconductivity, the fact that topological superconductivity develops near van Hove singularities, where the DOS is very large, indicates that both phonons and electronic interactions could be suitable candidates for a pairing mechanism at large doping. We will not discuss the phonon mechanism, since it is conventional.

Electronic mechanisms typically provide attraction when the charge susceptibility at the Fermi surface nesting vector $\mathbf{Q}$ satisfies $\chi(\mathbf{Q}) > \chi(0)$ [166]. When the chemical potential $\mu$ is close to a Van Hove singularity, the electronic bands

have energy spectrum $\epsilon(\mathbf{q}) = -\alpha q_x^2 + \beta q_y^2$, $(0 < \alpha \leq \beta)$ where $\mathbf{q}$ is the momentum away from the saddle point. The susceptibility in the vicinity of the singularity is logarithmic divergent, $\chi(0) = \frac{1}{2\pi^2}/\sqrt{\alpha\beta}\ln(\Lambda/\delta\mu)$ with $\delta\mu$ the deviation away from the van Hove and $\Lambda \sim t$ an ultraviolet cut-off around the saddle point [167]. At the nesting wavevector $\epsilon(\mathbf{q}+\mathbf{Q}) = -\alpha p_y^2 + \beta p_x^2$ , the susceptibility is

$$\chi(\mathbf{Q}) = c/(\alpha+\beta)\ln(\Lambda/\delta\mu)\,, \tag{5.22}$$

where the constant $c = \frac{1}{\pi^2}\ln(\sqrt{\frac{\alpha}{\beta-\alpha}} + \sqrt{\frac{\beta}{\beta-\alpha}})$ is logarithmically divergent at the nesting condition $\alpha = \beta$ [172]. For the particular lattice Hamiltonian parametrization taken from Ref. [156], the fitting of the bands around the van Hove at $\mu = 0.312$ eV has $\alpha \approx 1.2$ and $\beta \approx 1.7$. That gives the ratio $\chi(\mathbf{Q})/\chi(0) \sim 1.20$, suggesting that a purely electronic mechanism of superconductivity is possible [167, 169].

The high doping regime could in principle be reached with gating effects for $CrO_2$ encapsulated in an insulating substrate [170] that preserves the roto-inversion symmetry of the lattice.

## 5.8 Summary

We have examined the $p+ip$ pairing states for a lattice model of $CrO_2$ bilayers, and showed that a variety of triplet chiral topological superconducting phases are allowed at large doping. Due to the large DOS at the saddle points of the band, different pairing mechanisms are possible, including purely electronic ones. We showed that $CrO_2$ bilayers are promising materials for the observation of chiral topological superconductivity in 2D.

# Chapter 6

# Conclusion

In this thesis, we mainly studied the properties of generalized Dirac nodal systems in two dimension. Many questions arise if we want to study the interaction effects in these systems. Roughly speaking, we would like to know if new phases can appear when interactions are added.

In the ABC-stacked trilayer graphene system, we studied how the "free" quasiparticles are renormalized by the Coulomb interaction. With the result of polarization bubble and Fermi self-energy, we further computed several concrete physical observables which are renormalized by the electron-electron interactions. We believe that these renormalization effects leave hints which may be potentially detected in experiments.

"Frustration" due to competition among different interactions may lead to exotic phases like a quantum spin liquid. In the second part of the thesis the spin-orbital liquid phases are proposed in Dirac-material-based impurity superlattices. More concretely, we propose a controllable system in which an artificial Mott insulator can be achieved. Due to the flexible of the designing of the system, spin-orbital liquids ground state may be possible in a totally tunable parameter

region. In addition, different geometries of lattice can be realized in this system, which provide more opportunities for new physics.

In the third part the instability of the chiral topological superconductivity in the chromium dioxide bilayers was examined. Inspired by the half-metallic property of chromium dioxide, we investigated the spin triplet p+ip superconductivity in the chromium dioxide bilayers. In the parameter space extended by the chemical potential and the interaction strength, we identify several areas where a non-trivial topological Majorana mode can appear. Topological phase transitions in this system are also studied. The key result for this is that the topological phase transitions appear near the von Hove singularities. A remaining question is whether the mean field result is still robust when fluctuation effects are taken into account. Numerical simulation results will be also useful for providing more information about this question.

As discussed above the main focus is on two-dimensional or quasi-2D systems. In three dimension space, we still do not understand the chiral-induced transport properties of new Weyl materials like TaP, NbAs, and NbP. Type-II Weyl semimetals which have different Weyl nodes are also proposed, in which Weyl points are the touching points of electron and hole pockets [174]. Dirac loop semimetals present harder questions for experimental measurements: if there are no exotic surface states, one can not infer the properties in the bulk by measuring surface states.

# Bibliography


[1] A. H. Castro Neto, N. M. R. Peres, F. Guinea, K. Novoselov, A. K. Geim, Rev. Mod. Phys. 81 109 (2009).

[2] V. N. Kotov *et al.*, Rev. Mod. Phys. 84, 1067 (2012).

[3] Victor Pardo and Warren E. Pickett, Phys. Rev. Lett. 102, 166803

[4] Pavan Hosur and Xiao-Liang Qi, Comptes Rendus Physique Volume 14, Issues 9-10, November-December 2013, Pages 857-870.

[5] C. Fang *et al.*, arXiv:1609.05414.

[6] K. F. Mak, J. Shan, T. F. Heinz, Phys. Rev. Lett. 106, 046401 (2011).

[7] X. Dou, A. Jaefari, Y. Barlas, B. Uchoa, Phys. Rev. B 90, 161411(R) (2014), arXiv:1407.6021.

[8] X. Dou, Valeri N. Kotov, B. Uchoa, Scientific Reports 6, 31737 (2016), arXiv:1602.01477.

[9] X. Dou, K. Seo, B. Uchoa, arXiv:1803.05571.

[10] M.Z. Hasan and C.L. Kane, Rev. Mod. Phys. 82, 3045 (2010).

[11] D. Xiao, M.-C. Chang, and Qian Niu, Rev. Mod. Phys. 82, 1959 (2010).

[12] D. J. Thouless, M. Kohmoto, M. P. Nightingale, M. den Nijs, Phys. Rev. Lett. 49, 405 (1982).

[13] B.A. Bernevig and T.L. Hughes, Topological Insulators and Topological Superconductors, Princeton University Press (2013).

[14] A.M. Polyakov, Gauge Fields and Strings, CRC press (1987).

[15] A. Yacoby, Nat. Phys. 7, 925 (2011).

[16] C. H. Lui, Z. Li, K.F. Mak, E. Cappelluti, T.F. Heinz, Nat. Phys. 7, 944Ð947 (2011).

[17] W. Bao, L. Jing, Y. Lee, J. Velasco Jr., P. Kratz, D. Tran, B. Standley, M. Aykol, S. B. Cronin, D. Smirnov, M. Koshino, E. McCann, M. Bockrath, C.N. Lau, Nat. Phys. 7, 948–952 (2011).

[18] M. Koshino, Phys. Rev. B 81, 125304 (2010).

[19] M. Koshino, T. Ando, Phys. Rev. B 76, 085425 (2007).

[20] S. Coleman, Aspects of symmetry: Selected Erice lectures, Cambridge University Press 1985.

[21] M. Marino, Instantons and Large N: An Introduction to Non-Perturbative Methods in Quantum Field Theory, Cambridge University Press 2015

[22] V. N . Kotov, B. Uchoa, V. M. Pereira, F. Guinea, A. H. Casto Neto, Rev. Mod. Phys. **84**, 1067 (2012).

[23] F. Guinea, A. H. Castro Neto, N. M. R. Peres, Phys. Rev. B **73**, 245426 (2006).

[24] F. Zhang, B. Sahu, H. Min, and A. H. MacDonald, Phys. Rev. B **82**, 035409 (2010).

[25] V. Cvetkovic, and O. Vafek, arXiv:1210.4923v1 (2012).

[26] J. Jia, E. V. Gorbar, and V. P. Gusynin, Phys. Rev. B **88**, 205428 (2013).

[27] R. Olsen, R. van Gelderen, and C. Morais Smith, Phys. Rev. B **87**, 115414 (2013).

[28] Y. Lee, D. Tran, K. Myhro, J. Velasco Jr., N. Gillgren, C. N. Lau, Y. Barlas, J.M. Poumirol, D. Smirnov, F. Guinea, arXiv:1402.6413.

[29] Y. Barlas, and K. Yang, Phys. Rev. **B** 80, 161408 (2009).

[30] S. Gangadharaiah, A. M. Farid, E. G. Mishchenko, Phys. Rev. Lett. **100**, 166802 (2008).

[11] H. Min, E. H. Hwang, S. Das Sarma, Phys. Rev. B **86**, 081402(R) (2012).

[31] R. van Gelderen, R. Olsen, C. Morais Smith, Phys. Rev. B **88**, 115414 (2013).

[32] M. G. Menezes, R. B. Capaz, S. G. Louie, Phys. Rev. B **89**, 035431 (2014).

[33] D. T. Son, Phys. Rev. B **75**, 235423 (2007).

[34] M. S. Foster, I. L. Aleiner, Phys. Rev. B **77**, 195413 (2008).

[35] V. N. Kotov, B. Uchoa, A. H. Castro Neto, Phys. Rev. B **80**, 165424 (2009).

[36] Y. Lemonik, I. L. Aleiner, C. Toke, V. I. Fal'ko, Phys. Rev. B **82**, 201408(R) (2010).

[37] R. Nandkishore, L. Levitov, Phys. Rev. B **82**, 115431 (2010).

[38] J. J. Quinn and R. A. Ferrell, Phys. Rev. **112**, 812 (1958).

[39] G. Li, A. Luican, E. Y. Andrei, Phys. Rev. Lett. **102**, 176804 (2009).

[40] M. Yankowitz, J. I.-J. Wang, A. G. Birdwell, Y.-A. Chen, K. Watanabe, T. Taniguchi, P. Jacquod, P. San-Jose, P. J.-Herrero, B. J. LeRoy, Nat. Materials **13**, 786 (2014).

[41] J. Martin, N. Akerman, G. Ulbricht, T. Lohmann, J. H. Smet, K. Von Kliyzin, A. Yacoby, Nat. Phys. **4**, 144 (2008).

[42] G. D. Mahan, Many particle Physics, (Plenum, New York, third edition).

[43] A. H. Castro Neto, F. Guinea, N. M. R. Peres, K. S. Novoselov, and A. K. Geim Rev. Mod. Phys. 81, 109 (2009)

[44] M.E. Peskin, D.V. Schroeder, An introduction to quantum field theory, Westview Press (1995).

[45] N.P. Armitage, E.J. Mele, A. Vishwanath, Rev. Mod. Phys. 90, 015001(2018).

[46] L. Balents, Physics 4, 36 (2011).

[47] Xiangang Wan, Ari M. Turner, Ashvin Vishwanath, and Sergey Y. Savrasov, Phys. Rev. B 83, 205101(2011)

[48] Xu, S.-Y., Belopolski, I., Alidoust, N., Neupane, M., Bian, G., Zhang, C., Sankar, R., Chang, G., Yuan, Z., Lee, C.-C., Huang, S.-M., Zheng, H., Ma, J., Sanchez, D. S., Wang, B. K., Bansil, A., Chou, F.-C., Shibayev, P. P., Lin, H.; Jia, S., Hasan, M. Z., Science 349: 613-617 (2015)

[49] L. X. Yang, Z. K. Liu, Y. Sun, H. Peng, H. F. Yang, T. Zhang, B. Zhou, Y. Zhang, Y. F. Guo, M. Rahn, D. Prabhakaran, Z. Hussain, S.-K. Mo, C. Felser, B. Yan, Y. L. Chen, Nature Physics 11, pages 728-732 (2015)

[50] A. A. Zyuzin, A. A. Burkov, Phys. Rev. B 86, 115133 (2012)

[51] P. Goswami and S. Tewari, Phys. Rev. B 88, 245107 (2013)

[52] Xiaochun Huang, Lingxiao Zhao, Yujia Long, Peipei Wang, Dong Chen, Zhanhai Yang, Hui Liang, Mianqi Xue, Hongming Weng, Zhong Fang, Xi Dai, and Genfu Chen, Phys. Rev. X 5, 031023 2015

[53] Cheng-Long Zhang, Su-Yang Xu, Ilya Belopolski, Zhujun Yuan, Ziquan Lin, Bingbing Tong, Guang Bian, Nasser Alidoust, Chi-Cheng Lee, Shin-Ming Huang, Tay-Rong Chang, Guoqing Chang, Chuang-Han Hsu, Horng-Tay Jeng, Madhab Neupane, Daniel S. Sanchez, Hao Zheng, Junfeng Wang, Hsin Lin, Chi Zhang, Hai-Zhou Lu, Shun-Qing Shen, Titus Neupert, M. Zahid Hasan, Shuang Jia, Nature Communications 7, 10735 (2016)

[54] M.P.A. Fisher, In: Comtet A., JolicÏur T., Ouvry S., David F. (eds) Aspects topologiques de la physique en basse dimension. Topological aspects of low dimensional systems. Les Houches - Ecole dÕEte de Physique Theorique, vol 69. Springer, Berlin, Heidelberg (1999).

[55] A. Auerbach, Interacting Electrons and Quantum Magnetism, Springer (1998).

[56] E. Manousakis, Rev. Mod. Phys. 63, 1 (1991).

[57] P.W. Anderson, Mater. Res. Bull. 8, 153 (1973).

[58] M. F. Collins, Magnetic Critical Scattering, Oxford U. Press (1989).

[59] C.L. Gao, W. Wulfhekel, J. Kirschner, Phys. Rev. Lett. 101, 267205 (2008).

[60] L. Savary, L. Balents, Rep. Prog. Phys. 80, 016502 (2017).

[61] T. Imai, Y. Lee, Physics Today 69, 8, 30 (2016).

[62] X.G. Wen, F. Wilczek, A. Zee, Phys. Rev. B 39, 11413 (1989).

[63] A. Kitaev, Ann. Phys.,303 (1), 2 Ð 30.

[64] A. Kitaev, C. Laumann, arXiv:0904.2771.

[65] A. Kitaev, J. Preskill, Phys.Rev.Lett. 96 (2006) 110404.

[66] M. Levin, X.-G. Wen, Phys. Rev. Lett., 96, 110405 (2006).

[67] X.-G. Wen, Phys. Rev. B 65, 165113 (2002).

[68] S. Sachdev and N. Read, Int. J. Mod. Phys. B 5, 219 (1991).

[69] S. Sachdev, Phys. Rev. B 45, 12377 (1992).

[70] S. Yamashita, T. Yamamoto, Y. nakazawa, M. Tamura, R. Kato, Nature Communications volume 2, Article number: 275 (2011).

[71] Tian-Heng Han, Joel S. Helton, Shaoyan Chu, Daniel G. Nocera, Jose A. Rodriguez-Rivera, Collin Broholm, Young S. Lee, Nature 492, 406-410 (2012).

[72] P. A. Lee, Science **321**, 1306 (2008).

[73] L. Balents, Nature **464**, 199–208 (2010).

[74] Y. Kitaoka, *et al.*, J. Phys. Soc. Jpn **67**, 3703 (1998).

[75] M. V. Mostovoy,& D. I. Khomskii, Phys. Rev. Lett. **89**, 227203 (2002).

[76] A. J. W. Reitsma, L. F. Feiner, A. M. Oles, New J. Phys. **7**, 121 (2005).

[77] V. Fritsch, *et al.* Phys. Rev. Lett. **92**, 116401 (2004).

[78] F. Vernay, K. Penc, P. Fazekas, F. Mila, . Phys. Rev. B **70**, 014428 (2004).

[79] M. Bonda, *et al.*, Phys. Rev. B **78**, 104409 (2008).

[80] R. Fichtl, P. Lunkenheimer, J. Hemberger, V. Tsurkan, A. Loidl, J. Non-Cryst. Solids **351**, 2793–2797 (2005).

[81] M. J. Lewis, *et al.*, Phys. Rev. B **72**, 014408 (2005).

[82] S. Nakatsuji, *et al.*, Science **336**, 559 (2012).

[83] Y. Ishiguro, *et al.* Nat. Comm. **4**, 1 (2013).

[84] Y. Q. Li, M. Ma, D. N. Shi, F. C. Zhang, Phys. Rev. Lett. **81**, 3527 (1988).

[85] A. V. Gorshkov, et al., Nat. Phys. **6**, 289 (2010).

[86] X. Zhang, et al., Science **345**, 1467 (2014).

[87] R. Jördens, N. Strohmaier, K. Gunter, H. Moritz, T. A. Esslinger, Nature **455**, 204 (2008).

[88] A. M. Cazalilla, Rey, Rep. Prog. Phys. **77**, 124401 (2014).

[89] K. I. Kugel, D. I. Khomskii, A. O. Sboychakov, S. V. Streltsov, Phys. Rev. B **91**, 155125 (2015).

[90] V. M. Pereira, V. H. Kotov, A. H. Castro Neto, Phys. Rev. B **78**, 085101 (2008).

[91] D. S. Novikov, Phys. Rev. B **76**, 245435 (2007).

[92] V. N. Kotov, B. Uchoa, V. M. Pereira, F. Guinea,& A. H. Castro Neto, Rev. Mod. Phys. **84**, 1067 (2012).

[93] M. O. Goerbig, Rev. Mod. Phys. **83**, 1193 (2011).

[94] A. F. Young, *et al.*, Nature Phys. **8**, 550 (2012).

[95] A. F. Young, *et al.*, Nature **505**, 528 (2013).

[96] K. Nomura, A. H. McDonald, Phys. Rev. Lett. **96**, 256602 (2006).

[97] J. Alicea, M. P. A. Fisher, Phys. Rev. B **74**, 075422 (2006).

[98] D. A. Abanin, B. E. Feldman, A. Yacoby, B. I. Halperin, Phys. Rev. B **88**, 115407 (2013).

[99] I. Sodemann, A. H. MacDonald, Phys. Rev. Lett. **112** 126804 (2014).

[100] S. Y. Zhou, *et al.*, Nature Mater. **6**, 770 (2007).

[101] M. S. Nevius, *et al.*, Phys. Rev. Lett. **115**, 136802 (2015).

[102] P. Corboz, M. Lajko, A. M. Lauchli, K. Penc, F. Mila, Phys. Rev. X **2**, 041013 (2012).

[103] K. Penc, M. Mambrini, P. Fazekas, F. Mila, Phys. Rev. B **68**, 012408 (2003).

[104] P. Corboz, A. M. Lauchli, K. Penc, M. Troyer, F. Mila, Phys. Rev. Lett. **107**, 215301 (2011).

[105] F. Wang, A. Vishwanath, Phys. Rev. B **80**, 064413 (2009).

[106] J. Reinhardt, W. Greiner, Rep. Prog. Phys. **40**, 219 (1977).

[107] Y. B. Zeldovich, V. S. Popov, Sov. Phys. Usp. **14**, 673 (1972).

[108] K. I. Kugel, D. I. Khomskii, Sov. Phys. Usp. **25**, 231 (1982).

[109] D. M. Eigler, E. K. Schweizer, Nature **344**, 524 (1990).

[110] K. F. Mak, C. Lee, J. Hone, J. Shan, T.F. Heinz, Phys. Rev. Lett. **105**, 136805 (2010).

[111] Z. Y. Zhu, Y. C. Cheng, U. Schwingenschlögl, Phys. Rev. B **84**, 153402 (2011).

[112] M. Caragiu, S. Finberg, J. Phys. Condens. Matter **17**, R995 (2005).

[113] V.W. Brar, *et al.*, Nat. Phys. **7**, 43 (2011).

[114] M. Hermele, T. Senthil, M.P.A. Fisher, Phys. Rev. B **72**, 104404 (2005).

[115] B. Marston, I. Affleck, Phys. Rev. B **37**, 3774 (1988).

[116] S. Chatterjee, S. Sachdev, Phys. Rev. B **92**, 165113 (2015).

[117] C. -Z., Chen, Q. Sun, F. Wang, X. C. Xie, Phys. Rev. B **88**, 041405(R) (2013).

[118] H. -H. Hung, Y. Yang, C. Wu, Phys. Rev. B **84**, 054406 (2011).

[119] M. Fu, T. Imai, T. -H. Han, Y. S. Lee, Science **350,** 655 (2015).

[120] B. Uchoa, V. N. Kotov, M. Kindermann, Phys. Rev. B **91**, 121412(R) (2015).

[121] N. Nagaosa, Quantum field theory in condensed matter physics, Springer (1995).

[122] S. D. Sarma, C. Nayak, S. Tewari, Phys. Rev. B 73, 220502(R) (2006).

[123] G. Volovik, The Universe in a Helium Droplet, Oxford University Press, Oxford (2003).

[124] Y. K. Takahashi, A. Srinivasan, B. Varaprasad, A. Rajanikanth, N. Hase, T. M. Nakatani, S. Kasai, T. Furubayashi, K. Hono, Appl.Phys.Lett. 98, 152501(2011).

[125] W. Wang, H. Sukegawa, R. Shan, S. Mitani, K. Inomata, Appl. Phys. Lett. 95, 182502 (2009).

[126] A. Altland, M. R. Zirnbauer, Phys. Rev. B 55, 1142 (1997).

[127] P. Heinzner, A. Huck Leberry, and M. R. Zirnbauer, Commun. Math. Phys. 257, 725 (2005).

[128] D. Bernard, A. LeClair, J. Phys. A 35, 2555 (2002).

[129] Yu. S. Dedkov, M. Fonine, C. König, U. Rüdiger, and G. Güntherodt, Appl. Phys. Lett. **80**, 4181 (2002).

[130] R. J. Soulen, J. M. Byers, M. S. Osofsky, B. Nadgorny, T. Ambrose, S. F. Cheng, P. R. Broussard, C. T. Tanaka, J. Nowak, J. S. Moodera, A. Barry, and J. M. D. Coey, Science **282**, 85 (1998).

[131] W. E. Pickett, Phys. Rev. Lett. **77**, 3185 (1996).

[132] C. Kallin and J. Berlinsky, Rep. Prog. Phys. **79**, 54502 (2016).

[133] Y. Maeno, S. Kittaka, T. Nomura, S. Yonezawa, K. Ishida, J. Phys. Soc. Jpn. **81,** 011009 (2012).

[134] A. P. Mackenzie and Y. Maeno, Rev. Mod. Phys. **75**, 657 (2003).

[135] N. Read and D. Green, Phys. Rev. B **61**, 10267 (2000).

[136] X.-L. Qi, T. L. Hughes, S. Raghu, and S.-C. Zhang, Phys. Rev. Lett. **102**, 187001 (2009)

[137] X.-L. Qi, and S.-C. Zhang, Rev. Mod. Phys. **83,** 1057 (2011).

[138] J. Alicea, Rep. Prog. Phys. **75**, 076501 (2012).

[139] P. A. Lee, Science **346**, 545-546 (2014).

[140] M. Sato and Y. Ando, Rep. Prog. Phys. **80**, 076501 (2017).

[141] R. Jackiw and P. Rossi, Nucl. Phys. B 190, 681 (1981).

[142] J. P. Xu *et al.*, Phys. Rev. Lett. **114**, 017001 (2015).

[143] S. B. Chung, H. Bluhm, and E.-A. Kim, Phys. Rev. Lett. **99**, 197002 (2007).

[144] J. Jang, D. G. Ferguson, V. Vakaryuk, R. Budakian, S. B. Chung, P. M. Goldbart, Y. Maeno, Science **331**, 186 (2011).

[145] L. Fu and C. L. Kane Phys. Rev. Lett. **100**, 096407 (2008).

[146] A. R. Akhmerov, Johan Nilsson, and C. W. J. Beenakker, Phys. Rev. Lett. **102**, 216404 (2009).

[147] L. Fu, C. L. Kane, Phys. Rev. Lett. **102**, 216403 (2009).

[148] R. M. Lutchyn, J. D. Sau, and S. Das Sarma, Phys. Rev. Lett. **105**, 077001 (2010).

[149] S. B. Chung, H.-J. Zhang, X.-L. Qi, and S.-C. Zhang, Phys. Rev. B **84**, 060510(R) (2011).

[150] J. Li, T. Neupert, Z. J. Wang, A. H. MacDonald, A. Yazdani, B. A. Bernevig, Nat. Comm. **7**, 12297 (2016).

[151] X.-L. Qi, T. L. Hughes, and S.-C. Zhang, Phys. Rev. B **82**, 184516 (2010).

[152] Q. L. He *et al.,* Science **357**, 294 (2017).

[153] K. Schwarz, Journal of Physics F-Metal Physics **16**, L211 (1986).

[154] M.I. Katsnelson, V.Yu. Irkhin, L. Chioncel, A.I. Lichtenstein, R.A. de Groot, Rev. Mod. Phys. **80**, 315 (2008).

[155] Spin-orbit coupling can break mirror symmetry and lead to a finite imaginary $t_4 = it/8 \approx \pm(i)0.036$ eV. See Ref. [156]. This term opens a small gap of $\sim 4$ meV at the Dirac nodes and has no consequence in the large doping regime.

[156] T. Cai, X. Li, F. Wang, S. Ju, J. Feng, and C.-D. Gong, Nano Lett. **15**, 6434 (2015).

[157] N. Furukawa, T. M. Rice, and M. Salmhofer, Phys. Rev. Lett. **81**, 3195 (1998).

[158] R. Nandkishore, L. S. Levitov and A. V. Chubukov, Nat. Phys. **8**, 158 (2012).

[159] M. L. Kiesel, C. Platt, W. Hanke, D. A. Abanin, and R. Thomale, Phys. Rev. B **86**, 020507(R) (2012).

[160] Appendix C

[161] The spectral gap does not close along the line of first order topological phase transitions. The gap closes, however, if $\Delta_1$ is virtually changed as a continuous parameter connecting two topologically distinct ground states.

[162] A. P. Schnyder, S. Ryu, A. Furusaki, and A. W. W. Ludwig, Phys. Rev. B **78**, (2008).

[163] S. Ryu, A. Schnyder, A. Furusaki, and A. Ludwig, New J. Phys. **12**, 65010 (2010).

[164] C.-K. Chiu, J.C.Y. Teo, A.P. Schnyder, S. Ryu, Rev. Mod. Phys. 88, 035005 (2016).

[165] D. J. Thouless, M. Kohmoto, M. P. Nightingale, M. de Nijs, Phys. Rev. Lett. **49**, 405 (1982).

[166] W. Kohn, J. M. Luttinger, Phys. Rev. Lett. **15**, 524 (1965).

[167] J. Gonzalez, Phys. Rev. B **78**, 205431 (2008).

[168] P. C. Pattnaik, C. L. Kane, D. M. Newns, C. C. Tsuei, Phys. Rev. B **45**, 5714 (1992).

[169] F. Guinea, B. Uchoa, Phys. Rev. B **86**, 134521 (2012).

[170] Mayorov *et al.*, Nano Lett. **11**, 2396 (2011).

[171] T. Cai, X. Li, F. Wang, S. Ju, J. Feng, and C.-D. Gong, Nano Lett. **15**, 6434 (2015).

[172] P. C. Pattnaik, C. L. Kane, D. M. Newns, C. C. Tsuei, Phys. Rev. B **45**, 5714 (1992).

[173] M.Yu. Kagan, V.V.Val'kov, V.A. Mitskan, M.M. Korovushkin, JETP **118**, 995 (2014).

[174] A.A. Soluyanov, D. Gresch, Z. Wang, Q. Wu, M. Troyer, X. Dai, B. A. Bernevig, Nature 527, 495 (2015).

# Appendix A

## A.1 Details of methods used in Chapter 4

### A.1.1 Wavefunctions

We assume a real space cut-off for the Coulomb interaction $a = \lambda_C/18$. For a typical mass gap energy $mv^2 \approx 0.13$ eV and $\hbar v \approx 6$eVÅ, as in graphene on SiC, the Compton wavelength $\lambda_C \sim 50$Å, which corresponds to $a \approx 2.8$Å. This number agrees with the typical size of many Coulomb impurities, including alkaline metals.

The analytical form of the 2D Coulomb impurity wavefunctions in the weak coupling regime ($g \ll 1$) is well known [91, 92]. In that regime the cutoff does not play an important role (can be set to zero) and the bound states are shallow. The wavefunctions in the subcritical strong coupling regime ($0.5 \lesssim g < g_c$) can be solved analytically as well. They correspond to the solution of the Dirac equation in the potential (4.10) and bare strong similarity to the 3D Dirac equation ($\text{QED}_{3+1}$) case [106, 107].

Setting $\hbar = v = 1$, for $r > a$, the strong coupling solution in the subcritical

regime has spinor component amplitudes [**?**]

$$F_j^{(\pm)}(r) = \sqrt{m \mp \epsilon}\, e^{-\rho/2} \rho^{-\gamma-1/2} \frac{\Gamma(2s\gamma)}{\Gamma(s\gamma - \tilde{\epsilon})} G^{(\pm)}(r), \tag{A.1}$$

where $\gamma = \sqrt{j^2 - g^2}$, $\beta = \sqrt{m^2 - \epsilon^2}$, $\Gamma(x)$ is a gamma function and

$$\begin{aligned} G^{(\pm)}(r) \;\equiv\; & \sum_{s=\pm 1} [\mathcal{F}(-\gamma - \tilde{\epsilon}; 1 - 2\gamma; \rho) \\ & \mp \frac{-\gamma - \tilde{\epsilon}}{j + \tilde{m}} \mathcal{F}(1 - s\gamma - \tilde{\epsilon}; 1 - 2s\gamma; \rho)\Big] \end{aligned} \tag{A.2}$$

is defined in terms of confluent hypergeometric functions of the first kind. $\tilde{m} = mg/\beta$, $\tilde{\epsilon} = \epsilon g/\beta$ and $\rho = 2\beta r$ are the normalized mass, energy and distance away from the impurity. For $r \leq a$, the solution is defined in terms of Bessel functions

$$F_j^{-}(r) \;=\; J_{j-1/2}(\sqrt{E_+ E_-}\, r) \tag{A.3}$$

and

$$F_j^{(+)}(r) = -\frac{1}{E_+} \left\{ \partial_r [\sqrt{r} F_j^{(-)}(r)] - \frac{j}{r} \sqrt{r} F_j^{(-)}(r) \right\}, \tag{A.4}$$

where $E_\pm = \epsilon - V(a) \pm m$.

The energy of the levels follows from matching the wavefunctions at $r = a$, $\Psi_{r<a}(a) = \Psi_{r>a}(a)$, as shown in Fig. 2. For a given angular momentum state $j$, there is an infinite number of solutions that can be labeled by the index $n \in \mathbb{N}$, which is a non-negative integer. The lowest energy solution is labeled $n = 0$, with higher $n > 0$ attributed to the other higher excited states. For $j = \frac{1}{2}$ and $\epsilon = -m$, the critical coupling of the $n = 0$ level state is $g_c = 0.916$. The spectrum is in excellent agreement with the numerical results of [90].

### A.1.2 Hubbard $U$ term.

The Coulomb interaction among electrons in the lowest energy state $n = 0$ and $j = \frac{1}{2}$ is described by

$$\mathcal{H}_C = \frac{1}{2}\int \mathrm{d}^2 r \mathrm{d}^2 r' \hat{\rho}(\mathbf{r}) \frac{e^2}{\kappa|\mathbf{r}-\mathbf{r}'|}\hat{\rho}(\mathbf{r}'), \tag{A.5}$$

where $\hat{\rho}(\mathbf{r}) = \sum_\sigma \hat{\Theta}^\dagger_\sigma(\mathbf{r})\hat{\Theta}_\sigma(\mathbf{r})$ is the density operator defined in terms of the field operator $\hat{\Theta}_\sigma(\mathbf{r}) = \sum_\nu \Phi_{\frac{1}{2},\nu}(\mathbf{r})c_{\nu,\sigma}$. Hamiltonian (A.5) can be expressed explicitly in terms of $c$ operators, resulting in the Hubbard $U$ Hamiltonian described in the main text. The exchange term that also follows from (A.5) is identically zero due to the orthogonality of the two valley eigenvectors.

### A.1.3 Spin-orbital exchange Hamiltonian.

In second order of perturbation theory, the superexchange Hamiltonian is expressed in terms of $c$ operators as:

$$\mathcal{H}_s = -J_s \sum_{\langle ij\rangle} \sum_{\{\nu\},\{\sigma\}} c^\dagger_{i,\nu,\sigma} c_{j,\nu,\sigma} c^\dagger_{j,\nu',\sigma'} c_{i,\nu',\sigma'}, \tag{A.6}$$

with $J_s = t^2/U$. The exchange interaction between NN sites can be calculated from the Coulomb interaction $\sum_{\langle ij\rangle} \mathcal{H}_{C,ij}$,

$$\mathcal{H}_{C,ij} = \frac{1}{2}\int \mathrm{d}^2 r \mathrm{d}^2 r' \hat{\rho}(\mathbf{r}_i) \frac{e^2}{\kappa|\mathbf{r}-\mathbf{r}'|}\hat{\rho}(\mathbf{r}'_j). \tag{A.7}$$

We extend the definition of the field operators as a sum over lattice sites, $\Theta_\sigma(\mathbf{r}) = \sum_{\nu,i} \Phi_{\frac{1}{2},\nu}(\mathbf{r}_i)c_{i,\nu\sigma}$. The exchange part of the interaction above term can be explic-

itly written as

$$\mathcal{H}_e = J_e \sum_{\langle ij \rangle} \sum_{\{\nu\}\{\sigma\}} c^\dagger_{i,\nu,\sigma} c^\dagger_{j,\nu',\sigma'} c_{i\nu',\sigma'} c_{j,\nu,\sigma}, \tag{A.8}$$

where $J_e$ is given in the text. Hamiltonians (A.6) and (A.8) both map into pseudospin (valley) and spin operators, $\boldsymbol{\tau} = (\tau^x, \tau^y, \tau^z)$ and $\mathbf{S} = (S^x, S^y, S^z)$, through the following relations:

$$\begin{aligned}
c^\dagger_{i,\nu,\sigma} c_{i,\nu,\sigma} &\rightarrow \left(\frac{1}{2} + \nu\tau^z_i\right)\left(\frac{1}{2} + \sigma S^z_i\right) \\
c^\dagger_{i,\nu,\sigma} c_{i,-\nu,\sigma} &\rightarrow \tau^\nu \left(\frac{1}{2} + \sigma S^z_i\right) \\
c^\dagger_{i,\nu,\sigma} c_{i,\nu,-\sigma} &\rightarrow \left(\frac{1}{2} + \nu\tau^z_i\right) S^\sigma \\
c^\dagger_{i,\nu,\sigma} c_{i,-\nu,-\sigma} &\rightarrow \tau^\nu S^\sigma,
\end{aligned}$$

where $\tau^\nu = (\tau^x + \nu i \tau^y)$ and $S^\sigma = S^x + \sigma i S^y$. $\nu = \pm$, and $\sigma = \pm$ indexes the two valleys and spins respectively. This mapping results in Hamiltonian (4.18).

# Appendix B

## B.1 Wavefunction of the strong coupling sub-critical regime

The wave function $\Psi(\mathbf{r})$ of a two dimensional massive Dirac fermion moving around a Coulomb impurity satisfies,

$$(-i\boldsymbol{\sigma}\cdot\boldsymbol{\nabla}+V(r)+m\sigma_z)\Psi(\mathbf{r})=\epsilon\Psi(\mathbf{r}), \tag{B.1}$$

where

$$V(r)=\begin{cases}-g/r, & r>a\\ -g/a, & r\leq a\end{cases}$$

is the regularized Coulomb potential. Here we set $\hbar=v=1$.

The two-component wave function is

$$\Psi(r,\phi)=\frac{1}{\sqrt{2\pi}}\begin{pmatrix}F_j^{(-)}(r)e^{i(j-1/2)\phi}\\ F_j^{(+)}(r)e^{i(j+1/2)\phi}\end{pmatrix}, \tag{B.2}$$

he Dirac equation with the presence of an external potential becomes

$$\begin{bmatrix} \epsilon - m - U & -(\partial_r + \frac{\kappa+1}{r}) \\ (\partial_r - \frac{\kappa}{r}) & \epsilon + m - U \end{bmatrix} \begin{pmatrix} F_j^{(-)}(r) \\ F_j^{(+)}(r) \end{pmatrix} = 0$$

or equivalently

$$\begin{aligned} \frac{dF_j^{(-)}}{dr} - \frac{\kappa}{r} F_j^{(-)} + (\epsilon + m - U) F_j^{(+)} = 0 \\ \frac{dF_j^{(+)}}{dr} + \frac{\kappa+1}{r} F_j^{(+)} - (\epsilon - m - U) F_j^{(-)} = 0 \end{aligned} \tag{B.3}$$

where $\kappa = j - \frac{1}{2}$.

### B.1.1 Solution for $r > a$

The wave functions assumes the form ($j$ indexes will be dropped)

$$F^{(-)}(\rho) = \sqrt{m+\epsilon} e^{-\rho/2} \rho^{\gamma - 1/2} (Q_1 + Q_2)$$

$$F^{(+)}(\rho) = \sqrt{m-\epsilon} e^{-\rho/2} \rho^{\gamma - 1/2} (Q_1 - Q_2). \tag{B.4}$$

where $\rho = 2\lambda r$, $\beta = \sqrt{m^2 - \epsilon^2}$, and$\gamma = \sqrt{j^2 - g^2}$. After some algebra, we get

$$\rho Q_1' + (\gamma - \frac{\epsilon g}{\beta}) Q_1 - (j + \frac{mg}{\beta}) Q_2 = 0 \tag{B.5}$$

$$\rho Q_2' + (\gamma + \frac{\epsilon g}{\beta} - \rho) Q_2 - (j - \frac{mg}{\beta}) Q_1 = 0. \tag{B.6}$$

These equations can be decoupled

$$\rho Q_1'' + (1 + 2\gamma - \rho) Q_1' - (\gamma - \frac{\epsilon g}{\beta}) Q_1 = 0$$

$$\rho Q_2'' + (1 + 2\gamma - \rho)Q_2' - (1 + \gamma - \frac{\epsilon g}{\beta})Q_2 = 0,$$

both of which are Kummer's differential equation

$$xy'' + (c - x)y' - ay = 0$$

with the solution $y = c\mathcal{F}(a; c; x)$. Here we call the confluent Hypergeometric function of the first kind ${}_1F_1(a; c; x)$ as $\mathcal{F}(a; c; x)$,

$${}_1F_1(a; c; x) = 1 + \frac{a}{c}x + \frac{a(a+1)}{c(c+1)}\frac{x^2}{2!} + ...,$$

and notice that ${}_1F_1(a; c; x = 0) = 1$. The solutions are

$$Q_1 = c_1\mathcal{F}(\gamma - \frac{\epsilon g}{\beta}; 1 + 2\gamma; \rho) + d_1\mathcal{F}(-\gamma - \frac{\epsilon g}{\beta}; 1 - 2\gamma; \rho) \tag{B.7}$$

$$Q_2 = c_2\mathcal{F}(1 + \gamma - \frac{\epsilon g}{\beta}; 1 + 2\gamma; \rho) + d_2\mathcal{F}(1 - \gamma - \frac{\epsilon g}{\beta}; 1 - 2\gamma; \rho). \tag{B.8}$$

### B.1.2 Weak coupling regime

When $g < j$, $\gamma$ is real. Integrability of the wavefunction at $\rho \to \infty$ requires that $d_1 = d_2 = 0$. From Eq.$(B.7)$, one can determine the ratio

$$\frac{c_1}{c_2} = \frac{Q_1}{Q_2}\bigg|_{\rho=0} = \frac{j + \frac{mg}{\beta}}{\gamma - \frac{\epsilon g}{\beta}}.$$

To simplify the notation we call $\tilde{m} = mg/\beta$, $\tilde{\epsilon} = \epsilon g/\beta$, and

$$c_1 = c,\ c_2 = \frac{\gamma - \tilde{\epsilon}}{j + \tilde{m}}c.$$

That leads to the solution

$$F_j^{(-)}(\rho) = c\sqrt{m+\epsilon}e^{-\rho/2}\rho^{\gamma-1/2}[\mathcal{F}(\gamma-\tilde{\epsilon};1+2\gamma;\rho)+\frac{\gamma-\tilde{\epsilon}}{j+\tilde{m}}\mathcal{F}(1+\gamma-\tilde{\epsilon};1+2\gamma;\rho)]$$

$$F_j^{(+)}(\rho) = c\sqrt{m-\epsilon}e^{-\rho/2}\rho^{\gamma-1/2}[\mathcal{F}(\gamma-\tilde{\epsilon};1+2\gamma;\rho)-\frac{\gamma-\tilde{\epsilon}}{j+\tilde{m}}\mathcal{F}(1+\gamma-\tilde{\epsilon};1+2\gamma;\rho)]$$

This solution is regular at $\rho \to 0$, and the short distance cut-off can be set to zero.

### B.1.3 Strong coupling regime

When the coupling $g > \frac{1}{2}$, $\gamma$ becomes imaginary. With the requirement of imposing a small distance cut-off, the condition that the wave function behaves well at $\rho = 0$ is not necessary, so we should include both $\pm\gamma$ branches into the solutions. The ratio between the two And in this case we hope the wave functions die off at $\rho \to +\infty$, which can also serve to settle down the ratio between $\gamma-$branch and $(-\gamma)$-branch. The formula can be used here is the asymptotic form of the hypergeometric function,

$$ {}_1F_1(a;b;x) \sim \Gamma(b)\left(\frac{e^z z^{a-b}}{\Gamma(a)} + \frac{(-z)^{-a}}{\Gamma(b-a)}\right).$$

The second part is required if the gamma function $\Gamma(a)$ is infinite (when $a$ is a negative integer) or $\mathrm{Re}(z)$ is non-positive. In our case, we could exclude these two conditions, and only keep the second term. Therefore for large $|z|$, the dominating part (which is growing) of $\mathcal{F}(z)$ is

$$\mathcal{F}(a;b;z) \sim \frac{\Gamma(b)}{\Gamma(a)}e^z z^{a-b},$$

and we ask for some condition to cancel this term. For $aF(\rho;\gamma)+bF(\rho;-\gamma)$ we need the following two terms to be finite at $\rho\to+\infty$

$$a\rho^{\gamma-1/2}\mathcal{F}(\gamma-\tilde{\epsilon};1+2\gamma;\rho)+b\rho^{-\gamma-1/2}\mathcal{F}(-\gamma-\tilde{\epsilon};1-2\gamma;\rho) \tag{B.9}$$

$$a\rho^{\gamma-1/2}\frac{\gamma-\tilde{\epsilon}}{j+\tilde{m}}\mathcal{F}(1+\gamma-\tilde{\epsilon};1+2\gamma;\rho)+b\rho^{-\gamma-1/2}\frac{-\gamma-\tilde{\epsilon}}{j+\tilde{m}}\mathcal{F}(1-\gamma-\tilde{\epsilon};1-2\gamma;\rho) \tag{B.10}$$

From $B.9$,

$$\frac{a}{b}=-\frac{\Gamma(\gamma-\tilde{\epsilon})}{\Gamma(1+2\gamma)}\frac{\Gamma(1-2\gamma)}{\Gamma(-\gamma-\tilde{\epsilon})}=-\frac{\Gamma(\gamma-\tilde{\epsilon})}{(2\gamma)\Gamma(2\gamma)}\frac{(-2\gamma)\Gamma(-2\gamma)}{\Gamma(-\gamma-\tilde{\epsilon})}=\frac{\Gamma(\gamma-\tilde{\epsilon})}{\Gamma(2\gamma)}\frac{\Gamma(-2\gamma)}{\Gamma(-\gamma-\tilde{\epsilon})}.$$

We can assign

$$a=\frac{\Gamma(-2\gamma)}{\Gamma(-\gamma-\tilde{\epsilon})},\qquad\qquad b=\frac{\Gamma(2\gamma)}{\Gamma(\gamma-\tilde{\epsilon})} \tag{B.11}$$

The solution for $F^{(\pm)}$ is

$$\begin{aligned}F_j^{(\mp)}(r)&=c'\sqrt{m\pm\epsilon}e^{-\rho/2}\rho^{-1/2}\\&\times[\frac{\Gamma(-2\gamma)}{\Gamma(-\gamma-\tilde{\epsilon})}\rho^{\gamma}\mathcal{F}(\gamma-\tilde{\epsilon};1+2\gamma;\rho)+\frac{\Gamma(2\gamma)}{\Gamma(\gamma-\tilde{\epsilon})}\rho^{-\gamma}\mathcal{F}(-\gamma-\tilde{\epsilon};1-2\gamma;\rho)\\&\pm\frac{\Gamma(-2\gamma)}{\Gamma(-\gamma-\tilde{\epsilon})}\frac{\gamma-\tilde{\epsilon}}{j+\tilde{m}}\rho^{\gamma}\mathcal{F}(1+\gamma-\tilde{\epsilon};1+2\gamma;\rho)\\&\pm\frac{\Gamma(2\gamma)}{\Gamma(\gamma-\tilde{\epsilon})}\frac{-\gamma-\tilde{\epsilon}}{j+\tilde{m}}\rho^{-\gamma}\mathcal{F}(1-\gamma-\tilde{\epsilon};1-2\gamma;\rho)]\end{aligned} \tag{B.12}$$

### B.1.4 Solution for $r \leq a$

In the $r < a$ region, we define

$$F_j^{(-)}(r) = \frac{1}{\sqrt{r}} A(r)$$
$$F_j^{(+)}(r) = \frac{1}{\sqrt{r}} B(r)$$

the Dirac equation becomes

$$A'(r) - \frac{j}{r} A(r) + E_+ B(r) = 0$$

$$B'(r) + \frac{j}{r} B(r) - E_- A(r) = 0$$

where $E_\pm = \epsilon + \frac{g}{a} \pm m$. These equations can be decoupled into

$$A''(r) + (E_+ E_- + \frac{j - j^2}{r^2}) A(r) = 0$$

$$B''(r) + (E_+ E_- - \frac{j + j^2}{r^2}) B(r) = 0$$

The solutions are

$$A(r) = c_1 \sqrt{r} J_{j-1/2}(\sqrt{E_+ E_-} r)$$

$$B(r) = c_2 \sqrt{r} J_{j+1/2}(\sqrt{E_+ E_-} r)$$

and $\sqrt{E_+ E_-} = \sqrt{\epsilon^2 + (g/a)^2 + (2\epsilon g/a) - m^2}$.

From

$$B(r) = -\frac{A' - \frac{j}{r} A}{E_+},$$

we have

$$B(r) = -\frac{c_1}{E_+}[\frac{\frac{1}{2}-j}{\sqrt{r}}J_{j-1/2}(\sqrt{E_+E_-}r) + \sqrt{r}J'_{j-1/2}(\sqrt{E_+E_-}r)]$$

### B.1.5 Energy

The energy $\epsilon$ can be determined by matching the inside solution and the outside one, formally through

$$Out(j,\epsilon,r,g)\Big|_{r=a} = Ins(j,\epsilon,r,g)\Big|_{r=a}$$

For given $j$, $g$, and at $r = a$, we can determine the energy $\epsilon$

$$\left(\begin{array}{c} \sqrt{r}F(r) \\ \sqrt{r}G(r) \end{array}\right)\Big|_{r=a} = \left(\begin{array}{c} A(r) \\ B(r) \end{array}\right)\Big|_{r=a}$$

# Appendix C

## C.1 Topological Phase Transitions

### C.1.1 Order of the transitions

In order to explicitly verify the existence of a quantum critical second order phase transition for $|\mu| \gtrsim 0.18$ eV, we plot in Fig C.1 the free energy for $\mu = 0.1$eV and $\mu = 0.3$ eV. In the former, the topologically trivial superconducting state $\mathcal{N} = 0$ coexists with the normal state at the critical coupling $g_{1c} \approx 0.0919$ eV, where the order parameter is discontinuous. For $\mu = 0.3$eV, the transition to the normal state becomes continuous at $g = \bar{g}_{1c} \approx 0.0561$eV, where the system has a topological phase transition separating the normal state and the topological $\mathcal{N} = -3$ state. At $g = g_{1c} \approx 0.078$ eV, the order parameter jumps, signaling the onset of a discontinuous topological phase transition between the $\mathcal{N} = -3$ and $\mathcal{N} = 1$ states.

### C.1.2 Line of quantum critical points

Although the intra-orbital state is fully gapped, the Fermi surface at high doping is very anisotropic and produces an anisotropic superconducting gap in the energy

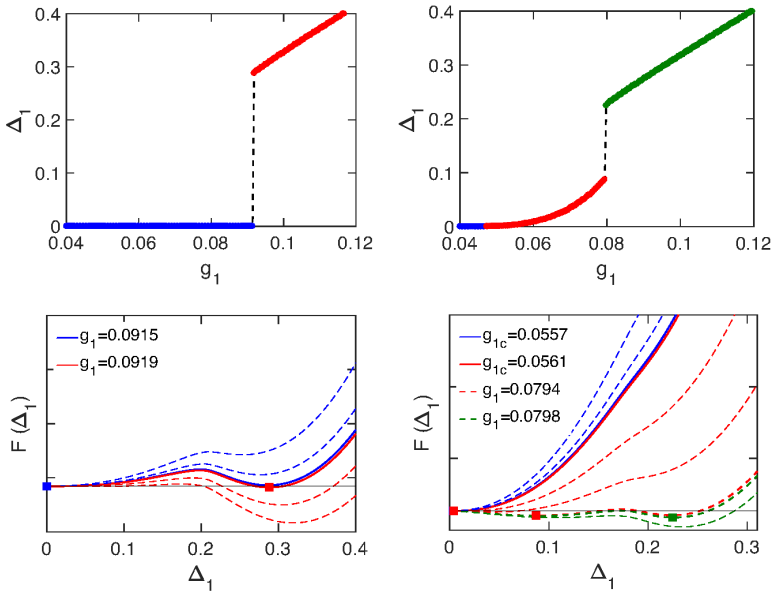


Figure C.1: Top left: scaling of the intra-orbital coupling $\Delta_1$ vs $g_1$ for $\mu = 0.1$ eV : first order phase transition from the normal to the superconductor state with $\mathcal{N} = 0$. Bottom left: Free energy for $\mu = 0.1$ eV, showing the coexistence of the normal and superconducting states. Top right: $\Delta_1$ vs $g_1$ for $\mu = 0.3$ eV. The system has a second order phase transition at $\bar{g}_{1c} = 0.0.0561$ to a topological phase with $\mathcal{N} = -3$ and a first order phase transition at $g_{1c} = 0.078$ eV, where $\Delta_1$ jumps. Bottom right: Free energy for $\mu = 0.3$ eV, showing coexistence of the $\mathcal{N} = -3$ and $\mathcal{N} = 1$ states.

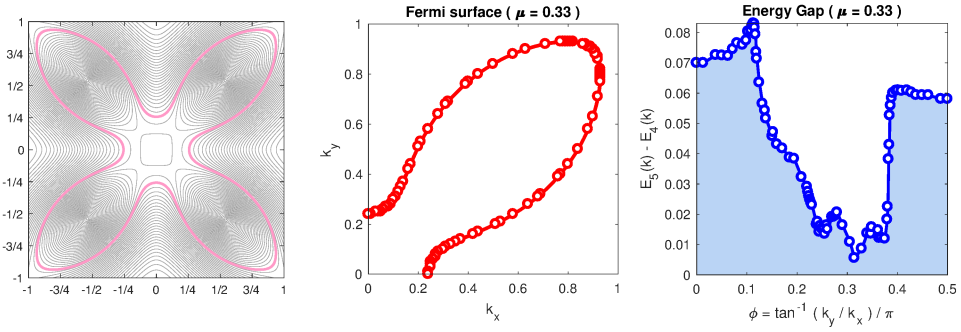


Figure C.2: Left: Fermi surface for $\mu = 0.33$eV. Center: Path along the Fermi surface, where the energy gap in the superconducting state (intra-orbital gapped state) is calculated numerically in the weak coupling regime. Right: Anisotropic gap as a function of the angle $\phi$ from 0 to 0.5 rad.

spectrum around the Fermi surface. In Fig. C.2 we plot the Fermi surface for $\mu = 0.33$eV and the corresponding energy gap along the Fermi surface, which has a significant variation. This anisotropic state requires a finite attractive coupling $g_1$ to stabilize the formation of Cooper pairs, leading to a quantum critical phase transition even when the normal system has a large DOS at the Fermi level.

We extract the quantum critical scaling of the order parameter $\Delta_1$ with $g_1$ in the vicinity of the critical point of the second order phase transition for $\mu = 0.3$, 0.312 (which coincides with the energy of a van Hove singularity) and 0.4 eV. The order parameter scaling has the form

$$\Delta_1(g_1) = \alpha \left( \frac{g_1}{\bar{g}_{1c}} - 1 \right)^{\beta},$$

with $\beta \approx 2.7 \pm 0.1$, $\alpha = 0.1$ and critical couplings $\bar{g}_{1c} = 0.046$ and 0.041 eV for $\mu = 0.3$ and 0.4 eV respectively. However, at $\mu = 0.312$ eV, $\bar{g}_{1c}$ suddenly drops to $\bar{g}_{1c} \approx 0.017$ eV and $\alpha \approx 2 \times 10^{-4}$. This abrupt drop in the numerical value of $\bar{g}_{1c}$ suggests a crossover to exponential behavior due to the presence of a Van Hove singularity at the Fermi surface. In that scenario, the anisotropy of the

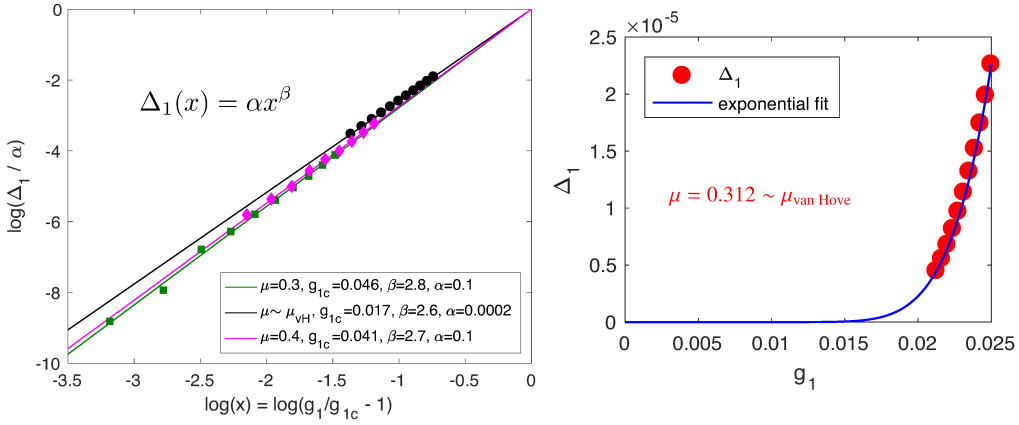


Figure C.3: Left: Scaling of the gapped state order parameter $\Delta_1$ vs coupling $g_1$ for $\mu = 0.3$, 0.312 and 0.4 eV. At $\mu = 0.312$ eV the Fermi surface is nested at the van Hove singularities. Away from the van Hove, the scaling can be fit with a power law behavior near a quantum critical point ($g = \bar{g}_{1c}$). In the immediate vicinity of the van Hove, $\bar{g}_{1c}$ drops abruptly, suggesting that the scaling crosses over to exponential behavior (right panel).

gap around the Fermi surface as a whole becomes unimportant and the system likely becomes unstable towards superconductivity at any arbitrary attractive coupling, as in conventional Fermi liquids. At that filling, $\Delta_1$ can fit well with an exponential curve $\Delta_1 = \alpha / [\exp(\beta g_1) - 1]$ , with $\alpha = 0.22$ and $\beta = 4.36$.

Fig. C.4 shows the Fermi surface at $\mu = 0.312$ eV, where it crosses a saddle point indicated by the vectors $q_1$ and $q_2$. On the right we fit the energy spectrum around that one saddle point. In general, the energy and position of van Hove singularities, as well as their dispersion, are not universal and are sensitive to the parametrization of the tight binding model. We assume the parametrization from ref. [171], which is based on ab initio results.

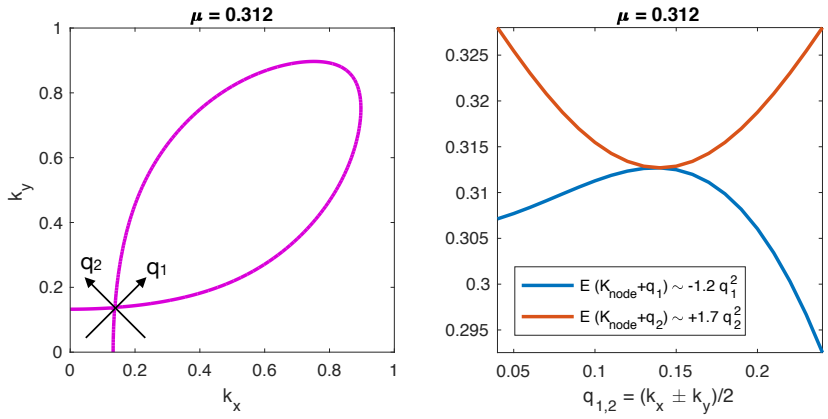


Figure C.4: Left: Fermi surface at $\mu = 0.312$ eV. The crossing indicates the position of the Van Hove singularity in the Brillouin zone for the tight-binding parameterization in the text. Right: Fitting of the bands around the van Hove singularity.

### C.1.3 $T_c$ estimate

For a purely electronic mechanism, a crude estimate of the critical temperature can be calculated when the chemical potential is very close to the van Hove singularities of the band. For perfect nesting ($\alpha = \beta$),

$$\chi_{ef} \approx \chi(\mathbf{Q}),$$

where

$$\chi(\mathbf{Q}) \sim \ln^2\left(\frac{\Lambda}{\delta\mu}\right)$$

has a double logarithmic divergence [172]. In perturbation theory, the dimensionless effective interaction is

$$\lambda_{ef} = V_0 + V_0^2\chi_{ef},$$

where

$$V_0 = \frac{U}{8\pi\Lambda} \ll 1$$

is the normalized interaction between nearest neighbor sites [173]. Since the DOS $\rho(0) = \chi(0) \sim \ln(\Lambda/\delta\mu)$, the gap equation reads

$$1 \sim \lambda_{ef} \int \mathrm{d}E \rho(0) \frac{\tanh(E/2T_c)}{E} \sim V_0^2 \chi(\mathbf{Q})\chi(0) \ln(\mu/T_c),$$

and hence

$$T_c \sim \delta\mu \, \mathrm{e}^{-1/V_0^2\chi(\mathbf{Q})\chi(0)} \approx \delta\mu \exp\left[-\frac{1}{V_0^2 \ln^3(\Lambda/\delta\mu)}\right].$$

This expression gives an upper bound for the critical temperature, since the nesting condition is not perfectly satisfied. For $\Lambda \sim t = 0.3$ eV, $U \sim 1$ eV, and $\delta\mu/t = 0.01$, then $T_c \sim 2$ meV$\approx 20$K.